Applied Surface Science

Thermal behaviour of Cu and Au nanoparticles grown on CeO2 thin films

--Manuscript Draft--

Manuscript Number:	APSUSC-D-21-10023R1
Article Type:	Full Length Article
Keywords:	alloy, catalyst, XPS, ion scattering
Corresponding Author:	Christopher Baddeley, PhD University of St Andrews St Andrews, Fife UNITED KINGDOM
First Author:	Rory Megginson
Order of Authors:	Rory Megginson
	Federico Grillo, PhD
	Stephen Francis, PhD
	Vagner Paes, PhD
	Henrique Trombini, PhD
	Pedro Grande, PhD
	Andrew Rossall, PhD
	Jaap van den Berg, PhD
	Christopher Baddeley, PhD
Abstract:	Bimetallic catalysts are often more active and/or selective than their monometallic counterparts. The behaviour of such catalysts is frequently strongly dependent on the molar ratio of the two elements as well as nanoparticle size and the interaction with the support material. X-ray photoelectron spectroscopy (XPS) is an excellent surface analytical technique for probing the electronic properties of catalytic systems. When a mixture of pure and alloyed particles is present, it is more difficult to extract information from XPS given that it is a spatial averaging technique. Recently, the technique of medium energy ion scattering (MEIS) has been exploited to investigate the depth-dependent composition of nanoparticles on planar surfaces. Herein, we combine the two techniques to investigate the nature of Cu and Au nanoparticles deposited onto ultrathin CeO 2 films on Si(111) examining their morphology and chemical composition as a function of annealing temperature for samples that have been maintained in an ultrahigh vacuum environment and exposed to air. The Cu/Au/CeO 2 /Si(111) is chosen as a model system in order to provide insight into how the catalytic properties of Cu/Au/CeO 2 depend on the presence of discrete Cu and Au particles versus fully intermixed Cu/Au systems.
Suggested Reviewers:	Laszlo Ovari ovari@chem.u-szeged.hu
	Phil Davies daviespr@cardiff.ac.uk
	Gavin Bell University of Warwick gavin.bell@physics.org

Thermal behaviour of Cu and Au nanoparticles grown on CeO_2 thin films

R. Megginson[1], F. Grillo[1], S. M. Francis[1], V. Z. C. Paes[2], H. Trombini[2], P. L. Grande[2], A. K. Rossall[3], J. A. van den Berg[3], C. J. Baddeley[1]*

1. EaStCHEM School of Chemistry, University of St Andrews, North Haugh, St Andrews, Fife, KY16 9ST, United Kingdom
2. Laboratório de Implantação Iônica, Universidade Federal do Rio Grande Sul UFRGS, Instituto de Física, Av. Bento Goncalves 9500, BR-91501970 Porto Alegre, RS, Brazil
3. MEIS Facility - Ion Beam Centre; School of Computing and Engineering, University of Huddersfield, Huddersfield, HD1 3DH, United Kingdom

* email cjb14@st-andrews.ac.uk

Abstract:

Bimetallic catalysts are often more active and/or selective than their monometallic counterparts. The behaviour of such catalysts is frequently strongly dependent on the molar ratio of the two elements as well as nanoparticle size and the interaction with the support material. X-ray photoelectron spectroscopy (XPS) is an excellent surface analytical technique for probing the electronic properties of catalytic systems. When a mixture of pure and alloyed particles is present, it is more difficult to extract information from XPS given that it is a spatial averaging technique. Recently, the technique of medium energy ion scattering (MEIS) has been exploited to investigate the depth-dependent composition of nanoparticles on planar surfaces. Herein, we combine the two techniques to investigate the nature of Cu and Au nanoparticles deposited onto ultrathin CeO_2 films on Si(111) examining their morphology and chemical composition as a function of annealing temperature for samples that have been maintained in an ultrahigh vacuum environment and exposed to air. The Cu/Au/CeO_2/Si(111) is chosen as a model system in order to provide insight into how the catalytic properties of Cu/Au/CeO_2 depend on the presence of discrete Cu and Au particles versus fully intermixed Cu/Au systems.

Keywords: alloy, catalyst, XPS, ion scattering

Introduction

There are many applications exploiting metallic nanoparticles on high surface area oxide supports including heterogeneous catalysts, photocatalysts and electrocatalysts.[1] Ceria (CeO_2) has a number of advantages as an oxide support including its ability to enhance metal dispersion; displaying a greater resistance to thermal sintering than other oxide supports and due to its ability to operate as an oxygen reservoir, thereby influencing surface chemical processes occurring on ceria-based materials.[2-4] Unlike supports such as SiO_2, when a metal atom interacts with CeO_2, charge transfer processes can occur resulting in the formation of Ce^{3+} surface species.[5, 6]

Bimetallic particles often outperform their monometallic counterparts in terms of activity and/or selectivity. For example, adding a second element can overcome the intrinsically low activity of gold. Conversely, the addition of a relatively inert element such as gold to a more reactive metal can allow the establishment of control over selectivity towards a particular catalytic route.[7] Cu/Au systems have been used for a number of applications in catalysis and electroreduction. Experimental [8] and theoretical [9, 10] studies have shown that the ordering and composition of Cu/Au nanoparticles is strongly dependent on temperature and surrounding environment. Cu/Au nanoparticles supported on CeO_2 have been used in the hydrogenation of cinnamaldehyde,[11] CO oxidation,[12-14] the oxygen-enhanced water gas shift reaction,[15] the photocatalytic oxidation of benzyl alcohol[16] and in the steam reforming of methanol.[17] Our interest in Cu/Au/CeO_2 stems from the development of catalysts for the “hydrogen-free” selective hydrogenation of furfural by Keane and co-workers.[18] In this catalytic system, hydrogen produced by the dehydrogenation of 2-butanol is fully utilised in the selective conversion of furfural to furfuryl alcohol. In this application, it is believed to be desirable to maintain separate Cu and Au particles on the oxide surface. However, Cu and Au have a very strong tendency to intermix forming solid solutions over the whole compositional range,[19, 20] so a motivation for the current work is to investigate the thermal behaviour of Cu/Au/CeO_2 model catalysts prepared by deposition of Cu and Au nanoparticles onto planar ceria surfaces.

The surface composition of bimetallic systems is commonly different to the bulk composition and depends on a number of parameters such as the relative surface energies of the two elements; atomic size; temperature and the environment to which the sample is exposed. In the phase diagram of bulk Cu/Au mixtures, only a few ordered phases are known, notably for specific Cu:Au ratios.[21, 22] For most bulk compositions, a gold-rich surface layer is favoured.[23] Nevertheless, both intermixed [24-29] and ordered surface terminations [25, 26] can be prepared when subjecting Cu/Au(111) systems to specific thermal treatments.

The technique of medium energy ion scattering (MEIS) possesses near monolayer depth resolution and has been established as a technique for the characterisation of the depth dependent composition of bimetallic layers on single crystal surfaces under the influence of adsorbates. [30, 31] A number of groups have aimed to refine the technique to investigate the depth dependent composition of nanoparticles on flat oxide surfaces.[32-35]

In this article MEIS, atomic force microscopy (AFM) and X-ray photoelectron spectroscopy (XPS) are used to characterise the temperature dependence of the composition profile of Cu/Au particles on CeO_2 thin films grown on Si(111).

Experimental Section

X-ray photoelectron spectroscopy (XPS)

XPS measurements were collected in an ultrahigh vacuum (UHV) chamber housing a Scienta ESCA-300 spectrometer equipped with a monochromatic Al *Kα* (1486.6 eV) rotating anode and an unmonochromated Al *Kα* anode. The detection system consisted of a large hemispherical analyser coupled to a multichannel plate/video camera. The instrument was calibrated daily to the Au 4f and Ag 3d photoelectron lines. The binding energy scale is referenced to the signals of Si 0/IV of Si/SiO_2 at 99.8 eV and 103.3 eV respectively. Peak fitting was carried out using CasaXPS software version 2.3.17.

Medium Energy Ion Scattering

MEIS analysis was carried out at the MEIS facility at the University of Huddersfield, UK using a beam of nominally 100 keV He^+ ions entering a UHV scattering chamber that houses a 3-axis target goniometer and a rotatable electrostatic energy analyser. As a sectional toroidal type, the analyser enables the simultaneous collection of a range of energies (1.5% of pass energy) and angles (27°) of backscattered ions through the use of a 2D detector located behind a set of channel plate multipliers that records both energy and angle of scattered ions. The overall 2D energy and angle spectrum is composed of individual tiles (one for each pass energy) that are linked together by software. The Si(111) sample was aligned such that the [101] direction was coincident with the ion beam incident at 35.3° off normal which leads to channelling within the Si lattice, while the centre of the analyser was aligned with the [121] direction resulting in a central backscattering angle of 125.3°. Thus, the plane of scattering contains the [121] surface direction. Energy spectra were extracted from the 2D spectrum for the three scattering angles of 119.3°, 125.3° and 131.3°. Large scattering angles were chosen to ensure maximum energy separation between the different scattered peaks in the spectra. MEIS energy spectra were analysed using the PowerMEIS simulation code discussed below.

PowerMEIS

All MEIS spectra were analysed with the PowerMEIS-3 (PM3) software. [34, 36, 37]This software uses a Monte Carlo algorithm that performs simulations of the interaction of ions (and also electrons [37]) with matter including multiple scattering (MS) and reliable scattering cross-sections. PM3 describes the sample by voxels organized in a matrix format, which may represent any complex structure consisting of a number of compounds. Here we considered different type of matrices describing discrete, alloy and core-shell spherical particles as well as thin films. In addition, each matrix has a weight to allow for a statistical mixture of structures. For enhanced computational efficiency PM3 uses a variation on the trajectory reversal approach to connect incoming and outgoing ion trajectories. These trajectories are constructed by first simulating two sets of trajectories: one set starting from the beam direction, and one set starting from the analyser. The position, energy, and path travelled by the ions during these trajectories are stored. The contribution of a specific incoming and outgoing trajectory combination from an atom A at position x,y,z is proportional to the differential elastic scattering cross section of atom A at the scattering angle between the incoming and (time-reversed) outgoing ion trajectory and the concentration of atom A at x,y,z. Simply V-shaped trajectories (straight-line in and out) can be also selected and provided the same results for the present study. The main physical inputs are the scattering cross-section, calculated from the Moliere potential, the electronic stopping power, from the SRIM 97 [38] and energy-loss straggling from the Chu model.[39] Since neutralized ions cannot be measured by our MEIS analyser, we included the neutralization correction from the Marion equation[40] in the simulations. PM3 assumes an amorphous target, i.e. the contribution from different atoms are added incoherently. Further details can be found elsewhere. [32, 41]

Atomic Force Microscopy

AFM measurements were carried out using a Bruker MultiMode 8 AFM. To minimise surface damage, all images were acquired via tapping mode using a Bruker RTESPA-300 probe (nominal frequency 300 kHz, nominal spring constant 40 N m^{-1}).

Preparation of model catalysts

Ceria films of a thickness of approx. 2 nm were prepared on Si(111) by the following procedure which is based on that of Zheng *et al*. who deposited thin ceria films on nickel.[42] Cerium nitrate hexahydrate (0.43 g) was dissolved in 70 ml of ethanol with stirring, 30 ml of collodion solution (cellulose nitrate 4-8% in ethanol/diethyl ether) was then added to control the viscosity. All reagents were purchased from Sigma Aldrich and used without further treatments. This solution was then diluted by a factor of ten while maintaining the ethanol:collodion ratio. Si(111) wafers were cleaned by immersion in a basic piranha solution for 30 mins, followed by a thorough rinse with deionised water. Finally, wafers were dried in flowing N_2(g). The clean Si(111) wafers were then dipped three times (for 100 s on each occasion) into the cerium containing solution and dried for 1 hour before being calcined in air up to a temperature of 775 K at a ramp rate of 5 K min^{-1} and held at 775 K for 20 minutes.

Copper and gold were deposited in UHV via metal vapour deposition via conventional filament evaporation sources consisting of copper wire (5N purity, 0.1 mm diameter) or gold wire (5N, 0.2 mm) wound around a tantalum filament (5N, 0.25 mm). Sample heating was carried out in UHV with the temperature of the heating stage on which the sample was mounted monitored by a K-type thermocouple. Coverages in copper and gold are reported in monolayers (ML), where we define 1 ML as 1×10^{15} atoms cm^{-2}.

Results and Discussion:

Many previous studies of gold or copper nanoparticle growth have been carried out on well-defined ceria surfaces, e.g. CeO_2(111). In a MEIS experiment, when ions are backscattered from surface atoms, the peak position in the energy spectrum is governed by conservation of energy and momentum in the elastic collision. When ions are backscattered from subsurface atoms, the incident ions are subject to additional inelastic energy losses dependent on the pathlength of the ion within the sample. Consequently, a thick CeO_2 film would result in a broad Ce-related peak in the MEIS spectrum, which would swamp the signal from copper nanoparticles dispersed on the ceria surface. PowerMEIS analysis requires the fitting of the peak shapes which is facilitated by a flat background. For this reason, thin ceria films were required grown on a substrate with a low atomic mass, such as Si used in this work.

CeO_2 film on Si(111)

A representative AFM image of an ultrathin CeO_2 film grown on Si(111) is shown in Figures 1a. Disc-shaped ceria particles are observed with an average diameter of ~23 nm (range 5-50 nm). The line profile in Figure 1b shows that the variation in height across the particles is in the range of 1-3 nm. Figure 1c shows the Ce 3d region of the XP spectrum of an analogous CeO_2 film on Si(111). The attenuation of the Si 2p signal as a result of ceria deposition allows an estimate of the CeO_2 film thickness. Assuming that the film is flat, the 58% attenuation of the Si 2p peak (see table 1) equates to a CeO_2 film thickness of approximately 1.8 nm. Assuming that the film adopts the fluorite structure of bulk CeO_2 (lattice parameter 0.541 nm) and that the surface terminates in {111} planes (interlayer spacing 0.313 nm), this corresponds to an average thickness of between 5 and 6 layers.

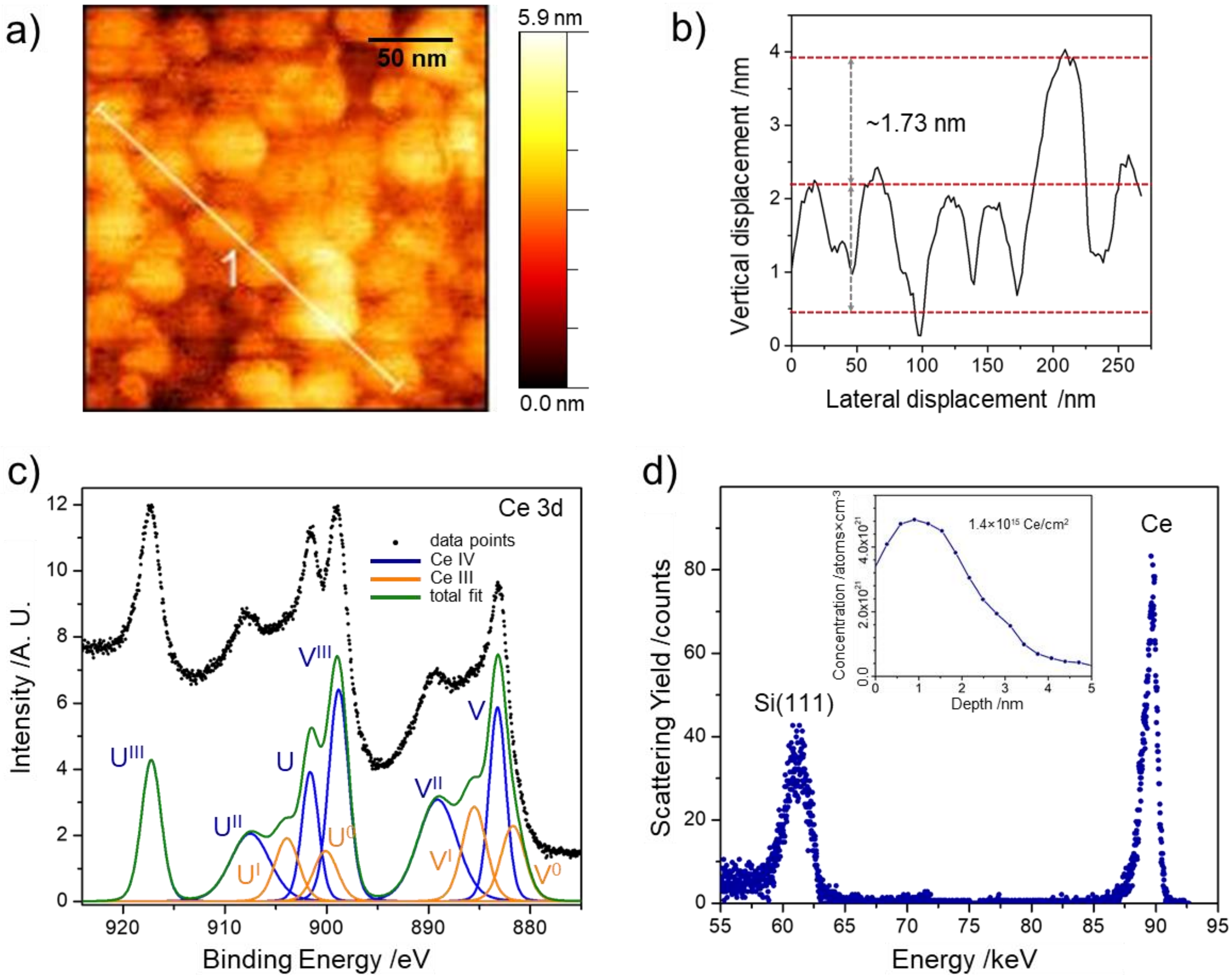

Figure 1. Characteristic AFM image of a) 255 nm × 255 nm of a CeO_2 film grown on Si(111); b) line profile showing the height variation along line 1 in Figure 1b); c) XP spectrum of the Ce 3d region showing the fitting of the peaks to Ce(III) and Ce(IV) of a CeO_2 film grown on Si(111); Ce(IV) components are shown in blue, Ce(III) components are shown in orange; peaks are labelled according to the nomenclature introduced by Burroughs *et al*. [43]; d) MEIS spectrum showing the intensity of scattered ions as a function of ion energy at a scattering angle of 125.3° of a CeO_2 film grown on Si(111) and in the inset the MEIS derived Ce depth profile indicating an on average 2.5 nm Ce film thickness.

Table 1. Raw XPS areas (normalised counts and %Ce(IV)) from the preparation of a ~1.6 ML Cu on ~1.0 ML Au on a CeO_2/Si(111) sample.

system	**Cu $2p_{3/2}$**	**Ce 3d**	**% Ce(IV)**	**Si 2p**	**Au 4f**
Si(111)	-	-	-	13.6	-
CeO_2/Si(111)	-	101.1	91.2	5.7	-
Au/CeO_2/Si(111)	-	91.1	88.6	5.2	8.2
Cu/Au/CeO_2/Si(111)	13.3	83.6	83.2	4.6	8.0

The Ce 3d region was fitted to quantify the relative amounts of Ce(IV) and Ce(III) oxidation states in the thin film. The as-deposited film was found to be almost exclusively constituted of Ce(IV), consistent with the formation of near-stoichiometric CeO_2 films. More details of the fitting procedure used for the Ce 3d region can be found in the Supplementary Information (SI1).

Figure 1d shows the MEIS spectrum from a ceria film on Si(111) prepared under analogous conditions. The cerium peak at ~88 keV has a FWHM of ~1.3 keV and is well separated from the peak caused by gold nanoparticles (expected at ~91 keV). The Ce MEIS peak was converted directly into a depth profile based on well-known inelastic energy loss rates and the silicon random level reference. Shown in the inset in Fig. 1d), it indicates a mean depth of the ceria film of 2.5 nm, close to the value determined by AFM, and an average deposited cerium dose of 1.4×10^{15} atoms cm^{-2}.

Investigation of the effect of variable CeO_2 film thickness on MEIS spectra.

The distribution of CeO_2 grown on Si(111) was investigated by MEIS through the PM3 software. Figure 2a shows the MEIS spectrum after the deposition of 2.4 ML Cu followed by 0.54 ML Au onto a CeO_2 film on Si(111). This spectrum confirms that the cerium profile is sufficiently narrow that both copper and gold signals each appear against a flat background, which is important for the PM3 analysis of these signals presented later. Three models were used to represent the CeO_2 arrangement as can be seen in Figure 2b). According to the MEIS spectrum shown in Figure 2a, when the CeO_2 layer is simulated as a continuous thin film the experimental and simulated data show poor agreement at the cerium tail (arrow in figure 2a) and at the silicon edge (~61 keV). The cerium tail can be simulated better by adding a second layer of cerium diffusing into the silicon surface, but the silicon edge continues not to match. To improve further the agreement between experimental and simulated data, a ceria island model was used. In this case, eight steps were created with thickness for the ceria islands ranging from 0 to 3 nm. The fraction of each step of this model can be seen in Figure 2b). In each model the total atomic density (number of atoms per cm^2) was kept constant. This result is in agreement with the AFM images shown in Figure 1 (a-b). The copper and gold nanoparticles on the ceria film do not significantly affect the Ce-related signal since most of the ceria surface is not covered by them. A continuous thin film of metal would result in a shift of the cerium peak to lower energy, such a shift was not observed in the MEIS spectra. Therefore, the fit to the cerium signal was refined prior to a detailed fitting of the copper and gold peaks. In addition, consistently the inclusion of copper and gold nanoparticles on the ceria films did not significantly change its initial profile.

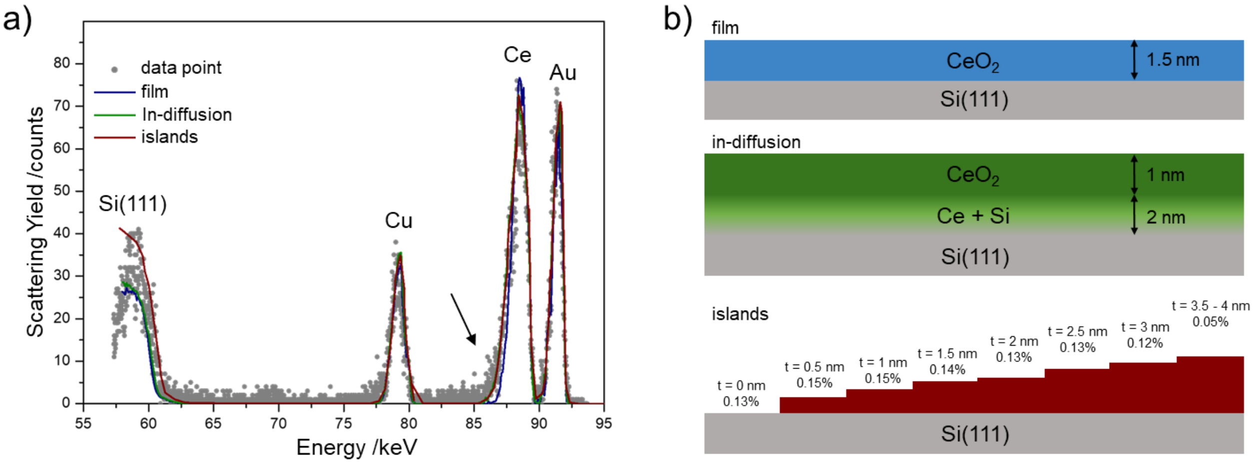

Figure 2. a) MEIS experimental data and simulations for a sample prepared by dosing copper (2.4 ML) followed by gold (0.54 ML) without thermal treatment for the three CeO_2 distribution models and for the backscattering angle of 131.3°. b) Schematic diagrams showing the three models employed for simulating the distributions of the CeO_2 layer morphology and thickness. In the first model a 1.5 nm thick CeO_2 film was used. In the second model a Ce in-diffusion layer was added. In the third model, the CeO_2 film thickness was allowed to vary between 0 and 3 nm, representing islands of CeO_2. Each model has the same number of atoms per cm^2.

The thermal behaviour of a typical CeO_2/Si(111) layer was investigated by XPS. From the analysis of the Ce 3d core level, the Ce(IV):Ce(III) was evaluated as ca. 90%:10% upon preparation. A change of the cerium oxidation state is seen with annealing, reaching a Ce(IV):Ce(III) of ca. 22%:78% after annealing to 500 K. The envelope of the O 1s peak, which contains also the signals of oxygen related to SiO_2 and the Ce-O-Si interfacial oxygen, varies accordingly. Ce 3d and O 1s core level spectra with annealing are reported in SI2.

Deposition of Au onto CeO_2/Si(111)

XPS

The metal vapour deposition of gold was carried out on a CeO_2/Si(111) sample at 300 K resulting in a gold coverage of ~1 ML. XP spectra of the Ce 3d and Au 4f regions are displayed in Figures 3a and 3b. For these XPS experiments, the non-monochromated Al *k*α source was used. The fitting of the Ce 3d region shown in figure 3a reveals that gold deposition results in a small decrease in Ce(IV):Ce(III) composition from ~91% Ce(IV) to ~89% (Table 1). This is consistent with a reduction of the ceria surface during the nucleation of gold particles. The reduction of CeO_2 by the deposition of metallic nanoparticle has been reported previously for a range of metals.[6, 44, 45] The Au $4f_{7/2}$ peak is recorded at 84.6 eV, as reported in figure 3b, a value in good agreement with that expected for metallic gold, 84.0 eV. [6, 46]

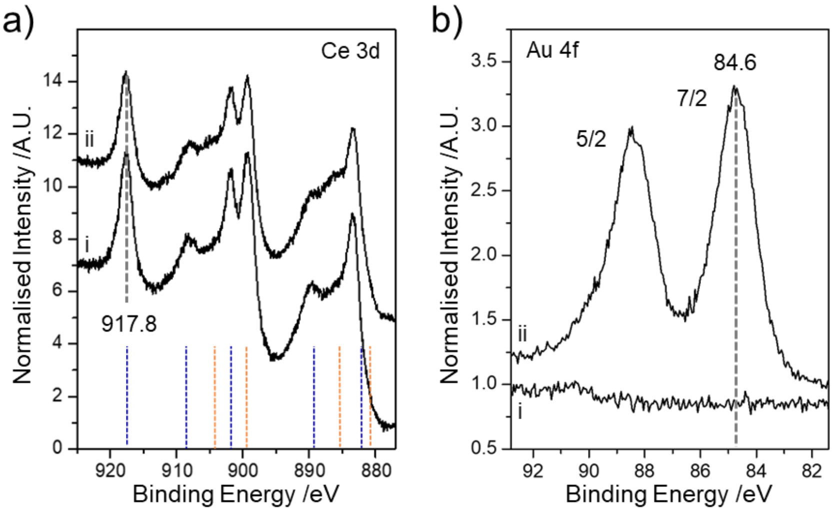

Figure 3. XP spectra displaying a) the Ce 3d region and b) the Au 4f region of the CeO_2/Si(111) surface, i) prior to and ii) after the deposition of ~1 ML Au, at a deposition temperature of 300 K; spectra are offset for clarity. In a) expected positions for Ce(IV)/Ce(III) components are indicated by blue/orange dashed lines.

Deposition of Cu onto Au/CeO_2/Si(111)

XPS:

The metal vapour deposition of copper was carried out on the Au/CeO_2/Si(111) sample at 300 K resulting in a copper coverage of ~1.6 ML. XP spectra of the Cu $2p_{3/2}$, Ce 3d and Au 4f regions before and after deposition of copper are displayed in Figures 4a-c. The Cu $2p_{3/2}$ is recorded at 933.5 eV, as shown in figure 4a; this value is in good agreement with those recorded for both metallic copper and Cu(I) [47]; moreover, no sign of asymmetries or satellite features that could suggest oxidation to Cu(II) can be seen. The Ce 3d region is reported in figure 4b. Table 1 reveals that the Ce 3d signal attenuates by ~9% after deposition of copper. In contrast, the Au 4f signal attenuates by ~2.5%. This is consistent with some copper being deposited onto gold particles, but the majority of the copper coalescing into pure nanoparticles on the ceria surface. The deposition of copper causes a further decrease in the percentage of Ce(IV) from ca. 88.6% to ca. 83.2%. This is consistent with the behaviour previously reported for the growth of copper on CeO_2 and supports the conclusion that copper particles are formed in direct contact with the ceria surface. [48] A small attenuation of the Au 4f peak indicates that some of the copper also condenses over the preformed Au nanoparticles.

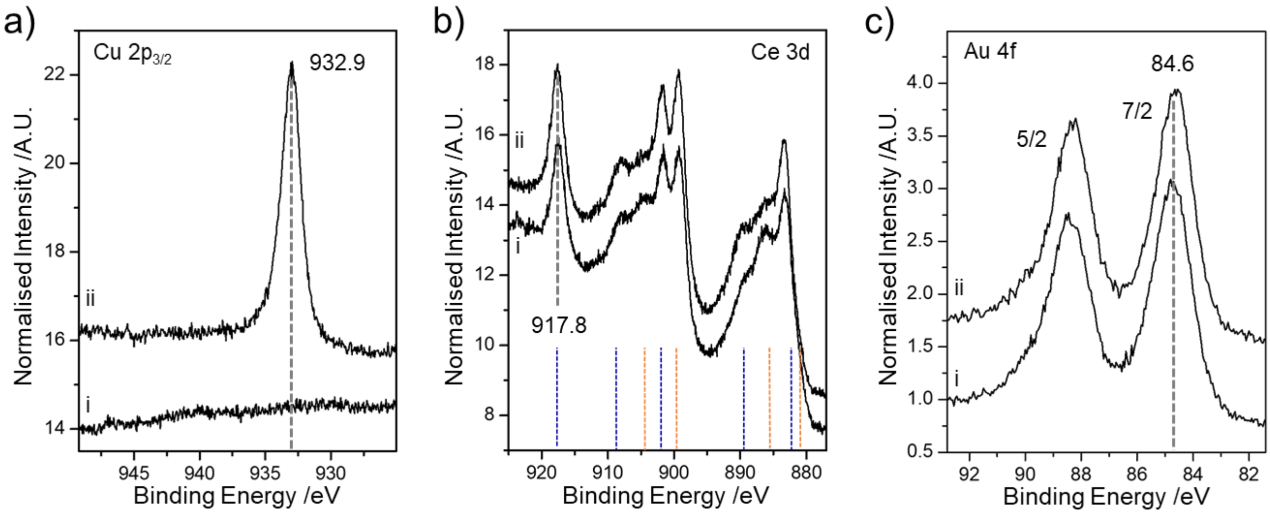

Figure 4. XP spectra of a) the Cu $2p_{3/2}$ region, b) the Ce 3d region and c) the Au 4f region, showing ~1 ML Au/CeO_2/Si(111) i) prior and ii) after deposition of ~1.6 ML Cu at 300 K. In b) expected positions for Ce(IV)/Ce(III) components are indicated by blue/orange dashed lines. Spectra are offset for clarity.

Annealing Cu/Au nanoparticle films on CeO_2/Si(111)

Figure 5 shows Cu $2p_{3/2}$, Ce 3d and Au 4f core levels XP spectra following the annealing of the layer described as above. Additional details, as well as O 1s, C 1s, Si 2p core level spectra, are reported in SI3.1.

The Cu $2p_{3/2}$ is recorded at 933.5 eV and remains essentially constant through the progressively higher annealing temperatures (Figure 5a). The fitting of the Ce 3d region in Figure 5b shows that the Ce(IV):Ce(III) ratio decreases with increasing annealing temperature. Following the highest thermal treatment, the Ce(IV):(III) ratio was found to be ~1:3. Similar behaviour is observed when annealing the CeO_2 thin film on Si(111) (See SI2). This is likely due to transfer of some oxygen from the ceria layer into the silicon substrate and/or desorption of oxygen. [49, 50] The overall intensity of the Ce 3d peaks increases with annealing temperature (Table 2 and Figure 5). Similar behaviour has been observed when annealing a ceria thin film, which was ascribed to a decrease in screening of subsurface cerium atoms when oxygen vacancies are created. [49] Contributions to the increase in the cerium signal could also derive from sintering of the metallic nanoparticles with increasing annealing temperature and from desorption of molecular adsorbates. The Au $4f_{7/2}$ peak, Figure 5c, is recorded at 84.6 eV and remains essentially constant through the annealing treatments. XPS (Table 2 and Figure 5) reveals that there is little change in the intensity of either the Cu $2p_{3/2}$ or Au 4f signals, which suggests that the particle size changes little with increasing annealing temperature.

Table 2. Raw XPS areas (normalised counts and %Ce(IV)) following the annealing of a ~1.6 ML Cu on ~1.0 ML Au on a CeO_2/Si(111) sample.

conditions	**Cu $2p_{3/2}$**	**Ce 3d**	**% Ce(IV)**	**Si 2p**	**Au 4f**
As prep, RT	13.3	83.6	83.2	4.6	8.0
Anneal 325 K	12.9	90.3	84.7	4.6	8.1
Anneal 375 K	12.6	88.5	78.9	4.7	7.8
Anneal 425 K	12.5	102.2	52.3	4.5	8.0
Anneal 475 K	12.6	108.5	44.1	4.2	7.2
Anneal 510 K	13.4	110.3	39.3	3.4	8.7
Anneal 540 K	12.2	122.2	23.5	4.2	7.2

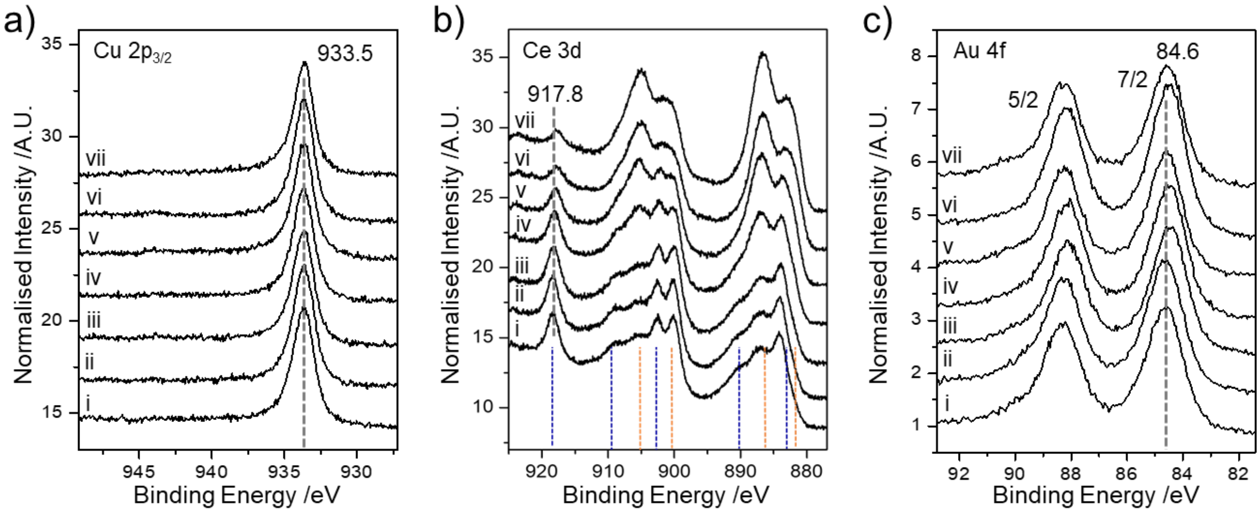

Figure 5. Annealing temperature dependence of XP spectra of the a) Cu $2p_{3/2}$, b) Ce 3d and c) Au 4f core levels for a sample prepared by the deposition of first ~1 ML Au followed by ~1.6 ML onto a ~2 nm CeO_2 film on Si(111) at 300 K; i) as prepared, ii) 325 K, iii) 375 K, iv) 425 K, v) 475 K, vi) 510 K and vii) 540 K. In b) expected positions for Ce(IV)/Ce(III) components are indicated by blue/orange dashed lines. Spectra are offset for clarity.

Cu/Au/CeO_2/Si(111)

MEIS

The PM3 software allowed us to explore several nanoparticle structures such as discrete nanoparticles (NPs), core@shell and alloy, with spherical and hemispherical geometries. In order to evaluate the goodness of the fit for the MEIS spectra the reduced Chi-square analysis was applied.[51] The Chi-square is used as a figure-of-merit for the evaluation of goodness of fit for MEIS spectra. In this work, we used the reduced Chi-square given by Equation 1:

$$\chi^2 = \frac{1}{N}\sum_{i=1}^{N}\left\{\frac{\left[I_{exp} - I_{sim} + min(I_{exp},1)\right]^2}{I_{exp} + 1}\right\} \qquad \text{Eq. 1}$$

where *N* is the total number of data points, I_{exp} and I_{sim}represent the experimental and simulated spectra, respectively.[51] The min(I_{exp},1) factor is used to take into account cases of low counts. Equation 1 was applied to three ion backscattering angles (119.3°, 125.3° and 131.3°) with the same energy range for the analysis presented in this work and the mean Chi-square result was taken.

A sample was prepared by first depositing 0.14 ML Au followed by 0.6 ML Cu onto ~2 nm CeO_2/Si(111) at 300 K. MEIS data were acquired for the as-prepared sample and following annealing the same sample to 350, 425 and 525 K. The Chi-square analysis (inset in Figure 6) reveals that the best fit to the MEIS data (see S4.1) for the as-deposited sample was for discrete NPs of Cu (radius 1.5 nm) and Au (radius 2 nm) adopting a hemispherical shape. Cu nanoparticles were found to cover approximately 10% of the ceria surface, while Au particles covered approximately 2% of the surface. The fit for a core-shell morphology was only marginally less good. The possibility of a mixture of discrete particles and Au(core)@Cu(shell) particles is consistent with our XPS data following a similar sample preparation. On annealing, the particle morphology was found to be relatively stable up to ~425 K. After annealing to 525 K, the PowerMEIS Chi-square analysis now shows approximately similar values for discrete Cu and Au particles; particles with an alloy shell surrounding a Cu core and alloyed ($Au_{0.25}Cu_{0.75}$) particles. The MEIS data are consistent with a clear change occurring compared to the lower annealing temperatures and it is likely that a mixture of particle morphologies and compositions is present under these conditions caused by diffusion, agglomeration and intermixing processes at this elevated temperature. MEIS spectra and PowerMEIS fits are reported in SI4.1.

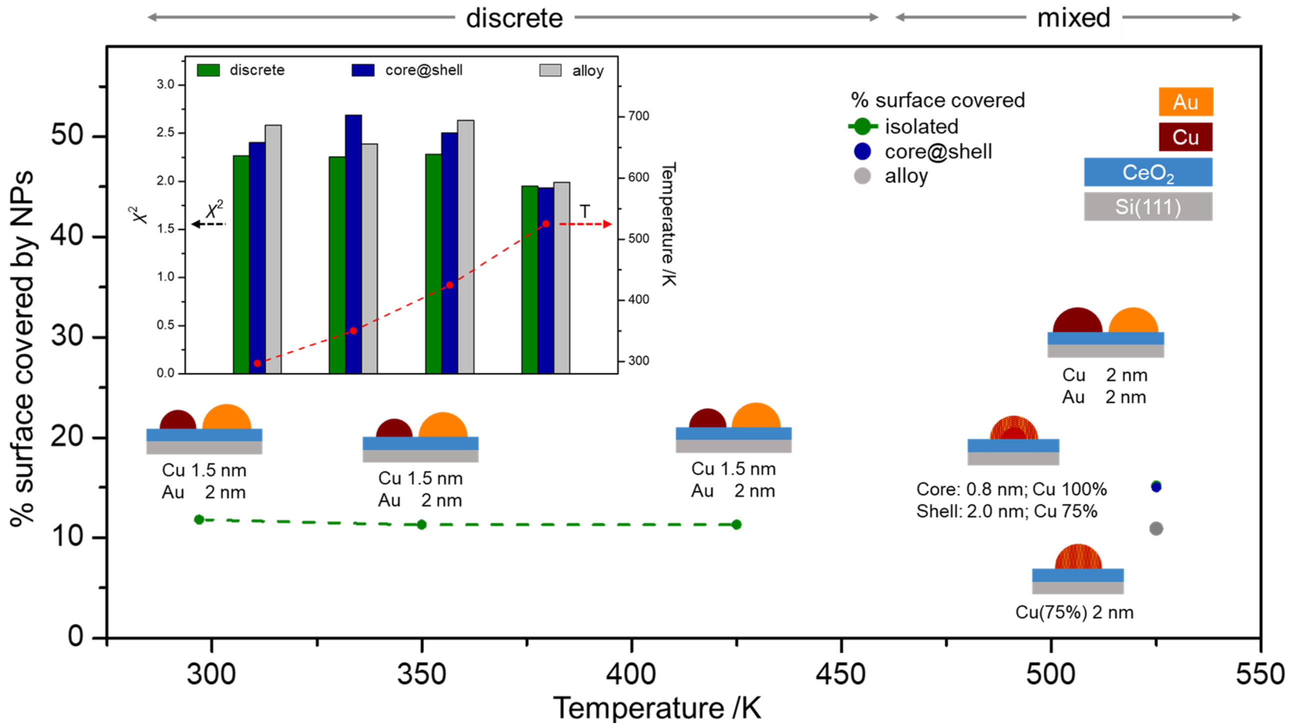

Figure 6. Nanoparticle radii, morphology and % of surface covered by nanoparticles as a function of annealing temperature for the samples prepared by the deposition of 0.14 ML Au followed by 0.6 ML Cu onto a ~2 nm CeO$_2$ film on Si(111) as deposited (~300 K) and annealed to 350, 425 and 525 K. In the inset, Chi-square analysis for the same samples obtained from the three ion backscattering angles (119.3°, 125.3° and 131.3°). Green, blue and grey bars indicate the use of a model with discrete NPs, core@shell and alloy, respectively.

To summarise the XPS and MEIS findings, XPS shows that when vapour depositing gold onto a CeO$_2$(111) film, a small charge transfer occurs on deposition, with cerium being slightly reduced and gold slightly oxidised. On addition of copper, metallic particles are nucleated, but a further reduction of ceria seems to occur. A slight decrease of the Au 4f intensity indicates that some preformed gold particles are coated by a copper layer. On annealing, the Cu 2p$_{3/2}$ and Au 4f peaks stay approximately constant in both binding energy and intensity. Annealing causes an increase in the reduction of CeO$_2$, mimicking the behaviour observed upon annealing the CeO$_2$ films on Si(111). This could indicate that the metal NPs are thermally stable from the XPS point of view and there is minimal interaction with the substrate, with reduction of ceria being ascribed primarily to loss of oxygen. The MEIS analysis is consistent with the XPS results indicating isolated gold nanoparticles are formed on ceria, with subsequent growth of both isolated copper particles and copper particles on pre-formed gold particles upon deposition of copper onto Au/CeO$_2$/Si(111). This morphology remains stable on annealing to 425 K, though increases in particle size and alloy formation are observed following annealing to 525 K.

Influence of annealing on an air-exposed Au/Cu/CeO$_2$/Si(111) sample

XPS

A sample was prepared by the deposition of first ~1.5 ML copper followed by ~1.0 ML gold onto a ~1.5 nm CeO_2 film on Si(111). The sample was exposed to air before being introduced into the XPS chamber for analysis. For these XPS experiments, the monochromated Al k_α source was used. Deposition of copper on the relatively well-defined CeO_2(111) surface has been shown to be initiated at step edges.[52, 53] It has been reported that charge transfer from the oxide to copper species leads to the formation of Cu(I) [2, 45] which are thought to be located at the interface with ceria and covered by Cu(0) species.[54] Gold deposition onto Cu/CeO_2 can result in decoration of pre-existing copper particles or the formation of isolated gold particles or a combination of both effects.

Figure 7a-c show the Cu $2p_{3/2}$, Ce 3d and Au 4f regions as a function of annealing temperature. The annealing temperatures reported are, we believe, accurate to within about 25 K due to difficulties in measuring the sample temperature using this specific sample holder. After deposition of the metal nanoparticles, and subsequent exposure to air, the Cu $2p_{3/2}$ region shows a signal that can be fitted with two components (Figure 7a), one with maximum at a binding energy (BE) of 933.6 eV, attributed to copper in the I/0 oxidation state, and one at 935.5 eV, which is associated with Cu(II).[47, 55]

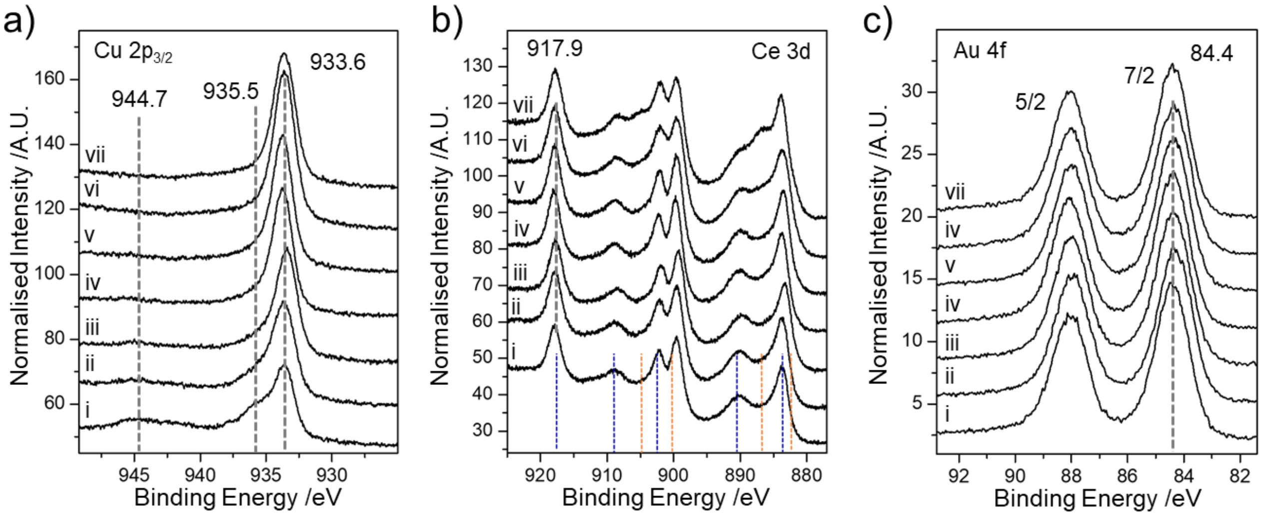

Figure 7. Annealing temperature dependence of XP spectra of the Cu $2p_{3/2}$, Ce 3d and Au 4f core levels for a sample prepared by the deposition of first ~1.5 ML Cu followed by ~1.0 ML Au onto a ~2 nm CeO_2 film on Si(111) at 300 K; i) as prepared, ii) 330 K, iii) 350 K, iv) 370 K, v) 385 K, vi) 400 K and vii) 425 K. In b) expected positions for Ce(IV)/Ce(III) components are indicated by blue/orange dashed lines. Spectra are offset for clarity.

Table 3. Raw XPS areas (normalised counts and %Ce(IV)) from a ~1.0 ML Au on ~1.5 ML Cu on CeO_2/Si(111) after exposure to air and as a function of annealing temperature

conditions	**Cu $2p_{3/2}$**	**Ce 3d**	**% Ce(IV)**	**Si 2p**	**Au 4f**
As prep, RT	60.30	191.61	89.9	19.73	37.02
Anneal 330 K	72.28	234.86	87.6	19.69	37.74
Anneal 350 K	76.47	217.84	91.0	19.27	37.59
Anneal 370 K	77.09	228.43	86.8	20.17	36.40
Anneal 385 K	84.69	269.18	84.6	19.21	36.88
Anneal 400 K	96.76	312.41	88.7	19.52	36.08
Anneal 425 K	60.30	302.89	74.8	19.73	37.02

The raised background at ca. 944 eV is attributed to the shake-up satellite features of Cu(II). A BE of 933.6 eV is approximately 1 eV higher than that typically observed for metallic copper particles.[56] Similar behaviour was reported in XP spectra of small copper particles deposited onto a single crystal ZnO surface where the authors concluded that small copper particles are partially oxidised due to the interaction with the ZnO surface.[57] With annealing to increasing temperature, the signals associated to Cu(II) decrease in intensity, the shake-up satellites attenuate and the lower BE component increases (Figure 7a). Each of these observations imply that the Cu(II) component reduces to Cu(I/0). A small shift of the lower BE peak is observed with increasing annealing temperature.

Figure 7b) shows that after preparation, the Ce 3d region shows the typical signature of cerium in the +IV oxidation state. With annealing, the decrease of the peaks related to Ce(IV) and the corresponding increase of the signals related to Ce(III) are recorded. The overall Ce(IV):Ce(III) composition % goes from ca. 90/10% after preparation to ca. 75/25% after annealing to 425 K. (see Table 3) The Au $4f_{7/2}$ is recorded at 84.4 eV, as shown in Figure 7c. The signal stays constant in position and shape throughout the annealing experiments. As observed for the main peak of copper, also the BE of Au 4f peaks are recorded at slightly higher BE than that expected for metallic gold.[6] Small gold particles have been reported to be partially oxidised on ceria surfaces, but a shift to higher binding energy has also been reported for Cu/Au alloys compared with pure gold.[58, 59]

Table 3 shows the variation of peak area for the Cu $2p_{3/2}$, Ce 3d, Si 2p, and Au 4f signals as a function of temperature obtained from the fitting procedure, and additional details are reported in SI3.2.

The Ce 3d and Cu $2p_{3/2}$ signals are seen to increase in intensity whereas that of Au 4f stays constant overall. On the basis of the XPS data, there are a number of possible interpretations of the variation in Ce 3d, Cu $2p_{3/2}$ and Au 4f intensities with increasing annealing temperature. The increase in the Ce 3d signal may indicate that the metal nanoparticles are sintering with increasing temperature, therefore exposing a larger area of bare ceria. However, one would expect a decrease in the overall intensity of the Cu $2p_{3/2}$ and Au 4f signals, which is not observed. The exposure of the sample to air causes the adsorption of carbon and oxygen containing species (e.g. OH^-, HCO_3^-, CO_3^{2-}). The thermally induced desorption of these species is likely to occur from copper and ceria sites rather than from less reactive gold sites. The deposition of copper onto ceria typically produces hemispherical copper particles.[53] As will be shown below, MEIS indicates that the copper particles have a radius of ~2.5 – 3.0 nm. Assuming a uniform array of particles on the CeO_2 surface, an array of copper particles can be envisaged whose centres are separated by between 10 and 14 nm. The subsequent deposition of gold is likely to result in gold nucleation on top of existing copper particles rather than the formation of isolated gold particles, given that Au-Cu bonds are thermodynamically more favourable than Au/ceria bonds especially when copper particles are already nucleated on the most favourable CeO_2 sites.[52, 53, 60] The relatively constant Au 4f signal as a function of increasing annealing temperature coupled with an increasing Cu $2p_{3/2}$ signal could be interpreted as being due to desorption of molecular species from bimetallic particles and intermixing of gold with copper.

MEIS: Au/Cu/CeO_2/Si(111)

Figure 8 summarizes our findings of the MEIS investigations of the samples when copper is first deposited followed by gold. MEIS spectra and PowerMEIS fits are reported in SI4.2. Figure 8 b) showing the NP's stoichiometry as a function of annealing temperature. After preparation in vacuum, PowerMEIS simulations of the data taken at 300 K indicate that the most likely nanoparticle structure corresponds to hemispherical particles of radius 2.5 nm with a Cu core of radius 1.3 nm and an alloy shell of composition 78% Cu giving an overall particle stoichiometry of ~80% Cu. After air exposure and annealing to 375 K, XPS reveals the presence of significant Cu(II) as well as C and O containing adsorbates. Under these conditions, analysis of the MEIS data reveals the formation of an exclusively Cu shell of thickness 0.6 nm surrounding a bimetallic core of radius 2.2 nm and with a Cu concentration of 45%. Segregation of Cu to the surface induced by exposure to atmospheric oxygen would be expected. PowerMEIS analysis of samples annealed to temperatures above 375 K is consistent with the formation of homogeneous alloy particles of a gradually increasing particle size an whose overall composition becomes slightly richer in gold.

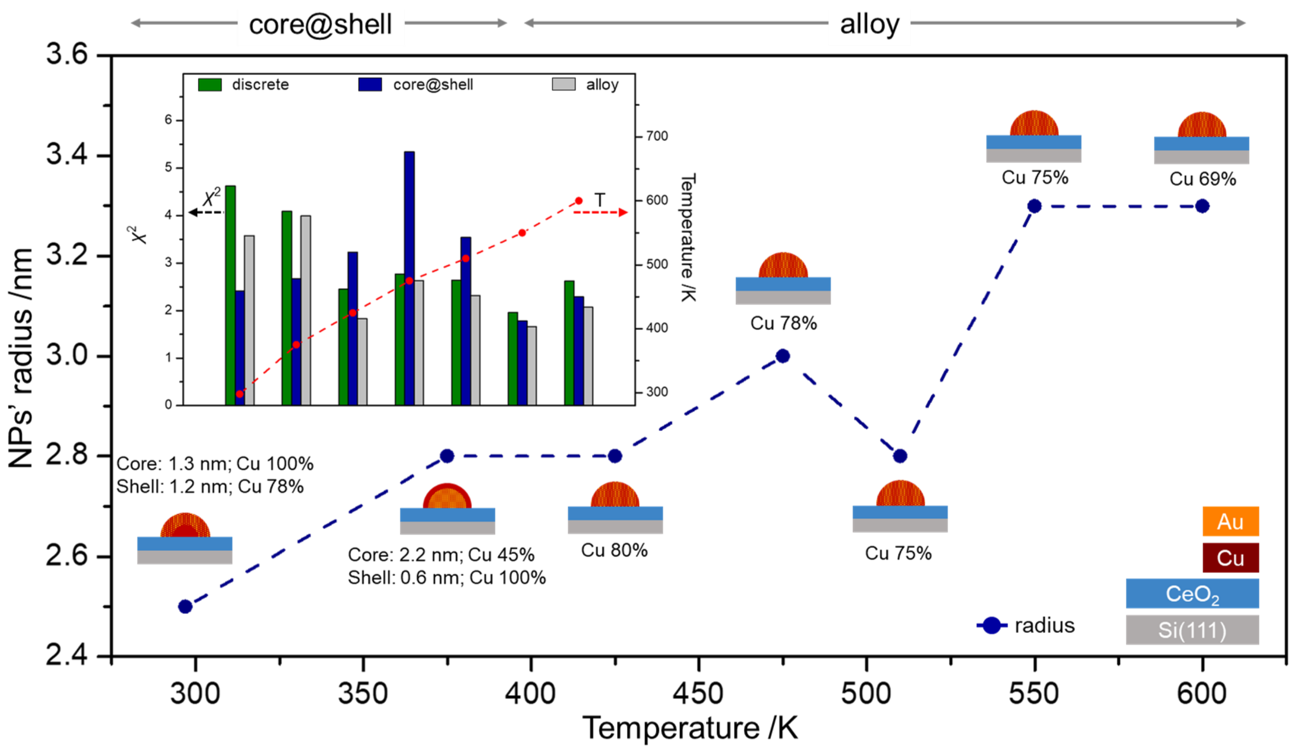

Figure 8. Nanoparticle radius, stoichiometry and morphology as a function of annealing temperature for the samples prepared by the deposition of ~1.5 ML Cu followed by ~1.0 ML Au onto a ~1.5 nm CeO_2 film on Si(111) as deposited and annealed to 375, 425, 475, 510, 550 and 600 K. Composition % is given with respect to Cu. In the inset, Chi-square analysis for the same samples obtained from the three ion backscattering angles (119.3°, 125.3° and 131.3°). Green, blue and grey bars indicate the use of a model with discrete NPs, core@shell and alloy, respectively.

Conclusions

A preparation method has been established for producing Au/Cu/CeO_2 model catalysts for analysis by MEIS consisting of a ~2 nm CeO_2 film deposited onto Si(111) followed by metal vapour deposition of elemental Cu and Au.

XPS reveals that the ceria film is initially almost pure CeO_2 in composition. On annealing a CeO_2/Si(111) sample, a gradual reduction is observed caused presumably by a combination of oxygen desorption and diffusion of oxygen into the Si substrate.

Deposition of Au onto the CeO_2/Si(111) surface at 300 K leads to a slightly lower Ce(IV):Ce(III) ratio. Deposition of Cu onto the precovered Au/CeO_2/Si(111) surface leads to further Ce(IV) reduction. In addition, a slight attenuation of the Au signal is observed. These observations are consistent with the formation of mainly pure Au and pure Cu particles with some Cu deposition onto Au particles. PowerMEIS analysis supports this conclusion, with the best fit to the MEIS data corresponding to discrete hemispherical Au (radius 2 nm) and Cu (radius 1.5 nm) particles. These particles are relatively thermally stable up to at least 450 K. The most physically realistic model for the sample after annealing to 525 K involves the formation of hemispherical alloyed CuAu particles (radius 2 nm).

A sample prepared by deposition of Cu followed by Au onto CeO_2/Si(111) was exposed to air. XPS revealed the presence of Cu(II) species following air exposure which are reduced to Cu/Cu(I) with increasing annealing temperature. Annealing to 375 K caused desorption of weakly bound adsorbates and MEIS revealed that under these conditions the sample consisted of nanoparticles with a Au rich core and a Cu rich shell. Annealing to higher temperatures resulted in the formation of alloyed particles. MEIS revealed that initially core-shell particles were produced after deposition of Cu followed by Au in vacuum. On exposure to air, Cu segregation to the surface was observed. Annealing to higher temperatures produced MEIS data that were consistent with the formation of homogeneously alloyed particles.

The powerful combination of XPS and MEIS allows significant insight into the thermal behaviour of Cu and Au particles on the ceria surface providing information on alloying behaviour, particle size and the electronic interaction with the CeO_2 support material.

Acknowledgements

RM and FG acknowledge funding from EPSRC grants (RM: EP/506631/1; FG: EP/M029077/1). JAvdB and AR acknowledge the EPSRC funding for the use of the MEIS facility at the University of Huddersfield within grant EP/M029077/1. This study was financed in part by the Coordenação de Aperfeiçoamento de Pessoal de Nível Superior - Brasil (CAPES) - Finance Code 001, by Conselho Nacional de Desenvolvimento Científico e Tecnológico (CNPq), and PRONEX-FAPERGS 16/2551-0000479-0.

The research data supporting this publication can be accessed at http://dx.doi.org/ to be added upon acceptance.

Supporting material description: fitting of Ce 3d XPS region; XPS of CeO_2/Si(111) with annealing; XPS of (Cu+Au)/CeO_2/Si(111) with annealing; MEIS spectra and respective PowerMEIS fits of (Cu+Au)/CeO_2/Si(111) with annealing

References

[1] A. T. Bell, The impact of nanoscience on heterogeneous catalysis, Science, 299 (2003) 1688-1691.

[2] M. M. Branda, N. C. Hernandez, J. F. Sanz, F. Illas, Density Functional Theory Study of the Interaction of Cu, Ag, and Au Atoms with the Regular CeO_2 (111) Surface, Journal of Physical Chemistry C, 114 (2010) 1934-1941.

[3] A. Trovarelli, Catalytic properties of ceria and CeO_2-containing materials, Catal. Rev.-Sci. Eng., 38 (1996) 439-520.

[4] J. Kaspar, P. Fornasiero, M. Graziani, Use of CeO_2-based oxides in the three-way catalysis, Catalysis Today, 50 (1999) 285-298.

[5] L. J. Chen, Y. H. Tang, L. X. Cui, C. Y. Ouyang, S. Q. Shi, Charge transfer and formation of Ce^{3+} upon adsorption of metal atom M (M = Cu, Ag, Au) on CeO_2 (100) surface, Journal of Power Sources, 234 (2013) 69-81.

[6] M. Baron, O. Bondarchuk, D. Stacchiola, S. Shaikhutdinov, H. J. Freund, Interaction of Gold with Cerium Oxide Supports: CeO_2(111) Thin Films vs CeO_x Nanoparticles, Journal of Physical Chemistry C, 113 (2009) 6042-6049.

[7] F. Tao, S. R. Zhang, L. Nguyen, X. Q. Zhang, Action of bimetallic nanocatalysts under reaction conditions and during catalysis: evolution of chemistry from high vacuum conditions to reaction conditions, Chemical Society Reviews, 41 (2012) 7980-7993.

[8] E. Völker, F. J. Williams, E. J. Calvo, T. Jacob, D. J. Schiffrin, O2 induced Cu surface segregation in Au–Cu alloys studied by angle resolved XPS and DFT modelling, Physical Chemistry Chemical Physics, 14 (2012) 7448-7455.

[9] N. Artrith, A. M. Kolpak, Grand canonical molecular dynamics simulations of Cu-Au nanoalloys in thermal equilibrium using reactive ANN potentials, Computational Materials Science, 110 (2015) 20-28.

[10] N. Artrith, A. M. Kolpak, Understanding the Composition and Activity of Electrocatalytic Nanoalloys in Aqueous Solvents: A Combination of DFT and Accurate Neural Network Potentials, Nano Letters, 14 (2014) 2670-2676.

[11] X. M. Liao, V. Pitchon, P. H. Cuong, W. Chu, V. Caps, Hydrogenation of cinnamaldehyde over bimetallic Au-Cu/CeO_2 catalyst under a mild condition, Chinese Chemical Letters, 28 (2017) 293-296.

[12] X. M. Liao, W. Chu, X. Y. Dai, V. Pitchon, Bimetallic Au-Cu supported on ceria for PROX reaction: Effects of Cu/Au atomic ratios and thermal pretreatments, Applied Catalysis B-Environmental, 142 (2013) 25-37.

[13] R. Fiorenza, C. Crisafulli, G. G. Condorelli, F. Lupo, S. Scire, Au-Ag/CeO_2 and Au-Cu/CeO_2 Catalysts for Volatile Organic Compounds Oxidation and CO Preferential Oxidation, Catalysis Letters, 145 (2015) 1691-1702.

[14] L. Zhang, H. Y. Kim, G. Henkelman, CO Oxidation at the Au-Cu Interface of Bimetallic Nanoclusters Supported on CeO_2(111), Journal of Physical Chemistry Letters, 4 (2013) 2943-2947.

[15] N. K. Gamboa-Rosales, J. L. Ayastuy, M. P. Gonzalez-Marcos, M. A. Gutierrez-Ortiz, Oxygen-enhanced water gas shift over ceria-supported Au-Cu bimetallic catalysts prepared by wet impregnation and deposition-precipitation, International Journal of Hydrogen Energy, 37 (2012) 7005-7016.

[16] B. B. Chen, X. M. Li, R. J. Zheng, R. P. Chen, X. Sun, Bimetallic (Au-Cu core)@(ceria shell) nanotubes for photocatalytic oxidation of benzyl alcohol: improved reactivity by Cu, Journal of Materials Chemistry A, 5 (2017) 13382-13391.

[17] C. Pojanavaraphan, A. Luengnaruemitchai, E. Gulari, Catalytic activity of Au-Cu/CeO_2-ZrO_2 catalysts in steam reforming of methanol, Applied Catalysis a-General, 456 (2013) 135-143.

[18] C. Pischetola, L. Collado, M. A. Keane, F. Cardenas-Lizana, Gas Phase Hydrogenation of Furaldehydes via Coupling with Alcohol Dehydrogenation over Ceria Supported Au-Cu, Molecules, 23 (2018).

[19] R. F. Zhang, X. F. Kong, H. T. Wang, S. H. Zhang, D. Legut, S. H. Sheng, S. Srinivasan, K. Rajan, T. C. Germann, An informatics guided classification of miscible and immiscible binary alloy systems, Scientific Reports, 7 (2017) 9577.

[20] W. B. Pearson, Handbook of Lattice Spacings and Structures of Metals and Alloys (Pergamon, London, 1958).

[21] J. Hennig, D. Mari, R. Schaller, Order-disorder phase transition and stress-induced diffusion in Au-Cu, Physical Review B, 79 (2009) 144116.

[22] Y. Feutelais, B. Legendre, M. Guymont, New enthalpies determination and in situ X-ray diffraction observations of order/disorder transitions in $Au_{0.5}Cu_{0.5}$, Acta Materialia, 47 (1999) 2539-2551.

[23] X. Zhao, P. Liu, J. Hrbek, J.A. Rodriguez, M. Pérez, The chemisorption of SO_2 on the Cu/Au(111) surface: Interplay between ensemble and electronic effects, Surface Science, 592 (2005) 25-36.

[24] L. Wang, P. Li, H. Shi, Z. Li, K. Wu, X. Shao, Thickness-Dependent Adsorption of Melamine on Cu/Au(111) Films, The Journal of Physical Chemistry C, 121 (2017) 7977-7984.

[25] F. Grillo, R. Megginson, D. Batchelor, M. Muntwiler, C. J. Baddeley, Structural and electronic characterization of Cu/Au(111) near-surface alloys, Japanese Journal of Applied Physics, 58 (2019) 5.

[26] F. Grillo, R. Megginson, J. Christie, S. M. Francis, N. V. Richardson, C. J. Baddeley, Structure and Reactivity of Cu-doped Au(111) Surfaces, e-Journal of Surface Science and Nanotechnology, 16 (2018) 163-171.

[27] F. Grillo, H. Früchtl, S. M. Francis, N. V. Richardson, Site selectivity in the growth of copper islands on Au (111), New Journal of Physics, 13 (2011).

[28] Q. Liu, Y. Ning, W. Huang, Q. Fu, F. Yang, X. Bao, Origin of the Thickness-Dependent Oxidation of Ultrathin Cu Films on Au(111), The Journal of Physical Chemistry C, 122 (2018) 8364-8372.

[29] W. Wang, H. Shi, L. Wang, Z. Li, H. Shi, K. Wu, X. Shao, Comparison Study of Structural Properties and CO Adsorption on the Cu/Au(111) and Au/Cu(111) Thin Films, The Journal of Physical Chemistry C, 122 (2018) 19551-19559.

[30] S. Deckers, F. Habraken, W. F. Vanderweg, A. W. D. Vandergon, J. F. Vanderveen, J. W. Geus, Oxidation-induced segregation at the $Pt0_{.5}Ni_{0.5}$(111) surface studied by medium energy ion scattering, G, Applied Surface Science, 45 (1990) 121-129.

[31] C. J. Baddeley, L. H. Bloxham, S. C. Laroze, R. Raval, T. C. Q. Noakes, P. Bailey, Quantitative analysis of adsorbate induced segregation at bimetallic surfaces: Improving the accuracy of medium energy ion scattering results, Journal of Physical Chemistry B, 105 (2001) 2766-2772.

[32] V. Z. C. Paes, M. V. Castegnaro, D. L. Baptista, P. L. Grande, J. Morais, Unveiling the Inner Structure of PtPd Nanoparticles, Journal of Physical Chemistry C, 121 (2017) 19461-19466.

[33] D. F. Sanchez, R. Moiraghi, F. P. Cometto, M. A. Perez, P. F. P. Fichtner, P. L. Grande, Morphological and compositional characteristics of bimetallic core@shell nanoparticles revealed by MEIS, Applied Surface Science, 330 (2015) 164-171.

[34] M. A. Sortica, P. L. Grande, G. Machado, L. Miotti, Characterization of nanoparticles through medium-energy ion scattering, Journal of Applied Physics, 106 (2009).

[35] J. Gustafson, A. R. Haire, C. J. Baddeley, Depth-profiling the composition of bimetallic nanoparticles using medium energy ion scattering, Surface Science, 605 (2011) 220-224.

[36] G. G. Marmitt, PowerMEIS-3 simulation code, http://tars.if.ufrgs.br/.

[37] G. G. Marmitt, Metal oxides of resistive memories investigated by electron and ion backscattering, Ph.D. thesis, Universidade Federal do Rio Grande do Sul, Porto Alegre (2017), https://lume.ufrgs.br/handle/10183/170451.

[38] J. F. Ziegler, J. P. Biersack, U. Littmark, The Stopping and Range of Ions in Solids, vol. 1 of The Stopping and Ranges of Ions in Matter: Stopping tables SRIM 97 (Pergamon Press, New York, 1985).

[39] W. K. Chu, Calculation of energy straggling for protons and helium ions, Physical Review A, 13 (1976) 2057-2060.

[40] J. B. Marion, F. C. Young, Nuclear Reaction Analysis, Graphs and Tables (North Holland Publishing Company, Amsterdam, 1968).

[41] H. Trombini, G. G. Marmitt, I. Alencar, D. L. Baptista, S. Reboh, F. Mazen, R. B. Pinheiro, D. F. Sanchez, C. A. Senna, B. S. Archanjo, C. A. Achete, P. L. Grande, Unraveling structural and compositional information in 3D FinFET electronic devices, Scientific Reports, 9 (2019).

[42] X. C. Zheng, X. L. Zhang, Z. Y. Fang, X. Y. Wang, S. R. Wang, S. H. Wu, Characterization and catalysis studies of CuO/CeO_2 model catalysts, Catalysis Communications, 7 (2006) 701-704.

[43] P. Burroughs, A. Hamnett, A. F. Orchard, G. Thornton, Satellite structure in the X-ray photoelectron spectra of some binary and mixed oxides of lanthanum and cerium, Journal of the Chemical Society, Dalton Transactions, (1976) 1686-1698.

[44] J. L. Lu, H. J. Gao, S. Shaikhutdinov, H. J. Freund, Gold supported on well-ordered ceria films: nucleation, growth and morphology in CO oxidation reaction, Catalysis Letters, 114 (2007) 8-16.

[45] Y. H. Tang, H. Zhang, L. X. Cui, C. Y. Ouyang, S. Q. Shi, W .H. Tang, H. Li, L. Q. Chen, Electronic states of metal (Cu, Ag, Au) atom on CeO_2(111) surface: The role of local structural distortion, Journal of Power Sources, 197 (2012) 28-37.

[46] N. C. Hernández, R. Grau-Crespo, N. H. de Leeuw, J. F. Sanz, Electronic charge transfer between ceria surfaces and gold adatoms: a GGA+U investigation, Physical Chemistry Chemical Physics, 11 (2009) 5246-5252.

[47] M. C. Biesinger, Advanced analysis of copper X-ray photoelectron spectra, Surf. Interface Anal., 49 (2017) 1325-1334.

[48] G. H. Li, S. W. Hu, Q. Xu, J. F. Zhu, Interaction between Cu Nanoparticles and CeO_2(111) Film Surfaces, Journal of Physical Chemistry C, 123 (2019) 23563-23571.

[49] P. Sapkota, A. Aprahamian, K. Y. Chan, B. Frentz, K. T. Macon, S. Ptasinska, D. Robertson, K. Manukyan, Irradiation-induced reactions at the $CeO_2/SiO_2/Si$ interface, The Journal of Chemical Physics, 152 (2020) 104704.

[50] M. Vorokhta, I. Matolinova, M. Dubau, S. Haviar, I. Khalakhan, K. Sevcikova, T. Mori, H. Yoshikawa, V. Matolin, HAXPES study of CeOx thin film-silicon oxide interface, Applied Surface Science, 303 (2014) 46-53.

[51] K. J. Mighell, Parameter estimation in astronomy with Poisson-distributed data. I. The χ_γ^2 statistic, Astrophys. J., 518 (1999) 380-393.

[52] T. E. James, S. L. Hemmingson, C. T. Campbell, Energy of Supported Metal Catalysts: From Single Atoms to Large Metal Nanoparticles, ACS Catalysis, 5 (2015) 5673-5678.

[53] T. E. James, S. L. Hemmingson, T. Ito, C. T. Campbell, Energetics of Cu Adsorption and Adhesion onto Reduced CeO_2(111) Surfaces by Calorimetry, The Journal of Physical Chemistry C, 119 (2015) 17209-17217.

[54] L. Szabova, T. Skala, I. Matolinova, S. Fabris, M. F. Camellone, V. Matolin, Copper-ceria interaction: A combined photoemission and DFT study, Applied Surface Science, 267 (2013) 12-16.

[55] D. Tahir, S. Tougaard, Electronic and optical properties of Cu, CuO and Cu_2O studied by electron spectroscopy, Journal of Physics-Condensed Matter, 24 (2012).

[56] Y. T. Wu, E. Garfunkel, T. E. Madey, Initial stages of Cu growth on ordered Al_2O_3 ultrathin films, Journal of Vacuum Science & Technology a-Vacuum Surfaces and Films, 14 (1996) 1662-1667.

[57] M. C. Patterson, X. Nie, F. Wang, R. L. Kurtz, S. B. Sinnott, A. Asthagiri, P. T. Sprunger, Growth and Structure of Cu and Au on the Nonpolar ZnO($10\bar{1}0$) Surface: STM, XPS, and DFT Studies, The Journal of Physical Chemistry C, 117 (2013) 18386-18397.

[58] T .K. Sham, A. Hiraya, M. Watanabe, Electronic structure of Cu-Au alloys from the Cu perspective: A Cu $L_{3,2}$-edge study, Physical Review B, 55 (1997) 7585-7592.

[59] M. Kuhn, T. K. Sham, Charge redistribution and electronic behavior in a series of Au-Cu alloys, Physical Review B, 49 (1994) 1647-1661.

[60] S. L. Hemmingson, C. T. Campbell, Trends in Adhesion Energies of Metal Nanoparticles on Oxide Surfaces: Understanding Support Effects in Catalysis and Nanotechnology, ACS Nano, 11 (2017) 1196-1203.

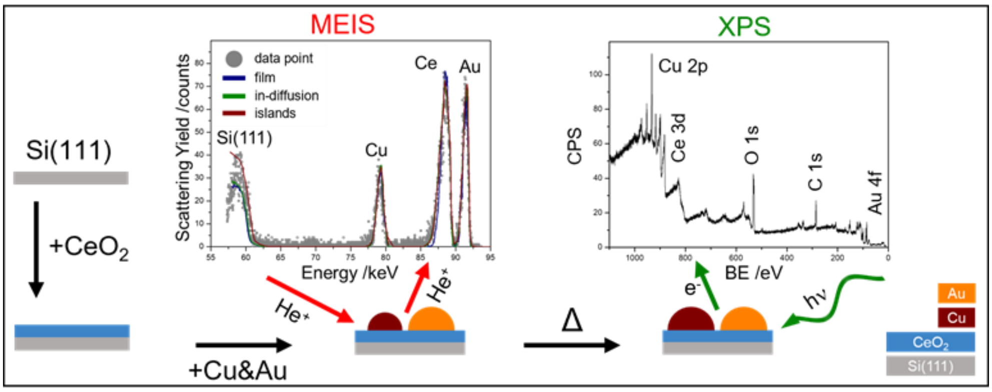
MEIS
XPS
Si(111)
+CeO$_2$
+Cu&Au
Δ
Scattering Yield /counts
0
10
20
30
40
50
60
70
80
data point
film
in-diffusion
islands
Si(111)
Cu
Ce
Au
55
60
65
70
75
80
85
90
95
Energy /keV
He$^+$
He$^+$
CPS
0
20
40
60
80
100
Cu 2p
Ce 3d
O 1s
C 1s
Au 4f
1000
800
600
400
200
0
BE /eV
e$^-$
hν
Au
Cu
CeO$_2$
Si(111)

Declaration of interests

☒ The authors declare that they have no known competing financial interests or personal relationships that could have appeared to influence the work reported in this paper.

☐The authors declare the following financial interests/personal relationships which may be considered as potential competing interests:

University of St Andrews

Professor C. J. Baddeley
EaStCHEM School of Chemistry

11 August 2021

Dear Professor Rudolph

I have submitted a paper entitled "*Thermal behaviour of Cu and Au nanoparticles grown on CeO_2 thin films"* by R. Megginson, F. Grillo, S. M. Francis, V. Z. C. Paes, H. Trombini, P. L. Grande, A. K. Rossall, J. A. van den Berg and C. J. Baddeley

In this manuscript, we combine the techniques of atomic force microscopy, X-ray photoelectron spectroscopy and medium energy ion scattering to investigate the growth of copper and gold nanoparticles on thin cerium oxide films on Si(111) serving as model systems for ceria supported Cu/Au catalysts. This system is chosen as a model system in order to provide insight into how the catalytic properties of Cu/Au/CeO_2 depend on the presence of discrete Cu and Au particles versus fully intermixed Cu/Au systems. XPS is an excellent surface analytical technique for probing the electronic properties of catalytic systems. When a mixture of pure metallic and alloyed particles is present, it is more difficult to extract information from XPS given that it is a spatial averaging technique. Recently, MEIS has been exploited to investigate the depth-dependent composition of nanoparticles on planar surfaces. Herein, we examine the thermal stability, morphology and nanoparticle composition following the deposition of Cu and Au nanoparticles onto CeO_2 thin films for samples that have been maintained in an ultrahigh vacuum environment and exposed to air.

We hope that the paper is of interest and acceptable for publication in Applied Surface Science
Yours sincerely,

Professor Christopher J Baddeley

Professor H Rudolph
Editor-in-chief
Applied Surface Science

Purdie Building, North Haugh, St Andrews, Fife KY16 9ST
Direct Line: +44 (0)1334 467236 School Office: +44 (0)1334 463800 Fax: +44 (0)1334 463808
e-mail: cjb14@st-andrews.ac.uk WWW: http://ch-www.st-andrews.ac.uk

Highlights

- established method to prepare Cu/Au/ceria model catalysts for analysis by MEIS/XPS

- discrete Cu and Au nanoparticles are thermally stable on ceria surface

- MEIS detects oxygen induced surface segregation of copper in Cu/Au nanoparticles

CRediT offers authors the opportunity to share an accurate and detailed description of their diverse contributions to the published work.

- The corresponding author is responsible for ensuring that the descriptions are accurate and agreed by all authors.
- The role(s) of all authors should be listed, using the relevant above categories.
- Authors may have contributed in multiple roles.
- CRediT in no way changes the journal's criteria to qualify for authorship.

CRediT statements should be provided during the submission process and will appear above the acknowledgement section of the published paper

Check criteria/categories on website

R. Megginson: investigation, methodology

F. Grillo: investigation, formal analysis, visualization

S. M. Francis: investigation

V. Z. C. Paes: formal analysis

H. Trombini: formal analysis

P. L. Grande: formal analysis, funding acquisition, writing - Original Draft

A. K. Rossall: investigation, resources

J. A. van den Berg: investigation, resources, writing - Original Draft

C. J. Baddeley: conceptualisation; writing – original draft; project admin; funding acquisition

emails and ORCIDiD

name	email	ORCIDiD
R. Megginson	rm265@st-andrews.ac.uk	
F. Grillo	fg11@st-andrews.ac.uk	0000-0001-9961-1212
S. M. Francis	smf6@st-andrews.ac.uk	
V. Z. C. Paes	vzeizer@hotmail.com	0000-0001-5413-6075
H. Trombini	trombinifis@gmail.com	0000-0002-7254-4774
P. L. Grande	grande@if.ufrgs.br	0000-0003-0199-0520
A. K. Rossall	A.Rossall@hud.ac.uk	0000-0002-0123-8163

J. A. van den Berg	J.VanDenBerg@hud.ac.uk	0000-0003-2527-2523
C. J. Baddeley	cjb14@st-andrews.ac.uk	0000-0001-9750-6494

University of St Andrews

Professor C. J. Baddeley
EaStCHEM School of Chemistry

30 September 2021

Dr. Alfredo Juan, PhD
Editor - Applied Surface Science

Dear Dr Juan,

Ms. Ref. No.: APSUSC-D-21-10023
Title: Thermal behaviour of Cu and Au nanoparticles grown on CeO_2 thin films

We are very grateful for your evaluation of our manuscript for its suitability for Applied Surface Science, and to the reviewers for providing their feedback. Please find below our response to each point raised by the reviewers. Our responses and proposed changes to the manuscript are indicated in red text. We hope that our revised manuscript is now acceptable for publication in Applied Surface Science.

Yours sincerely

Professor Christopher J Baddeley

Reviewers' comments

Reviewer #2: Precisely charactering the surface structures of the bimetallic particles supported on a functional oxide is important for revealing the active centers of a bimetal catalyst as well as understanding the reaction mechanism. In this work, the authors have performed systematic measurements of XPS in combination with MEIS, to investigate the distributions and alloyed structures of the Cu/Au bimetallic particles decorated on an ultrathin Ceria/Si(111) film under different annealing and exposure conditions. The detailed analyses of the spectroscopy results, particularly the MEIS data, clearly evidenced the charge transfer at the metal/oxide interface, the recipe-dependent Cu-Au distribution over the ceria surface as well as the variable surface segregation of the Cu-Au bimetallic particle against the experimental conditions. The sophisticated data have been well organized and clearly presented. The power of the MEIS technique in characterizing the surface structures of the supported bimetallic particles is fruitful and encouraging. Therefore, I think the manuscript is publishable. But a major revision is necessary as some of the experimental points may have to be clarified or corrected before publishing.

Authors' reply: We thank the reviewer for their feedback; actions taken are reported below each of the point the reviewer has raised.

(1) The most attractive aspect of the sample, to me, is that the ceria film was prepared via solution deposition method followed by the annealing in air. As the authors did not mention

any treatment of the sample before metal deposition, I would take the ceria surface exposed to air and covered with various adsorbates such as H2O, CO2 etc. Will these pre-adsorbates affect the nucleation of either Cu or Au clusters? Is that the reason why the ceria gets reduced upon metal deposition since the adsorbates got desorbed under the collision of the metal atoms? Please at least add comments or explanations around these issues.

Authors' reply:
No pre-treatment was done on the ceria layers, apart from being in UHV conditions where any weakly bound material will desorb. We evaluated the stability of the unloaded ceria layers upon annealing for comparison with the metal loaded systems, as reported in SI. We have no means to determine whether adsorbates are removed upon deposition of metal atoms. We speculate that the presence of adsorbates could result in oxidation of metal species, however, we are more keen to attribute the small degree of oxidation of the metallic species to charge transfer between the metals and the ceria layer as it is well known from the literature that charge transfer can occur on deposition. Any oxygen containing species would have resulted in a signal to the higher BE side of the O 1s peak, which we do not see. We do see some oxidation of the Cu particles when exposed to atmosphere. The Cu reduces on annealing in UHV.

(2) The authors present an AFM image of the as-prepared ceria film, which gives the readers the impression that the as-grown ceria film is not continuous but composed of discrete islands. However, is the morphology really reflecting the corrugation of the ceria film instead of the si(111) substrate after a series solution process and air annealing treatments? I would suggest the authors to provide an AFM measurement of the blank sample, to exclude the influence of the formation of the SiO2 layer over the substrate. In addition, the profile analysis in Fig. 1b actually cannot prove the film thickness of ceria since if there is no clear reference of the substrate level.

Authors' reply: We have removed the line profile from Figure 1, as this may have created confusion. We agree with the reviewer that we cannot give an accurate estimate of the CeO_2 layer thickness based on the line profile, because a clear area of substrate is not visible. In fact, we do not estimate the thickness from the line profile. The calculation of 5-6 layer thickness comes from the attenuation of the Si peak from XPS and from the analysis of the Ce signal in the MEIS spectra. The AFM confirms that the surface is smooth, consisting of grains of an average size of ca 23 nm in diameter. The MEIS and XPS data are consistent with a CeO_2 layer of average thickness ca. 2 nm.
Regarding an AFM scan of the Si substrate, at present we are not in the position to perform such analysis.
ACTION: FIGURE 1 AMENDED

More details for the experiments may need to be provided, such as, what is the base pressure of the UHV (both xps and MEIS measurements) system? How did the author determine the evaporation rate of Cu and Au? How did the authors align the crystal direction of the Si(111) substrate during the MEIS measurements? Is the Si(111) wafer doped or undoped?

Authors' reply:

- Base pressures of XPS preparation chamber/anode *ca.* 1×10^{-9} mbar, XPS analyser *ca.* 5×10^{-10} mbar, MEIS *ca.* 5×10^{-10} mbar.
- Evaporation rates were estimated as ca. 0.03 ML min^{-1} for copper and ca. 0.04 ML min^{-1} for gold, as determined via XPS from both the attenuation of the Si 2p peak and the growth of the Cu 2p/Au 4f peaks, by deposition on clean Si(111) wafers.
- Regarding the Si(111) substrates alignment procedure in MEIS, this is a standard Ion Beam Analysis procedure. It is done by changing the 3 sample angles (rotation, spin and tilt) over small ranges while looking for the minimum backscattering yield which indicates alignment.
- The Si(111) substrates from International Wafer Service are p/B doped.

ACTION: THE REQUESTED ADDITIONAL EXPERIMENTAL DETAILS HAVE BEEN ADDED.

(4) On page 8, the subhead "Investigation of the effect of variable CeO2 film thickness on MEIS spectra" seems not correctly describe the content of the following paragraph, as the authors were actually discussing the influence of the structure and/or morphology instead of the thickness of the ceria film over the fitting of the MEIS spectrum.

Authors' reply: as suggested by the reviewer, the subheading has been changed from "Investigation of the effect of variable CeO_2 film thickness on MEIS spectra." to "Investigation of the effect of variable CeO_2 film thickness and morphology on MEIS spectra."
ACTION: HEADING AMENDED

(5) On page 16, the authors found "the BE of Au 4f peaks are recorded at slightly higher BE than that expected for metallic gold" and they try to explain this shift by "Small gold particles have been reported to be partially oxidised on ceria surfaces" or "but a shift to higher binding energy has also been reported for Cu/Au alloys compared with pure gold". However, on page 8, they claim "The Au 4f7/2 peak is recorded at 84.6 eV,…a value in good agreement with that expected for metallic gold, 84.0 eV". Such obvious inconsistency should be corrected.

Authors' reply: to rectify the inconsistency, we rephrased "in good agreement" to "slightly higher than" at the end of page 8.
ACTION: TEXT AMENDED

(6) In the first paragraph of the introduction, the authors state "Our interest in Cu/Au/CeO2 stems…In this application, it is believed to be desirable to maintain separate Cu and Au particles on the oxide surface." I would suggest that the authors may come back to this point at the end of the manuscript, to add some comments of short discussions on the application or promotion of the Cu-Au-CeO2 catalyst in the selective hydrogenation of furfural or related reactions.

Authors' reply: We thank the reviewer for this suggestion. The following comment has been added to the discussion "This work suggests that discrete Cu and Au particles are stable up to 450 K on the CeO_2 surface. When preparing Cu/Au/CeO_2 catalysts for selective hydrogenation of furfural, the thermal treatment of the catalyst should be carefully considered in order to minimise alloy formation."
ACTION: TEXT AMENDED

Reviewer #3: The main aim of the revised work is related to the formation of a CeO2 thin film deposited on silicon, whose performance as a catalyst could be improved by depositing Au and Cu nanoparticles. In this work authors show that depending on what is first deposited, i.e., Au or Cu , the nanoparticles can stay on the CeO2 surface as isolated nanoparticles, as an alloy or in a core-shell configuration. On the basis of XPS and MEIS (medium energy ion scattering) results authors propose a model describing the formation of the samples at different values of temperature. The present work shows interesting results that could be useful to understand the behavior of this type of materials, and I consider that it could be published as is.
Authors' reply: We thank the reviewer for their feedback: no action needed.

Thermal behaviour of Cu and Au nanoparticles grown on CeO_2 thin films

R. Megginson[1], F. Grillo[1], S. M. Francis[1], V. Z. C. Paes[2], H. Trombini[2], P. L. Grande[2], A. K. Rossall[3], J. A. van den Berg[3], C. J. Baddeley[1]*

1. EaStCHEM School of Chemistry, University of St Andrews, North Haugh, St Andrews, Fife, KY16 9ST, United Kingdom
2. Laboratório de Implantação Iônica, Universidade Federal do Rio Grande Sul UFRGS, Instituto de Física, Av. Bento Goncalves 9500, BR-91501970 Porto Alegre, RS, Brazil
3. MEIS Facility - Ion Beam Centre; School of Computing and Engineering, University of Huddersfield, Huddersfield, HD1 3DH, United Kingdom

* email cjb14@st-andrews.ac.uk

Abstract:

Bimetallic catalysts are often more active and/or selective than their monometallic counterparts. The behaviour of such catalysts is frequently strongly dependent on the molar ratio of the two elements as well as nanoparticle size and the interaction with the support material. X-ray photoelectron spectroscopy (XPS) is an excellent surface analytical technique for probing the electronic properties of catalytic systems. When a mixture of pure and alloyed particles is present, it is more difficult to extract information from XPS given that it is a spatial averaging technique. Recently, the technique of medium energy ion scattering (MEIS) has been exploited to investigate the depth-dependent composition of nanoparticles on planar surfaces. Herein, we combine the two techniques to investigate the nature of Cu and Au nanoparticles deposited onto ultrathin CeO_2 films on Si(111) examining their morphology and chemical composition as a function of annealing temperature for samples that have been maintained in an ultrahigh vacuum environment and exposed to air. The Cu/Au/CeO_2/Si(111) is chosen as a model system in order to provide insight into how the catalytic properties of Cu/Au/CeO_2 depend on the presence of discrete Cu and Au particles versus fully intermixed Cu/Au systems.

Keywords: alloy, catalyst, XPS, ion scattering

Introduction

There are many applications exploiting metallic nanoparticles on high surface area oxide supports including heterogeneous catalysts, photocatalysts and electrocatalysts.[1] Ceria (CeO_2) has a number of advantages as an oxide support including its ability to enhance metal dispersion; displaying a greater resistance to thermal sintering than other oxide supports and due to its ability to operate as an oxygen reservoir, thereby influencing surface chemical processes occurring on ceria-based materials.[2-4] Unlike supports such as SiO_2, when a metal atom interacts with CeO_2, charge transfer processes can occur resulting in the formation of Ce^{3+} surface species.[5, 6]

Bimetallic particles often outperform their monometallic counterparts in terms of activity and/or selectivity. For example, adding a second element can overcome the intrinsically low activity of gold. Conversely, the addition of a relatively inert element such as gold to a more reactive metal can allow the establishment of control over selectivity towards a particular catalytic route.[7] Cu/Au systems have been used for a number of applications in catalysis and electroreduction. Experimental [8] and theoretical [9, 10] studies have shown that the ordering and composition of Cu/Au nanoparticles is strongly dependent on temperature and surrounding environment. Cu/Au nanoparticles supported on CeO_2 have been used in the hydrogenation of cinnamaldehyde,[11] CO oxidation,[12-14] the oxygen-enhanced water gas shift reaction,[15] the photocatalytic oxidation of benzyl alcohol[16] and in the steam reforming of methanol.[17] Our interest in $Cu/Au/CeO_2$ stems from the development of catalysts for the “hydrogen-free” selective hydrogenation of furfural by Keane and co-workers.[18] In this catalytic system, hydrogen produced by the dehydrogenation of 2-butanol is fully utilised in the selective conversion of furfural to furfuryl alcohol. In this application, it is believed to be desirable to maintain separate Cu and Au particles on the oxide surface. However, Cu and Au have a very strong tendency to intermix forming solid solutions over the whole compositional range,[19, 20] so a motivation for the current work is to investigate the thermal behaviour of $Cu/Au/CeO_2$ model catalysts prepared by deposition of Cu and Au nanoparticles onto planar ceria surfaces.

The surface composition of bimetallic systems is commonly different to the bulk composition and depends on a number of parameters such as the relative surface energies of the two elements; atomic size; temperature and the environment to which the sample is exposed. In the phase diagram of bulk Cu/Au mixtures, only a few ordered phases are known, notably for specific Cu:Au ratios.[21, 22] For most bulk compositions, a gold-rich surface layer is favoured.[23] Nevertheless, both intermixed [24-29] and ordered surface terminations [25, 26] can be prepared when subjecting Cu/Au(111) systems to specific thermal treatments.

The technique of medium energy ion scattering (MEIS) possesses near monolayer depth resolution and has been established as a technique for the characterisation of the depth dependent composition of bimetallic layers on single crystal surfaces under the influence of adsorbates. [30, 31] A number of groups have aimed to refine the technique to investigate the depth dependent composition of nanoparticles on flat oxide surfaces.[32-35]

In this article MEIS, atomic force microscopy (AFM) and X-ray photoelectron spectroscopy (XPS) are used to characterise the temperature dependence of the composition profile of Cu/Au particles on CeO_2 thin films grown on Si(111).

Experimental Section

X-ray photoelectron spectroscopy (XPS)

XPS measurements were collected in an ultrahigh vacuum (UHV) chamber housing a Scienta ESCA-300 spectrometer equipped with a monochromatic Al *Kα* (1486.6 eV) rotating anode and an unmonochromated Al *Kα* anode (base pressure *ca.* 1×10^{-9} mbar). The detection system consisted of a large hemispherical analyser coupled to a multichannel plate/video camera (base pressure *ca.* 5×10^{-10} mbar). The instrument was calibrated daily to the Au 4f and Ag 3d photoelectron lines. The binding energy scale is referenced to the signals of Si 0/IV of Si/SiO_2 at 99.8 eV and 103.3 eV respectively. Peak fitting was carried out using CasaXPS software version 2.3.17.

Medium Energy Ion Scattering

MEIS analysis was carried out at the MEIS facility at the University of Huddersfield, UK using a beam of nominally 100 keV He^+ ions entering a UHV scattering chamber that houses a 3-axis target goniometer and a rotatable electrostatic energy analyser (base pressure *ca.* 5×10^{-10} mbar). As a sectional toroidal type, the analyser enables the simultaneous collection of a range of energies (1.5% of pass energy) and angles (27°) of backscattered ions through the use of a 2D detector located behind a set of channel plate multipliers that records both energy and angle of scattered ions. The overall 2D energy and angle spectrum is composed of individual tiles (one for each pass energy) that are linked together by software. The Si(111) sample was aligned such that the [101] direction was coincident with the ion beam incident at 35.3° off normal which leads to channelling within the Si lattice, while the centre of the analyser was aligned with the [121] direction resulting in a central backscattering angle of 125.3°. Thus, the plane of scattering contains the [121] surface direction. Energy spectra were extracted from the 2D spectrum for the three scattering angles of 119.3°, 125.3° and 131.3°. Large scattering angles were chosen to ensure maximum energy separation between the different scattered peaks in the spectra. MEIS energy spectra were analysed using the PowerMEIS simulation code discussed below.

PowerMEIS

All MEIS spectra were analysed with the PowerMEIS-3 (PM3) software. [34, 36, 37]This software uses a Monte Carlo algorithm that performs simulations of the interaction of ions (and also electrons [37]) with matter including multiple scattering (MS) and reliable scattering cross-sections. PM3 describes the sample by voxels organized in a matrix format, which may represent any complex structure consisting of a number of compounds. Here we considered different type of matrices describing discrete, alloy and core-shell spherical particles as well as thin films. In addition, each matrix has a weight to allow for a statistical mixture of structures. For enhanced computational efficiency PM3 uses a variation on the trajectory reversal approach to connect incoming and outgoing ion trajectories. These trajectories are constructed by first simulating two sets of trajectories: one set starting from the beam direction, and one set starting from the analyser. The position, energy, and path travelled by the ions during these trajectories are stored. The contribution of a specific incoming and outgoing trajectory combination from an atom A at position x,y,z is proportional to the differential elastic scattering cross section of atom A at the scattering angle between the incoming and (time-reversed) outgoing ion trajectory and the concentration of atom A at x,y,z. Simply V-shaped trajectories (straight-line in and out) can be also selected and provided the same results for the present study. The main physical inputs are the scattering cross-section, calculated from the Moliere potential, the electronic stopping power, from the SRIM 97 [38] and energy-loss straggling from the Chu model.[39] Since neutralized ions cannot be measured by our MEIS analyser, we included the neutralization correction from the Marion equation[40] in the simulations. PM3 assumes an amorphous target, i.e. the contribution from different atoms are added incoherently. Further details can be found elsewhere. [32, 41]

Atomic Force Microscopy

AFM measurements were carried out using a Bruker MultiMode 8 AFM. To minimise surface damage, all images were acquired via tapping mode using a Bruker RTESPA-300 probe (nominal frequency 300 kHz, nominal spring constant 40 N m^{-1}).

Preparation of model catalysts

Ceria films of a thickness of approx. 2 nm were prepared on Si(111) (International Wafer Service, p/B doped) by the following procedure which is based on that of Zheng *et al*. who deposited thin ceria films on nickel.[42] Cerium nitrate hexahydrate (0.43 g) was dissolved in 70 ml of ethanol with stirring, 30 ml of collodion solution (cellulose nitrate 4-8% in ethanol/diethyl ether) was then added to control the viscosity. All reagents were purchased from Sigma Aldrich and used without further treatments. This solution was then diluted by a factor of ten while maintaining the ethanol:collodion ratio. Si(111) wafers were cleaned by immersion in a basic piranha solution for 30 mins, followed by a thorough rinse with deionised water. Finally, wafers were dried in flowing N_2(g). The clean Si(111) wafers were then dipped three times (for 100 s on each occasion) into the cerium containing solution and dried for 1 hour before being calcined in air up to a temperature of 775 K at a ramp rate of 5 K min^{-1} and held at 775 K for 20 minutes.

Copper and gold were deposited in UHV via metal vapour deposition via conventional filament evaporation sources consisting of copper wire (5N purity, 0.1 mm diameter) or gold wire (5N, 0.2 mm) wound around a tantalum filament (5N, 0.25 mm). Evaporation rates were estimated as ca. 0.03 ML min^{-1} for copper and ca. 0.04 ML min^{-1} for gold, as determined via XPS from both the attenuation of the Si 2p peak and the growth of the Cu 2p/Au 4f peaks, by deposition on clean Si(111) wafers. Sample heating was carried out in UHV (base pressure *ca.* 1 × 10^{-9} mbar) with the temperature of the heating stage on which the sample was mounted monitored by a K-type thermocouple. Coverages in copper and gold are reported in monolayers (ML), where we define 1 ML as 1 × 10^{15} atoms cm^{-2}.

Results and Discussion:

Many previous studies of gold or copper nanoparticle growth have been carried out on well-defined ceria surfaces, e.g. CeO_2(111). In a MEIS experiment, when ions are backscattered from surface atoms, the peak position in the energy spectrum is governed by conservation of energy and momentum in the elastic collision. When ions are backscattered from subsurface atoms, the incident ions are subject to additional inelastic energy losses dependent on the pathlength of the ion within the sample. Consequently, a thick CeO_2 film would result in a broad Ce-related peak in the MEIS spectrum, which would swamp the signal from copper nanoparticles dispersed on the ceria surface. PowerMEIS analysis requires the fitting of the peak shapes which is facilitated by a flat background. For this reason, thin ceria films were required grown on a substrate with a low atomic mass, such as Si used in this work.

CeO_2 film on Si(111)

A representative AFM image of an ultrathin CeO_2 film grown on Si(111) is shown in Figures 1a. Disc-shaped ceria particles are observed with an average diameter of ~23 nm (range 5-50 nm). ~~The line profile in Figure 1b shows that the variation in height across the particles is in the range of 1-3 nm.~~ Figure 1~~c~~b shows the Ce 3d region of the XP spectrum of an analogous CeO_2 film on Si(111). The attenuation of the Si 2p signal as a result of ceria deposition allows an estimate of the CeO_2 film thickness. Assuming that the film is flat, the 58% attenuation of the Si 2p peak (see table 1) equates to a CeO_2 film thickness of approximately 1.8 nm. Assuming that the film adopts the fluorite structure of bulk CeO_2 (lattice parameter 0.541 nm) and that the surface terminates in {111} planes (interlayer spacing 0.313 nm), this corresponds to an average thickness of between 5 and 6 layers.

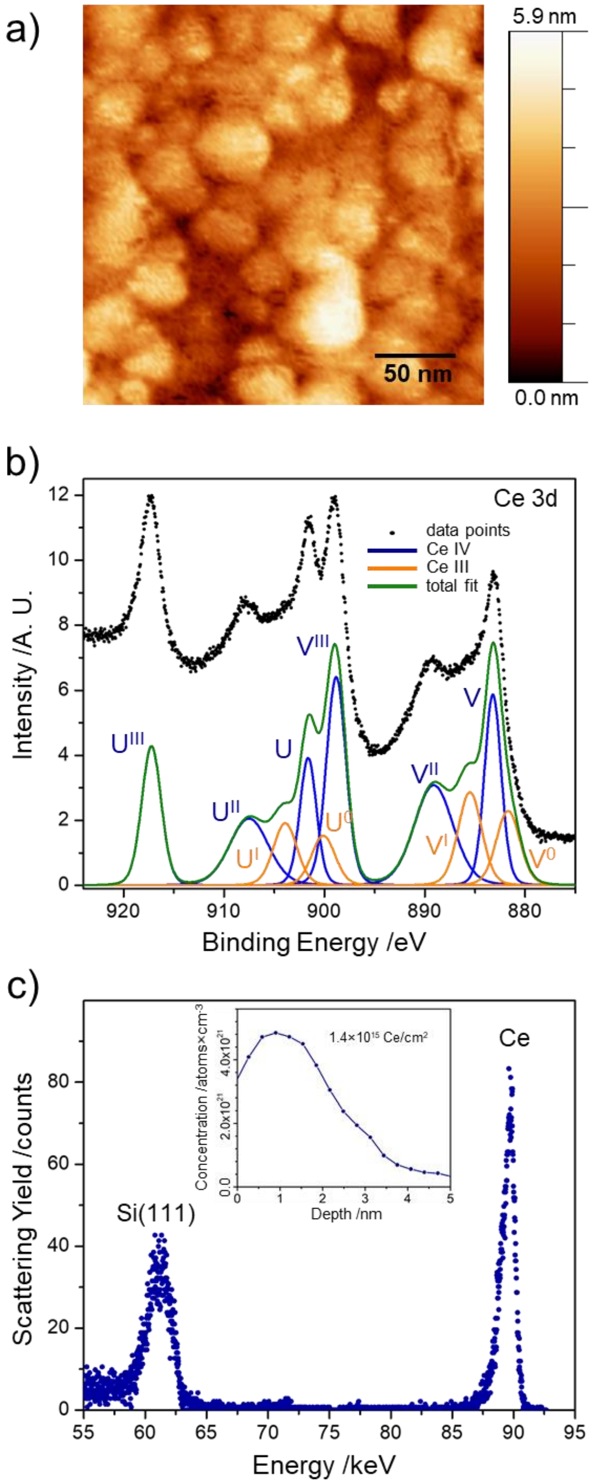

Figure 1. Characteristic AFM image of a) 255 nm × 255 nm of a CeO_2 film grown on Si(111);~~ b) line profile showing the height variation along line 1 in Figure 1b); c~~ b) XP spectrum of the Ce 3d region showing the fitting of the peaks to Ce(III) and Ce(IV) of a CeO_2 film grown on Si(111); Ce(IV) components are shown in blue, Ce(III) components are shown in orange; peaks are labelled according to the nomenclature introduced by Burroughs *et al*. [43]; ~~d~~ c) MEIS spectrum showing the intensity of scattered ions as a function of ion energy at a scattering angle of 125.3° of a CeO_2 film grown on Si(111) and in the inset the MEIS derived Ce depth profile indicating an on average 2.5 nm Ce film thickness.

Table 1. Raw XPS areas (normalised counts and %Ce(IV)) from the preparation of a ~1.6 ML Cu on ~1.0 ML Au on a CeO_2/Si(111) sample.

system	**Cu $2p_{3/2}$**	**Ce 3d**	**% Ce(IV)**	**Si 2p**	**Au 4f**
Si(111)	-	-	-	13.6	-
CeO_2/Si(111)	-	101.1	91.2	5.7	-
Au/CeO_2/Si(111)	-	91.1	88.6	5.2	8.2
Cu/Au/CeO_2/Si(111)	13.3	83.6	83.2	4.6	8.0

The Ce 3d region was fitted to quantify the relative amounts of Ce(IV) and Ce(III) oxidation states in the thin film. The as-deposited film was found to be almost exclusively constituted of Ce(IV), consistent with the formation of near-stoichiometric CeO_2 films. More details of the fitting procedure used for the Ce 3d region can be found in the Supplementary Information (SI1).

Figure 1~~d~~c shows the MEIS spectrum from a ceria film on Si(111) prepared under analogous conditions. The cerium peak at ~88 keV has a FWHM of ~1.3 keV and is well separated from the peak caused by gold nanoparticles (expected at ~91 keV). The Ce MEIS peak was converted directly into a depth profile based on well-known inelastic energy loss rates and the silicon random level reference. Shown in the inset in Fig. 1~~d~~c), it indicates a mean depth of the ceria film of ca. 2.5 nm, ~~close to the value determined by AFM,~~ and an average deposited cerium dose of 1.4×10^{15} atoms cm^{-2}.

Investigation of the effect of variable CeO_2 film thickness and morphology on MEIS spectra.

The distribution of CeO_2 grown on Si(111) was investigated by MEIS through the PM3 software. Figure 2a shows the MEIS spectrum after the deposition of 2.4 ML Cu followed by 0.54 ML Au onto a CeO_2 film on Si(111). This spectrum confirms that the cerium profile is sufficiently narrow that both copper and gold signals each appear against a flat background, which is important for the PM3 analysis of these signals presented later. Three models were used to represent the CeO_2 arrangement as can be seen in Figure 2b). According to the MEIS spectrum shown in Figure 2a, when the CeO_2 layer is simulated as a continuous thin film the experimental and simulated data show poor agreement at the cerium tail (arrow in figure 2a) and at the silicon edge (~61 keV). The cerium tail can be simulated better by adding a second layer of cerium diffusing into the silicon surface, but the silicon edge continues not to match. To improve further the agreement between experimental and simulated data, a ceria island model was used. In this case, eight steps were created with thickness for the ceria islands ranging from 0 to 3 nm. The fraction of each step of this model can be seen in Figure 2b). In each model the total atomic density (number of atoms per cm^2) was kept constant. This result is in agreement with the AFM images shown in Figure 1 (a-b). The copper and gold nanoparticles on the ceria film do not significantly affect the Ce-related signal since most of the ceria surface is not covered by them. A continuous thin film of metal would result in a shift of the cerium peak to lower energy, such a shift was not observed in the MEIS spectra. Therefore, the fit to the cerium signal was refined prior to a detailed fitting of the copper and gold peaks. In addition, consistently the inclusion of copper and gold nanoparticles on the ceria films did not significantly change its initial profile.

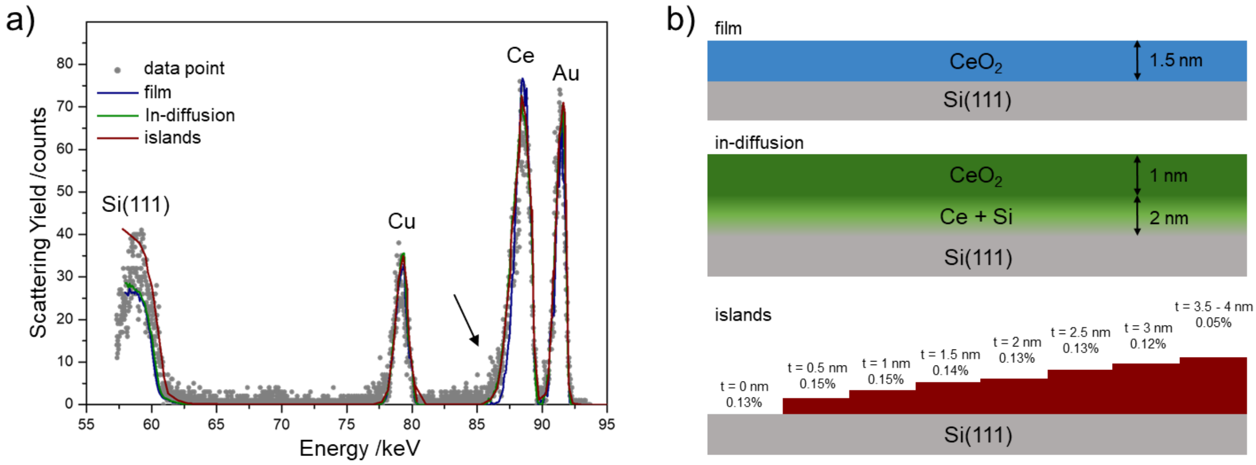

Figure 2. a) MEIS experimental data and simulations for a sample prepared by dosing copper (2.4 ML) followed by gold (0.54 ML) without thermal treatment for the three CeO_2 distribution models and for the backscattering angle of 131.3°. b) Schematic diagrams showing the three models employed for simulating the distributions of the CeO_2 layer morphology and thickness. In the first model a 1.5 nm thick CeO_2 film was used. In the second model a Ce in-diffusion layer was added. In the third model, the CeO_2 film thickness was allowed to vary between 0 and 3 nm, representing islands of CeO_2. Each model has the same number of atoms per cm^2.

The thermal behaviour of a typical CeO_2/Si(111) layer was investigated by XPS. From the analysis of the Ce 3d core level, the Ce(IV):Ce(III) was evaluated as ca. 90%:10% upon preparation. A change of the cerium oxidation state is seen with annealing, reaching a Ce(IV):Ce(III) of ca. 22%:78% after annealing to 500 K. The envelope of the O 1s peak, which contains also the signals of oxygen related to SiO_2 and the Ce-O-Si interfacial oxygen, varies accordingly. Ce 3d and O 1s core level spectra with annealing are reported in SI2.

Deposition of Au onto CeO_2/Si(111)

XPS

The metal vapour deposition of gold was carried out on a CeO_2/Si(111) sample at 300 K resulting in a gold coverage of ~1 ML. XP spectra of the Ce 3d and Au 4f regions are displayed in Figures 3a and 3b. For these XPS experiments, the non-monochromated Al *k*α source was used. The fitting of the Ce 3d region shown in figure 3a reveals that gold deposition results in a small decrease in Ce(IV):Ce(III) composition from ~91% Ce(IV) to ~89% (Table 1). This is consistent with a reduction of the ceria surface during the nucleation of gold particles. The reduction of CeO_2 by the deposition of metallic nanoparticle has been reported previously for a range of metals.[6, 44, 45] The Au $4f_{7/2}$ peak is recorded at 84.6 eV, as reported in figure 3b, a value ~~in good agreement with~~ slightly higher than that expected for metallic gold, 84.0 eV. [6, 46]

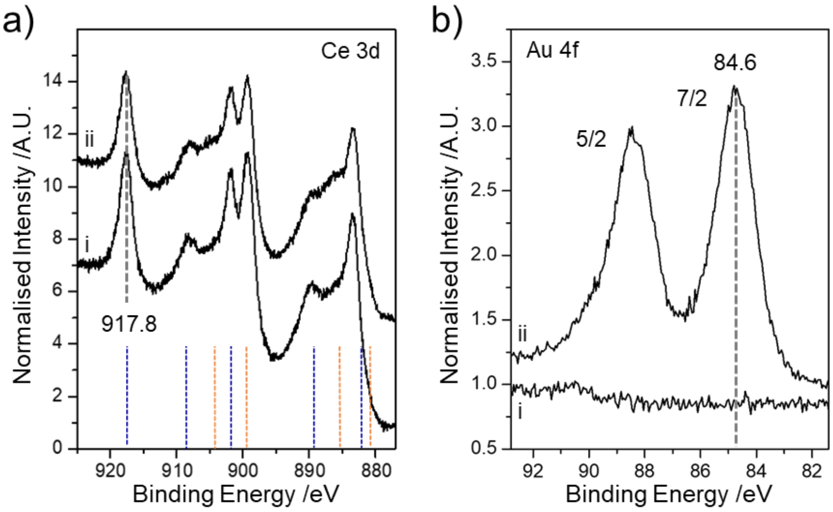

Figure 3. XP spectra displaying a) the Ce 3d region and b) the Au 4f region of the CeO_2/Si(111) surface, i) prior to and ii) after the deposition of ~1 ML Au, at a deposition temperature of 300 K; spectra are offset for clarity. In a) expected positions for Ce(IV)/Ce(III) components are indicated by blue/orange dashed lines.

Deposition of Cu onto Au/CeO_2/Si(111)

XPS:

The metal vapour deposition of copper was carried out on the Au/CeO_2/Si(111) sample at 300 K resulting in a copper coverage of ~1.6 ML. XP spectra of the Cu $2p_{3/2}$, Ce 3d and Au 4f regions before and after deposition of copper are displayed in Figures 4a-c. The Cu $2p_{3/2}$ is recorded at 933.5 eV, as shown in figure 4a; this value is in good agreement with those recorded for both metallic copper and Cu(I) [47]; moreover, no sign of asymmetries or satellite features that could suggest oxidation to Cu(II) can be seen. The Ce 3d region is reported in figure 4b. Table 1 reveals that the Ce 3d signal attenuates by ~9% after deposition of copper. In contrast, the Au 4f signal attenuates by ~2.5%. This is consistent with some copper being deposited onto gold particles, but the majority of the copper coalescing into pure nanoparticles on the ceria surface. The deposition of copper causes a further decrease in the percentage of Ce(IV) from ca. 88.6% to ca. 83.2%. This is consistent with the behaviour previously reported for the growth of copper on CeO_2 and supports the conclusion that copper particles are formed in direct contact with the ceria surface. [48] A small attenuation of the Au 4f peak indicates that some of the copper also condenses over the preformed Au nanoparticles.

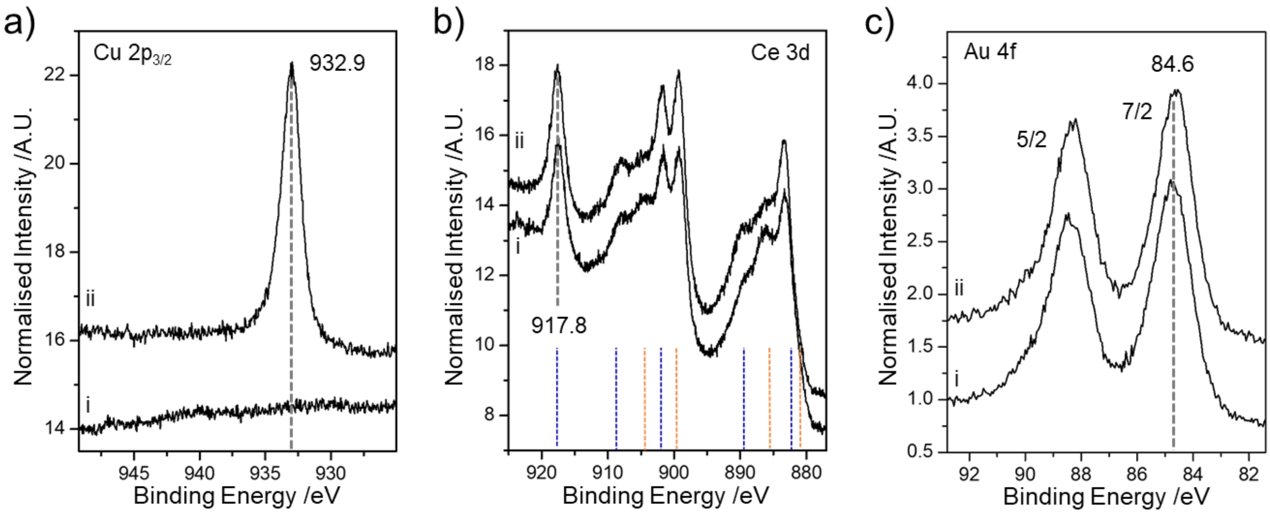

Figure 4. XP spectra of a) the Cu $2p_{3/2}$ region, b) the Ce 3d region and c) the Au 4f region, showing ~1 ML Au/CeO_2/Si(111) i) prior and ii) after deposition of ~1.6 ML Cu at 300 K. In b) expected positions for Ce(IV)/Ce(III) components are indicated by blue/orange dashed lines. Spectra are offset for clarity.

Annealing Cu/Au nanoparticle films on CeO_2/Si(111)

Figure 5 shows Cu $2p_{3/2}$, Ce 3d and Au 4f core levels XP spectra following the annealing of the layer described as above. Additional details, as well as O 1s, C 1s, Si 2p core level spectra, are reported in SI3.1.

The Cu $2p_{3/2}$ is recorded at 933.5 eV and remains essentially constant through the progressively higher annealing temperatures (Figure 5a). The fitting of the Ce 3d region in Figure 5b shows that the Ce(IV):Ce(III) ratio decreases with increasing annealing temperature. Following the highest thermal treatment, the Ce(IV):(III) ratio was found to be ~1:3. Similar behaviour is observed when annealing the CeO_2 thin film on Si(111) (See SI2). This is likely due to transfer of some oxygen from the ceria layer into the silicon substrate and/or desorption of oxygen. [49, 50] The overall intensity of the Ce 3d peaks increases with annealing temperature (Table 2 and Figure 5). Similar behaviour has been observed when annealing a ceria thin film, which was ascribed to a decrease in screening of subsurface cerium atoms when oxygen vacancies are created. [49] Contributions to the increase in the cerium signal could also derive from sintering of the metallic nanoparticles with increasing annealing temperature and from desorption of molecular adsorbates. The Au $4f_{7/2}$ peak, Figure 5c, is recorded at 84.6 eV and remains essentially constant through the annealing treatments. XPS (Table 2 and Figure 5) reveals that there is little change in the intensity of either the Cu $2p_{3/2}$ or Au 4f signals, which suggests that the particle size changes little with increasing annealing temperature.

Table 2. Raw XPS areas (normalised counts and %Ce(IV)) following the annealing of a ~1.6 ML Cu on ~1.0 ML Au on a CeO$_2$/Si(111) sample.

conditions	**Cu 2p$_{3/2}$**	**Ce 3d**	**% Ce(IV)**	**Si 2p**	**Au 4f**
As prep, RT	13.3	83.6	83.2	4.6	8.0
Anneal 325 K	12.9	90.3	84.7	4.6	8.1
Anneal 375 K	12.6	88.5	78.9	4.7	7.8
Anneal 425 K	12.5	102.2	52.3	4.5	8.0
Anneal 475 K	12.6	108.5	44.1	4.2	7.2
Anneal 510 K	13.4	110.3	39.3	3.4	8.7
Anneal 540 K	12.2	122.2	23.5	4.2	7.2

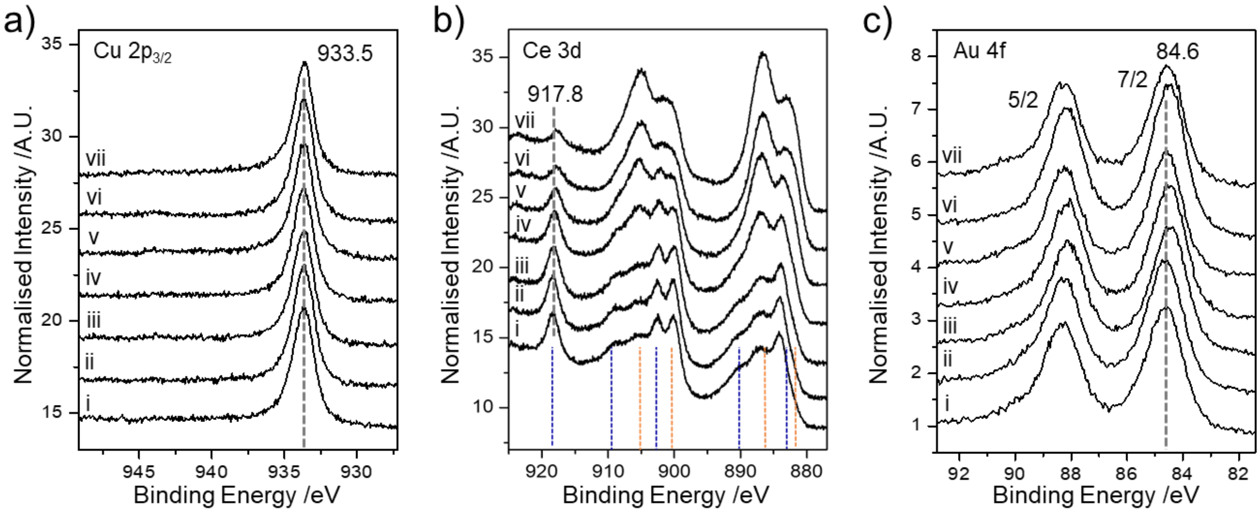

Figure 5. Annealing temperature dependence of XP spectra of the a) Cu 2p$_{3/2}$, b) Ce 3d and c) Au 4f core levels for a sample prepared by the deposition of first ~1 ML Au followed by ~1.6 ML onto a ~2 nm CeO$_2$ film on Si(111) at 300 K; i) as prepared, ii) 325 K, iii) 375 K, iv) 425 K, v) 475 K, vi) 510 K and vii) 540 K. In b) expected positions for Ce(IV)/Ce(III) components are indicated by blue/orange dashed lines. Spectra are offset for clarity.

Cu/Au/CeO$_2$/Si(111)

MEIS

The PM3 software allowed us to explore several nanoparticle structures such as discrete nanoparticles (NPs), core@shell and alloy, with spherical and hemispherical geometries. In order to evaluate the goodness of the fit for the MEIS spectra the reduced Chi-square analysis was applied.[51] The Chi-square is used as a figure-of-merit for the evaluation of goodness of fit for MEIS spectra. In this work, we used the reduced Chi-square given by Equation 1:

$$\chi^2 = \frac{1}{N}\sum_{i=1}^{N}\left\{\frac{\left[I_{exp} - I_{sim} + min\left(I_{exp},1\right)\right]^2}{I_{exp} + 1}\right\} \qquad \text{Eq. 1}$$

where N is the total number of data points, I_{exp} and I_{sim}represent the experimental and simulated spectra, respectively.[51] The min(I_{exp},1) factor is used to take into account cases of low counts. Equation 1 was applied to three ion backscattering angles (119.3°, 125.3° and 131.3°) with the same energy range for the analysis presented in this work and the mean Chi-square result was taken.

A sample was prepared by first depositing 0.14 ML Au followed by 0.6 ML Cu onto ~2 nm CeO_2/Si(111) at 300 K. MEIS data were acquired for the as-prepared sample and following annealing the same sample to 350, 425 and 525 K. The Chi-square analysis (inset in Figure 6) reveals that the best fit to the MEIS data (see S4.1) for the as-deposited sample was for discrete NPs of Cu (radius 1.5 nm) and Au (radius 2 nm) adopting a hemispherical shape. Cu nanoparticles were found to cover approximately 10% of the ceria surface, while Au particles covered approximately 2% of the surface. The fit for a core-shell morphology was only marginally less good. The possibility of a mixture of discrete particles and Au(core)@Cu(shell) particles is consistent with our XPS data following a similar sample preparation. On annealing, the particle morphology was found to be relatively stable up to ~425 K. After annealing to 525 K, the PowerMEIS Chi-square analysis now shows approximately similar values for discrete Cu and Au particles; particles with an alloy shell surrounding a Cu core and alloyed ($Au_{0.25}Cu_{0.75}$) particles. The MEIS data are consistent with a clear change occurring compared to the lower annealing temperatures and it is likely that a mixture of particle morphologies and compositions is present under these conditions caused by diffusion, agglomeration and intermixing processes at this elevated temperature. MEIS spectra and PowerMEIS fits are reported in SI4.1.

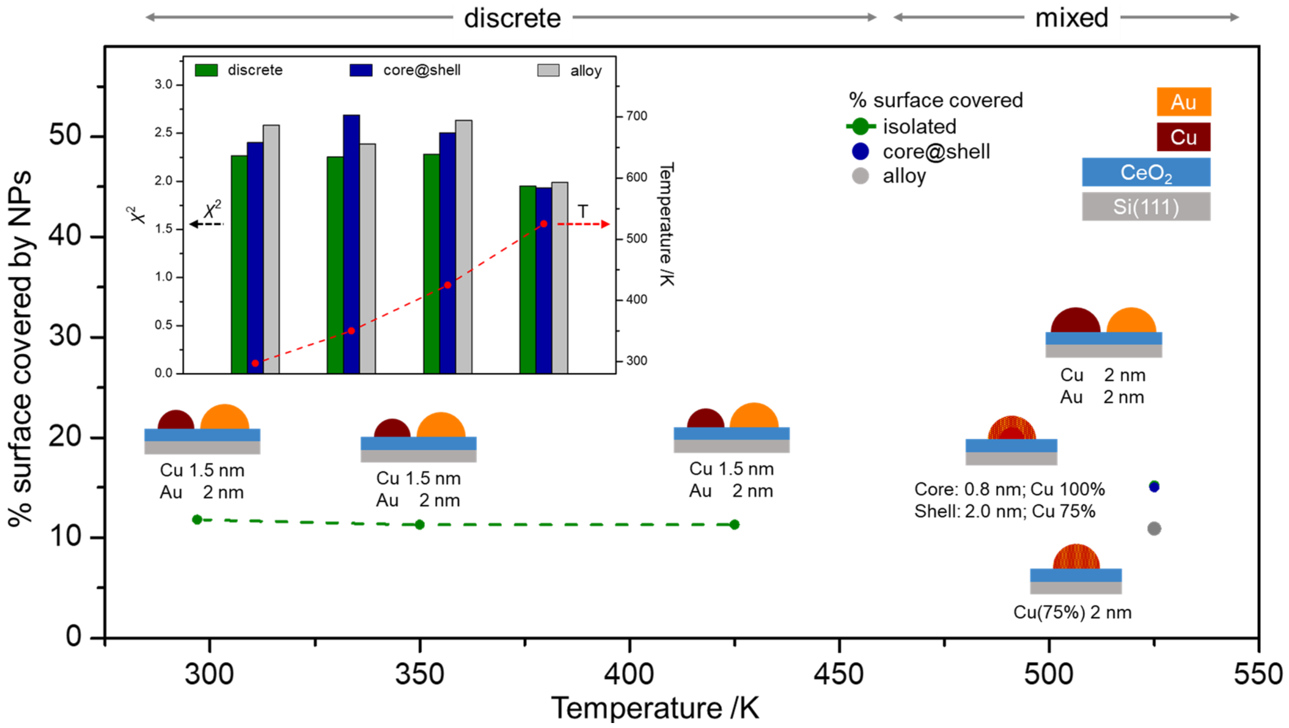

Figure 6. Nanoparticle radii, morphology and % of surface covered by nanoparticles as a function of annealing temperature for the samples prepared by the deposition of 0.14 ML Au followed by 0.6 ML Cu onto a ~2 nm CeO_2 film on Si(111) as deposited (~300 K) and annealed to 350, 425 and 525 K. In the inset, Chi-square analysis for the same samples obtained from the three ion backscattering angles (119.3°, 125.3° and 131.3°). Green, blue and grey bars indicate the use of a model with discrete NPs, core@shell and alloy, respectively.

To summarise the XPS and MEIS findings, XPS shows that when vapour depositing gold onto a CeO_2(111) film, a small charge transfer occurs on deposition, with cerium being slightly reduced and gold slightly oxidised. On addition of copper, metallic particles are nucleated, but a further reduction of ceria seems to occur. A slight decrease of the Au 4f intensity indicates that some preformed gold particles are coated by a copper layer. On annealing, the Cu $2p_{3/2}$ and Au 4f peaks stay approximately constant in both binding energy and intensity. Annealing causes an increase in the reduction of CeO_2, mimicking the behaviour observed upon annealing the CeO_2 films on Si(111). This could indicate that the metal NPs are thermally stable from the XPS point of view and there is minimal interaction with the substrate, with reduction of ceria being ascribed primarily to loss of oxygen. The MEIS analysis is consistent with the XPS results indicating isolated gold nanoparticles are formed on ceria, with subsequent growth of both isolated copper particles and copper particles on pre-formed gold particles upon deposition of copper onto Au/CeO_2/Si(111). This morphology remains stable on annealing to 425 K, though increases in particle size and alloy formation are observed following annealing to 525 K.

Influence of annealing on an air-exposed Au/Cu/CeO_2/Si(111) sample

XPS

A sample was prepared by the deposition of first ~1.5 ML copper followed by ~1.0 ML gold onto a ~1.5 nm CeO_2 film on Si(111). The sample was exposed to air before being introduced into the XPS chamber for analysis. For these XPS experiments, the monochromated Al k_α source was used. Deposition of copper on the relatively well-defined CeO_2(111) surface has been shown to be initiated at step edges.[52, 53] It has been reported that charge transfer from the oxide to copper species leads to the formation of Cu(I) [2, 45] which are thought to be located at the interface with ceria and covered by Cu(0) species.[54] Gold deposition onto Cu/CeO_2 can result in decoration of pre-existing copper particles or the formation of isolated gold particles or a combination of both effects.

Figure 7a-c show the Cu $2p_{3/2}$, Ce 3d and Au 4f regions as a function of annealing temperature. The annealing temperatures reported are, we believe, accurate to within about 25 K due to difficulties in measuring the sample temperature using this specific sample holder. After deposition of the metal nanoparticles, and subsequent exposure to air, the Cu $2p_{3/2}$ region shows a signal that can be fitted with two components (Figure 7a), one with maximum at a binding energy (BE) of 933.6 eV, attributed to copper in the I/0 oxidation state, and one at 935.5 eV, which is associated with Cu(II).[47, 55]

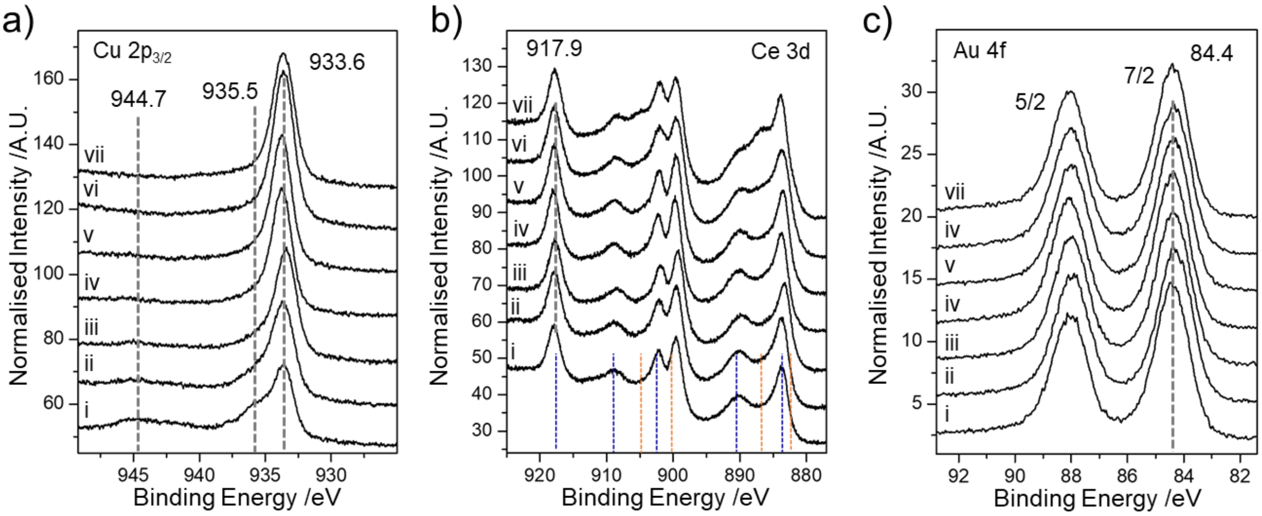

Figure 7. Annealing temperature dependence of XP spectra of the Cu $2p_{3/2}$, Ce 3d and Au 4f core levels for a sample prepared by the deposition of first ~1.5 ML Cu followed by ~1.0 ML Au onto a ~2 nm CeO_2 film on Si(111) at 300 K; i) as prepared, ii) 330 K, iii) 350 K, iv) 370 K, v) 385 K, vi) 400 K and vii) 425 K. In b) expected positions for Ce(IV)/Ce(III) components are indicated by blue/orange dashed lines. Spectra are offset for clarity.

Table 3. Raw XPS areas (normalised counts and %Ce(IV)) from a ~1.0 ML Au on ~1.5 ML Cu on CeO_2/Si(111) after exposure to air and as a function of annealing temperature

conditions	**Cu $2p_{3/2}$**	**Ce 3d**	**% Ce(IV)**	**Si 2p**	**Au 4f**
As prep, RT	60.30	191.61	89.9	19.73	37.02
Anneal 330 K	72.28	234.86	87.6	19.69	37.74
Anneal 350 K	76.47	217.84	91.0	19.27	37.59
Anneal 370 K	77.09	228.43	86.8	20.17	36.40
Anneal 385 K	84.69	269.18	84.6	19.21	36.88
Anneal 400 K	96.76	312.41	88.7	19.52	36.08
Anneal 425 K	60.30	302.89	74.8	19.73	37.02

The raised background at ca. 944 eV is attributed to the shake-up satellite features of Cu(II). A BE of 933.6 eV is approximately 1 eV higher than that typically observed for metallic copper particles.[56] Similar behaviour was reported in XP spectra of small copper particles deposited onto a single crystal ZnO surface where the authors concluded that small copper particles are partially oxidised due to the interaction with the ZnO surface.[57] With annealing to increasing temperature, the signals associated to Cu(II) decrease in intensity, the shake-up satellites attenuate and the lower BE component increases (Figure 7a). Each of these observations imply that the Cu(II) component reduces to Cu(I/0). A small shift of the lower BE peak is observed with increasing annealing temperature.

Figure 7b) shows that after preparation, the Ce 3d region shows the typical signature of cerium in the +IV oxidation state. With annealing, the decrease of the peaks related to Ce(IV) and the corresponding increase of the signals related to Ce(III) are recorded. The overall Ce(IV):Ce(III) composition % goes from ca. 90/10% after preparation to ca. 75/25% after annealing to 425 K. (see Table 3) The Au $4f_{7/2}$ is recorded at 84.4 eV, as shown in Figure 7c. The signal stays constant in position and shape throughout the annealing experiments. As observed for the main peak of copper, also the BE of Au 4f peaks are recorded at slightly higher BE than that expected for metallic gold.[6] Small gold particles have been reported to be partially oxidised on ceria surfaces, but a shift to higher binding energy has also been reported for Cu/Au alloys compared with pure gold.[58, 59]

Table 3 shows the variation of peak area for the Cu $2p_{3/2}$, Ce 3d, Si 2p, and Au 4f signals as a function of temperature obtained from the fitting procedure, and additional details are reported in SI3.2.

The Ce 3d and Cu $2p_{3/2}$ signals are seen to increase in intensity whereas that of Au 4f stays constant overall. On the basis of the XPS data, there are a number of possible interpretations of the variation in Ce 3d, Cu $2p_{3/2}$ and Au 4f intensities with increasing annealing temperature. The increase in the Ce 3d signal may indicate that the metal nanoparticles are sintering with increasing temperature, therefore exposing a larger area of bare ceria. However, one would expect a decrease in the overall intensity of the Cu $2p_{3/2}$ and Au 4f signals, which is not observed. The exposure of the sample to air causes the adsorption of carbon and oxygen containing species (e.g. OH^-, HCO_3^-, CO_3^{2-}). The thermally induced desorption of these species is likely to occur from copper and ceria sites rather than from less reactive gold sites. The deposition of copper onto ceria typically produces hemispherical copper particles.[53] As will be shown below, MEIS indicates that the copper particles have a radius of ~2.5 – 3.0 nm. Assuming a uniform array of particles on the CeO_2 surface, an array of copper particles can be envisaged whose centres are separated by between 10 and 14 nm. The subsequent deposition of gold is likely to result in gold nucleation on top of existing copper particles rather than the formation of isolated gold particles, given that Au-Cu bonds are thermodynamically more favourable than Au/ceria bonds especially when copper particles are already nucleated on the most favourable CeO_2 sites.[52, 53, 60] The relatively constant Au 4f signal as a function of increasing annealing temperature coupled with an increasing Cu $2p_{3/2}$ signal could be interpreted as being due to desorption of molecular species from bimetallic particles and intermixing of gold with copper.

MEIS: Au/Cu/CeO_2/Si(111)

Figure 8 summarizes our findings of the MEIS investigations of the samples when copper is first deposited followed by gold. MEIS spectra and PowerMEIS fits are reported in SI4.2. Figure 8 b) showing the NP's stoichiometry as a function of annealing temperature. After preparation in vacuum, PowerMEIS simulations of the data taken at 300 K indicate that the most likely nanoparticle structure corresponds to hemispherical particles of radius 2.5 nm with a Cu core of radius 1.3 nm and an alloy shell of composition 78% Cu giving an overall particle stoichiometry of ~80% Cu. After air exposure and annealing to 375 K, XPS reveals the presence of significant Cu(II) as well as C and O containing adsorbates. Under these conditions, analysis of the MEIS data reveals the formation of an exclusively Cu shell of thickness 0.6 nm surrounding a bimetallic core of radius 2.2 nm and with a Cu concentration of 45%. Segregation of Cu to the surface induced by exposure to atmospheric oxygen would be expected. PowerMEIS analysis of samples annealed to temperatures above 375 K is consistent with the formation of homogeneous alloy particles of a gradually increasing particle size an whose overall composition becomes slightly richer in gold.

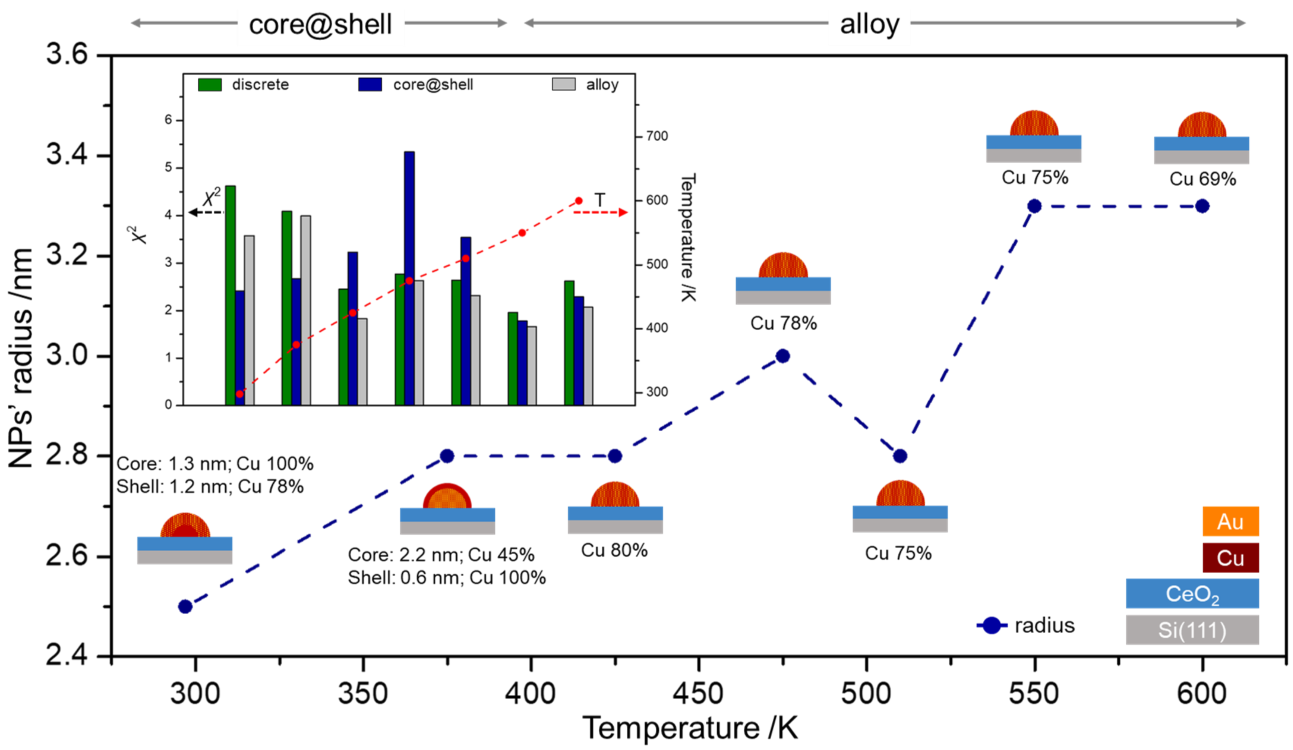

Figure 8. Nanoparticle radius, stoichiometry and morphology as a function of annealing temperature for the samples prepared by the deposition of ~1.5 ML Cu followed by ~1.0 ML Au onto a ~1.5 nm CeO_2 film on Si(111) as deposited and annealed to 375, 425, 475, 510, 550 and 600 K. Composition % is given with respect to Cu. In the inset, Chi-square analysis for the same samples obtained from the three ion backscattering angles (119.3°, 125.3° and 131.3°). Green, blue and grey bars indicate the use of a model with discrete NPs, core@shell and alloy, respectively.

Conclusions

A preparation method has been established for producing Au/Cu/CeO_2 model catalysts for analysis by MEIS consisting of a ~2 nm CeO_2 film deposited onto Si(111) followed by metal vapour deposition of elemental Cu and Au.

XPS reveals that the ceria film is initially almost pure CeO_2 in composition. On annealing a CeO_2/Si(111) sample, a gradual reduction is observed caused presumably by a combination of oxygen desorption and diffusion of oxygen into the Si substrate.

Deposition of Au onto the CeO_2/Si(111) surface at 300 K leads to a slightly lower Ce(IV):Ce(III) ratio. Deposition of Cu onto the precovered Au/CeO_2/Si(111) surface leads to further Ce(IV) reduction. In addition, a slight attenuation of the Au signal is observed. These observations are consistent with the formation of mainly pure Au and pure Cu particles with some Cu deposition onto Au particles. PowerMEIS analysis supports this conclusion, with the best fit to the MEIS data corresponding to discrete hemispherical Au (radius 2 nm) and Cu (radius 1.5 nm) particles. These particles are relatively thermally stable up to at least 450 K. The most physically realistic model for the sample after annealing to 525 K involves the formation of hemispherical alloyed CuAu particles (radius 2 nm).

A sample prepared by deposition of Cu followed by Au onto CeO_2/Si(111) was exposed to air. XPS revealed the presence of Cu(II) species following air exposure which are reduced to Cu/Cu(I) with increasing annealing temperature. Annealing to 375 K caused desorption of weakly bound adsorbates and MEIS revealed that under these conditions the sample consisted of nanoparticles with a Au rich core and a Cu rich shell. Annealing to higher temperatures resulted in the formation of alloyed particles. MEIS revealed that initially core-shell particles were produced after deposition of Cu followed by Au in vacuum. On exposure to air, Cu segregation to the surface was observed. Annealing to higher temperatures produced MEIS data that were consistent with the formation of homogeneously alloyed particles.

The powerful combination of XPS and MEIS allows significant insight into the thermal behaviour of Cu and Au particles on the ceria surface providing information on alloying behaviour, particle size and the electronic interaction with the CeO_2 support material. In fact, this work suggests that discrete Cu and Au particles are stable up to 450 K on the CeO_2 surface. When preparing Cu/Au/CeO_2 catalysts for selective hydrogenation of furfural, as discrete metal particles are desirable, the thermal treatment of the catalyst should be considered carefully in order to minimise alloy formation.

Acknowledgements

RM and FG acknowledge funding from EPSRC grants (RM: EP/506631/1; FG: EP/M029077/1). JAvdB and AR acknowledge the EPSRC funding for the use of the MEIS facility at the University of Huddersfield within grant EP/M029077/1. This study was financed in part by the Coordenação de Aperfeiçoamento de Pessoal de Nível Superior - Brasil (CAPES) - Finance Code 001, by Conselho Nacional de Desenvolvimento Científico e Tecnológico (CNPq), and PRONEX-FAPERGS 16/2551-0000479-0.

The research data supporting this publication can be accessed at http://dx.doi.org/10.17630/c6bcbb11-ffd3-497c-bd12-7e09bdcc31d9 to be ~~added~~ activated upon acceptance.

Supporting material description: fitting of Ce 3d XPS region; XPS of CeO_2/Si(111) with annealing; XPS of (Cu+Au)/CeO_2/Si(111) with annealing; MEIS spectra and respective PowerMEIS fits of (Cu+Au)/CeO_2/Si(111) with annealing

References

[1] A. T. Bell, The impact of nanoscience on heterogeneous catalysis, Science, 299 (2003) 1688-1691.

[2] M. M. Branda, N. C. Hernandez, J. F. Sanz, F. Illas, Density Functional Theory Study of the Interaction of Cu, Ag, and Au Atoms with the Regular CeO_2 (111) Surface, Journal of Physical Chemistry C, 114 (2010) 1934-1941.

[3] A. Trovarelli, Catalytic properties of ceria and CeO_2-containing materials, Catal. Rev.-Sci. Eng., 38 (1996) 439-520.

[4] J. Kaspar, P. Fornasiero, M. Graziani, Use of CeO_2-based oxides in the three-way catalysis, Catalysis Today, 50 (1999) 285-298.

[5] L. J. Chen, Y. H. Tang, L. X. Cui, C. Y. Ouyang, S. Q. Shi, Charge transfer and formation of Ce^{3+} upon adsorption of metal atom M (M = Cu, Ag, Au) on CeO_2 (100) surface, Journal of Power Sources, 234 (2013) 69-81.

[6] M. Baron, O. Bondarchuk, D. Stacchiola, S. Shaikhutdinov, H. J. Freund, Interaction of Gold with Cerium Oxide Supports: CeO_2(111) Thin Films vs CeO_x Nanoparticles, Journal of Physical Chemistry C, 113 (2009) 6042-6049.

[7] F. Tao, S. R. Zhang, L. Nguyen, X. Q. Zhang, Action of bimetallic nanocatalysts under reaction conditions and during catalysis: evolution of chemistry from high vacuum conditions to reaction conditions, Chemical Society Reviews, 41 (2012) 7980-7993.

[8] E. Völker, F. J. Williams, E. J. Calvo, T. Jacob, D. J. Schiffrin, O2 induced Cu surface segregation in Au–Cu alloys studied by angle resolved XPS and DFT modelling, Physical Chemistry Chemical Physics, 14 (2012) 7448-7455.

[9] N. Artrith, A. M. Kolpak, Grand canonical molecular dynamics simulations of Cu-Au nanoalloys in thermal equilibrium using reactive ANN potentials, Computational Materials Science, 110 (2015) 20-28.

[10] N. Artrith, A. M. Kolpak, Understanding the Composition and Activity of Electrocatalytic Nanoalloys in Aqueous Solvents: A Combination of DFT and Accurate Neural Network Potentials, Nano Letters, 14 (2014) 2670-2676.

[11] X. M. Liao, V. Pitchon, P. H. Cuong, W. Chu, V. Caps, Hydrogenation of cinnamaldehyde over bimetallic Au-Cu/CeO_2 catalyst under a mild condition, Chinese Chemical Letters, 28 (2017) 293-296.

[12] X. M. Liao, W. Chu, X. Y. Dai, V. Pitchon, Bimetallic Au-Cu supported on ceria for PROX reaction: Effects of Cu/Au atomic ratios and thermal pretreatments, Applied Catalysis B-Environmental, 142 (2013) 25-37.

[13] R. Fiorenza, C. Crisafulli, G. G. Condorelli, F. Lupo, S. Scire, Au-Ag/CeO_2 and Au-Cu/CeO_2 Catalysts for Volatile Organic Compounds Oxidation and CO Preferential Oxidation, Catalysis Letters, 145 (2015) 1691-1702.

[14] L. Zhang, H. Y. Kim, G. Henkelman, CO Oxidation at the Au-Cu Interface of Bimetallic Nanoclusters Supported on CeO_2(111), Journal of Physical Chemistry Letters, 4 (2013) 2943-2947.

[15] N. K. Gamboa-Rosales, J. L. Ayastuy, M. P. Gonzalez-Marcos, M. A. Gutierrez-Ortiz, Oxygen-enhanced water gas shift over ceria-supported Au-Cu bimetallic catalysts prepared by wet impregnation and deposition-precipitation, International Journal of Hydrogen Energy, 37 (2012) 7005-7016.

[16] B. B. Chen, X. M. Li, R. J. Zheng, R. P. Chen, X. Sun, Bimetallic (Au-Cu core)@(ceria shell) nanotubes for photocatalytic oxidation of benzyl alcohol: improved reactivity by Cu, Journal of Materials Chemistry A, 5 (2017) 13382-13391.

[17] C. Pojanavaraphan, A. Luengnaruemitchai, E. Gulari, Catalytic activity of Au-Cu/CeO_2-ZrO_2 catalysts in steam reforming of methanol, Applied Catalysis a-General, 456 (2013) 135-143.

[18] C. Pischetola, L. Collado, M. A. Keane, F. Cardenas-Lizana, Gas Phase Hydrogenation of Furaldehydes via Coupling with Alcohol Dehydrogenation over Ceria Supported Au-Cu, Molecules, 23 (2018).

[19] R. F. Zhang, X. F. Kong, H. T. Wang, S. H. Zhang, D. Legut, S. H. Sheng, S. Srinivasan, K. Rajan, T. C. Germann, An informatics guided classification of miscible and immiscible binary alloy systems, Scientific Reports, 7 (2017) 9577.

[20] W. B. Pearson, Handbook of Lattice Spacings and Structures of Metals and Alloys (Pergamon, London, 1958).

[21] J. Hennig, D. Mari, R. Schaller, Order-disorder phase transition and stress-induced diffusion in Au-Cu, Physical Review B, 79 (2009) 144116.

[22] Y. Feutelais, B. Legendre, M. Guymont, New enthalpies determination and in situ X-ray diffraction observations of order/disorder transitions in $Au_{0.5}Cu_{0.5}$, Acta Materialia, 47 (1999) 2539-2551.

[23] X. Zhao, P. Liu, J. Hrbek, J.A. Rodriguez, M. Pérez, The chemisorption of SO_2 on the Cu/Au(111) surface: Interplay between ensemble and electronic effects, Surface Science, 592 (2005) 25-36.

[24] L. Wang, P. Li, H. Shi, Z. Li, K. Wu, X. Shao, Thickness-Dependent Adsorption of Melamine on Cu/Au(111) Films, The Journal of Physical Chemistry C, 121 (2017) 7977-7984.

[25] F. Grillo, R. Megginson, D. Batchelor, M. Muntwiler, C. J. Baddeley, Structural and electronic characterization of Cu/Au(111) near-surface alloys, Japanese Journal of Applied Physics, 58 (2019) 5.

[26] F. Grillo, R. Megginson, J. Christie, S. M. Francis, N. V. Richardson, C. J. Baddeley, Structure and Reactivity of Cu-doped Au(111) Surfaces, e-Journal of Surface Science and Nanotechnology, 16 (2018) 163-171.

[27] F. Grillo, H. Früchtl, S. M. Francis, N. V. Richardson, Site selectivity in the growth of copper islands on Au (111), New Journal of Physics, 13 (2011).

[28] Q. Liu, Y. Ning, W. Huang, Q. Fu, F. Yang, X. Bao, Origin of the Thickness-Dependent Oxidation of Ultrathin Cu Films on Au(111), The Journal of Physical Chemistry C, 122 (2018) 8364-8372.

[29] W. Wang, H. Shi, L. Wang, Z. Li, H. Shi, K. Wu, X. Shao, Comparison Study of Structural Properties and CO Adsorption on the Cu/Au(111) and Au/Cu(111) Thin Films, The Journal of Physical Chemistry C, 122 (2018) 19551-19559.

[30] S. Deckers, F. Habraken, W. F. Vanderweg, A. W. D. Vandergon, J. F. Vanderveen, J. W. Geus, Oxidation-induced segregation at the $Pt0_{.5}Ni_{0.5}(111)$ surface studied by medium energy ion scattering, G, Applied Surface Science, 45 (1990) 121-129.

[31] C. J. Baddeley, L. H. Bloxham, S. C. Laroze, R. Raval, T. C. Q. Noakes, P. Bailey, Quantitative analysis of adsorbate induced segregation at bimetallic surfaces: Improving the accuracy of medium energy ion scattering results, Journal of Physical Chemistry B, 105 (2001) 2766-2772.

[32] V. Z. C. Paes, M. V. Castegnaro, D. L. Baptista, P. L. Grande, J. Morais, Unveiling the Inner Structure of PtPd Nanoparticles, Journal of Physical Chemistry C, 121 (2017) 19461-19466.

[33] D. F. Sanchez, R. Moiraghi, F. P. Cometto, M. A. Perez, P. F. P. Fichtner, P. L. Grande, Morphological and compositional characteristics of bimetallic core@shell nanoparticles revealed by MEIS, Applied Surface Science, 330 (2015) 164-171.

[34] M. A. Sortica, P. L. Grande, G. Machado, L. Miotti, Characterization of nanoparticles through medium-energy ion scattering, Journal of Applied Physics, 106 (2009).

[35] J. Gustafson, A. R. Haire, C. J. Baddeley, Depth-profiling the composition of bimetallic nanoparticles using medium energy ion scattering, Surface Science, 605 (2011) 220-224.

[36] G. G. Marmitt, PowerMEIS-3 simulation code, http://tars.if.ufrgs.br/.

[37] G. G. Marmitt, Metal oxides of resistive memories investigated by electron and ion backscattering, Ph.D. thesis, Universidade Federal do Rio Grande do Sul, Porto Alegre (2017), https://lume.ufrgs.br/handle/10183/170451.

[38] J. F. Ziegler, J. P. Biersack, U. Littmark, The Stopping and Range of Ions in Solids, vol. 1 of The Stopping and Ranges of Ions in Matter: Stopping tables SRIM 97 (Pergamon Press, New York, 1985).

[39] W. K. Chu, Calculation of energy straggling for protons and helium ions, Physical Review A, 13 (1976) 2057-2060.

[40] J. B. Marion, F. C. Young, Nuclear Reaction Analysis, Graphs and Tables (North Holland Publishing Company, Amsterdam, 1968).

[41] H. Trombini, G. G. Marmitt, I. Alencar, D. L. Baptista, S. Reboh, F. Mazen, R. B. Pinheiro, D. F. Sanchez, C. A. Senna, B. S. Archanjo, C. A. Achete, P. L. Grande, Unraveling structural and compositional information in 3D FinFET electronic devices, Scientific Reports, 9 (2019).

[42] X. C. Zheng, X. L. Zhang, Z. Y. Fang, X. Y. Wang, S. R. Wang, S. H. Wu, Characterization and catalysis studies of CuO/CeO_2 model catalysts, Catalysis Communications, 7 (2006) 701-704.

[43] P. Burroughs, A. Hamnett, A. F. Orchard, G. Thornton, Satellite structure in the X-ray photoelectron spectra of some binary and mixed oxides of lanthanum and cerium, Journal of the Chemical Society, Dalton Transactions, (1976) 1686-1698.

[44] J. L. Lu, H. J. Gao, S. Shaikhutdinov, H. J. Freund, Gold supported on well-ordered ceria films: nucleation, growth and morphology in CO oxidation reaction, Catalysis Letters, 114 (2007) 8-16.

[45] Y. H. Tang, H. Zhang, L. X. Cui, C. Y. Ouyang, S. Q. Shi, W .H. Tang, H. Li, L. Q. Chen, Electronic states of metal (Cu, Ag, Au) atom on CeO_2(111) surface: The role of local structural distortion, Journal of Power Sources, 197 (2012) 28-37.

[46] N. C. Hernández, R. Grau-Crespo, N. H. de Leeuw, J. F. Sanz, Electronic charge transfer between ceria surfaces and gold adatoms: a GGA+U investigation, Physical Chemistry Chemical Physics, 11 (2009) 5246-5252.

[47] M. C. Biesinger, Advanced analysis of copper X-ray photoelectron spectra, Surf. Interface Anal., 49 (2017) 1325-1334.

[48] G. H. Li, S. W. Hu, Q. Xu, J. F. Zhu, Interaction between Cu Nanoparticles and CeO_2(111) Film Surfaces, Journal of Physical Chemistry C, 123 (2019) 23563-23571.

[49] P. Sapkota, A. Aprahamian, K. Y. Chan, B. Frentz, K. T. Macon, S. Ptasinska, D. Robertson, K. Manukyan, Irradiation-induced reactions at the $CeO_2/SiO_2/Si$ interface, The Journal of Chemical Physics, 152 (2020) 104704.

[50] M. Vorokhta, I. Matolinova, M. Dubau, S. Haviar, I. Khalakhan, K. Sevcikova, T. Mori, H. Yoshikawa, V. Matolin, HAXPES study of CeOx thin film-silicon oxide interface, Applied Surface Science, 303 (2014) 46-53.

[51] K. J. Mighell, Parameter estimation in astronomy with Poisson-distributed data. I. The χ_γ^2 statistic, Astrophys. J., 518 (1999) 380-393.

[52] T. E. James, S. L. Hemmingson, C. T. Campbell, Energy of Supported Metal Catalysts: From Single Atoms to Large Metal Nanoparticles, ACS Catalysis, 5 (2015) 5673-5678.

[53] T. E. James, S. L. Hemmingson, T. Ito, C. T. Campbell, Energetics of Cu Adsorption and Adhesion onto Reduced CeO_2(111) Surfaces by Calorimetry, The Journal of Physical Chemistry C, 119 (2015) 17209-17217.

[54] L. Szabova, T. Skala, I. Matolinova, S. Fabris, M. F. Camellone, V. Matolin, Copper-ceria interaction: A combined photoemission and DFT study, Applied Surface Science, 267 (2013) 12-16.

[55] D. Tahir, S. Tougaard, Electronic and optical properties of Cu, CuO and Cu_2O studied by electron spectroscopy, Journal of Physics-Condensed Matter, 24 (2012).

[56] Y. T. Wu, E. Garfunkel, T. E. Madey, Initial stages of Cu growth on ordered Al_2O_3 ultrathin films, Journal of Vacuum Science & Technology a-Vacuum Surfaces and Films, 14 (1996) 1662-1667.

[57] M. C. Patterson, X. Nie, F. Wang, R. L. Kurtz, S. B. Sinnott, A. Asthagiri, P. T. Sprunger, Growth and Structure of Cu and Au on the Nonpolar ZnO($10\overline{1}0$) Surface: STM, XPS, and DFT Studies, The Journal of Physical Chemistry C, 117 (2013) 18386-18397.

[58] T .K. Sham, A. Hiraya, M. Watanabe, Electronic structure of Cu-Au alloys from the Cu perspective: A Cu $L_{3,2}$-edge study, Physical Review B, 55 (1997) 7585-7592.

[59] M. Kuhn, T. K. Sham, Charge redistribution and electronic behavior in a series of Au-Cu alloys, Physical Review B, 49 (1994) 1647-1661.

[60] S. L. Hemmingson, C. T. Campbell, Trends in Adhesion Energies of Metal Nanoparticles on Oxide Surfaces: Understanding Support Effects in Catalysis and Nanotechnology, ACS Nano, 11 (2017) 1196-1203.

Thermal behaviour of Cu and Au nanoparticles grown on CeO_2 thin films

R. Megginson[1], F. Grillo[1], S. M. Francis[1], V. Z. C. Paes[2], H. Trombini[2], P. L. Grande[2], A. K. Rossall[3], J. A. van den Berg[3], C. J. Baddeley[1]*

1. EaStCHEM School of Chemistry, University of St Andrews, North Haugh, St Andrews, Fife, KY16 9ST, United Kingdom
2. Laboratório de Implantação Iônica, Universidade Federal do Rio Grande Sul UFRGS, Instituto de Física, Av. Bento Goncalves 9500, BR-91501970 Porto Alegre, RS, Brazil
3. MEIS Facility - Ion Beam Centre; School of Computing and Engineering, University of Huddersfield, Huddersfield, HD1 3DH, United Kingdom

* email cjb14@st-andrews.ac.uk

Abstract:

Bimetallic catalysts are often more active and/or selective than their monometallic counterparts. The behaviour of such catalysts is frequently strongly dependent on the molar ratio of the two elements as well as nanoparticle size and the interaction with the support material. X-ray photoelectron spectroscopy (XPS) is an excellent surface analytical technique for probing the electronic properties of catalytic systems. When a mixture of pure and alloyed particles is present, it is more difficult to extract information from XPS given that it is a spatial averaging technique. Recently, the technique of medium energy ion scattering (MEIS) has been exploited to investigate the depth-dependent composition of nanoparticles on planar surfaces. Herein, we combine the two techniques to investigate the nature of Cu and Au nanoparticles deposited onto ultrathin CeO_2 films on Si(111) examining their morphology and chemical composition as a function of annealing temperature for samples that have been maintained in an ultrahigh vacuum environment and exposed to air. The Cu/Au/CeO_2/Si(111) is chosen as a model system in order to provide insight into how the catalytic properties of Cu/Au/CeO_2 depend on the presence of discrete Cu and Au particles versus fully intermixed Cu/Au systems.

Keywords: alloy, catalyst, XPS, ion scattering

Introduction

There are many applications exploiting metallic nanoparticles on high surface area oxide supports including heterogeneous catalysts, photocatalysts and electrocatalysts.[1] Ceria (CeO_2) has a number of advantages as an oxide support including its ability to enhance metal dispersion; displaying a greater resistance to thermal sintering than other oxide supports and due to its ability to operate as an oxygen reservoir, thereby influencing surface chemical processes occurring on ceria-based materials.[2-4] Unlike supports such as SiO_2, when a metal atom interacts with CeO_2, charge transfer processes can occur resulting in the formation of Ce^{3+} surface species.[5, 6]

Bimetallic particles often outperform their monometallic counterparts in terms of activity and/or selectivity. For example, adding a second element can overcome the intrinsically low activity of gold. Conversely, the addition of a relatively inert element such as gold to a more reactive metal can allow the establishment of control over selectivity towards a particular catalytic route.[7] Cu/Au systems have been used for a number of applications in catalysis and electroreduction. Experimental [8] and theoretical [9, 10] studies have shown that the ordering and composition of Cu/Au nanoparticles is strongly dependent on temperature and surrounding environment. Cu/Au nanoparticles supported on CeO_2 have been used in the hydrogenation of cinnamaldehyde,[11] CO oxidation,[12-14] the oxygen-enhanced water gas shift reaction,[15] the photocatalytic oxidation of benzyl alcohol[16] and in the steam reforming of methanol.[17] Our interest in Cu/Au/CeO_2 stems from the development of catalysts for the “hydrogen-free” selective hydrogenation of furfural by Keane and co-workers.[18] In this catalytic system, hydrogen produced by the dehydrogenation of 2-butanol is fully utilised in the selective conversion of furfural to furfuryl alcohol. In this application, it is believed to be desirable to maintain separate Cu and Au particles on the oxide surface. However, Cu and Au have a very strong tendency to intermix forming solid solutions over the whole compositional range,[19, 20] so a motivation for the current work is to investigate the thermal behaviour of Cu/Au/CeO_2 model catalysts prepared by deposition of Cu and Au nanoparticles onto planar ceria surfaces.

The surface composition of bimetallic systems is commonly different to the bulk composition and depends on a number of parameters such as the relative surface energies of the two elements; atomic size; temperature and the environment to which the sample is exposed. In the phase diagram of bulk Cu/Au mixtures, only a few ordered phases are known, notably for specific Cu:Au ratios.[21, 22] For most bulk compositions, a gold-rich surface layer is favoured.[23] Nevertheless, both intermixed [24-29] and ordered surface terminations [25, 26] can be prepared when subjecting Cu/Au(111) systems to specific thermal treatments.

The technique of medium energy ion scattering (MEIS) possesses near monolayer depth resolution and has been established as a technique for the characterisation of the depth dependent composition of bimetallic layers on single crystal surfaces under the influence of adsorbates. [30, 31] A number of groups have aimed to refine the technique to investigate the depth dependent composition of nanoparticles on flat oxide surfaces.[32-35]

In this article MEIS, atomic force microscopy (AFM) and X-ray photoelectron spectroscopy (XPS) are used to characterise the temperature dependence of the composition profile of Cu/Au particles on CeO_2 thin films grown on Si(111).

Experimental Section

X-ray photoelectron spectroscopy (XPS)

XPS measurements were collected in an ultrahigh vacuum (UHV) chamber housing a Scienta ESCA-300 spectrometer equipped with a monochromatic Al *Kα* (1486.6 eV) rotating anode and an unmonochromated Al *Kα* anode (base pressure *ca.* 1×10^{-9} mbar). The detection system consisted of a large hemispherical analyser coupled to a multichannel plate/video camera (base pressure *ca.* 5×10^{-10} mbar). The instrument was calibrated daily to the Au 4f and Ag 3d photoelectron lines. The binding energy scale is referenced to the signals of Si 0/IV of Si/SiO_2 at 99.8 eV and 103.3 eV respectively. Peak fitting was carried out using CasaXPS software version 2.3.17.

Medium Energy Ion Scattering

MEIS analysis was carried out at the MEIS facility at the University of Huddersfield, UK using a beam of nominally 100 keV He^+ ions entering a UHV scattering chamber that houses a 3-axis target goniometer and a rotatable electrostatic energy analyser (base pressure *ca.* 5×10^{-10} mbar). As a sectional toroidal type, the analyser enables the simultaneous collection of a range of energies (1.5% of pass energy) and angles (27°) of backscattered ions through the use of a 2D detector located behind a set of channel plate multipliers that records both energy and angle of scattered ions. The overall 2D energy and angle spectrum is composed of individual tiles (one for each pass energy) that are linked together by software. The Si(111) sample was aligned such that the [101] direction was coincident with the ion beam incident at 35.3° off normal which leads to channelling within the Si lattice, while the centre of the analyser was aligned with the [121] direction resulting in a central backscattering angle of 125.3°. Thus, the plane of scattering contains the [121] surface direction. Energy spectra were extracted from the 2D spectrum for the three scattering angles of 119.3°, 125.3° and 131.3°. Large scattering angles were chosen to ensure maximum energy separation between the different scattered peaks in the spectra. MEIS energy spectra were analysed using the PowerMEIS simulation code discussed below.

PowerMEIS

All MEIS spectra were analysed with the PowerMEIS-3 (PM3) software. [34, 36, 37]This software uses a Monte Carlo algorithm that performs simulations of the interaction of ions (and also electrons [37]) with matter including multiple scattering (MS) and reliable scattering cross-sections. PM3 describes the sample by voxels organized in a matrix format, which may represent any complex structure consisting of a number of compounds. Here we considered different type of matrices describing discrete, alloy and core-shell spherical particles as well as thin films. In addition, each matrix has a weight to allow for a statistical mixture of structures. For enhanced computational efficiency PM3 uses a variation on the trajectory reversal approach to connect incoming and outgoing ion trajectories. These trajectories are constructed by first simulating two sets of trajectories: one set starting from the beam direction, and one set starting from the analyser. The position, energy, and path travelled by the ions during these trajectories are stored. The contribution of a specific incoming and outgoing trajectory combination from an atom A at position x,y,z is proportional to the differential elastic scattering cross section of atom A at the scattering angle between the incoming and (time-reversed) outgoing ion trajectory and the concentration of atom A at x,y,z. Simply V-shaped trajectories (straight-line in and out) can be also selected and provided the same results for the present study. The main physical inputs are the scattering cross-section, calculated from the Moliere potential, the electronic stopping power, from the SRIM 97 [38] and energy-loss straggling from the Chu model.[39] Since neutralized ions cannot be measured by our MEIS analyser, we included the neutralization correction from the Marion equation[40] in the simulations. PM3 assumes an amorphous target, i.e. the contribution from different atoms are added incoherently. Further details can be found elsewhere. [32, 41]

Atomic Force Microscopy

AFM measurements were carried out using a Bruker MultiMode 8 AFM. To minimise surface damage, all images were acquired via tapping mode using a Bruker RTESPA-300 probe (nominal frequency 300 kHz, nominal spring constant 40 N m^{-1}).

Preparation of model catalysts

Ceria films of a thickness of approx. 2 nm were prepared on Si(111) (International Wafer Service, p/B doped) by the following procedure which is based on that of Zheng *et al*. who deposited thin ceria films on nickel.[42] Cerium nitrate hexahydrate (0.43 g) was dissolved in 70 ml of ethanol with stirring, 30 ml of collodion solution (cellulose nitrate 4-8% in ethanol/diethyl ether) was then added to control the viscosity. All reagents were purchased from Sigma Aldrich and used without further treatments. This solution was then diluted by a factor of ten while maintaining the ethanol:collodion ratio. Si(111) wafers were cleaned by immersion in a basic piranha solution for 30 mins, followed by a thorough rinse with deionised water. Finally, wafers were dried in flowing N_2(g). The clean Si(111) wafers were then dipped three times (for 100 s on each occasion) into the cerium containing solution and dried for 1 hour before being calcined in air up to a temperature of 775 K at a ramp rate of 5 K min^{-1} and held at 775 K for 20 minutes.

Copper and gold were deposited in UHV via metal vapour deposition via conventional filament evaporation sources consisting of copper wire (5N purity, 0.1 mm diameter) or gold wire (5N, 0.2 mm) wound around a tantalum filament (5N, 0.25 mm). Evaporation rates were estimated as ca. 0.03 ML min^{-1} for copper and ca. 0.04 ML min^{-1} for gold, as determined via XPS from both the attenuation of the Si 2p peak and the growth of the Cu 2p/Au 4f peaks, by deposition on clean Si(111) wafers. Sample heating was carried out in UHV (base pressure *ca.* 1 × 10^{-9} mbar) with the temperature of the heating stage on which the sample was mounted monitored by a K-type thermocouple. Coverages in copper and gold are reported in monolayers (ML), where we define 1 ML as 1 × 10^{15} atoms cm^{-2}.

Results and Discussion:

Many previous studies of gold or copper nanoparticle growth have been carried out on well-defined ceria surfaces, e.g. CeO_2(111). In a MEIS experiment, when ions are backscattered from surface atoms, the peak position in the energy spectrum is governed by conservation of energy and momentum in the elastic collision. When ions are backscattered from subsurface atoms, the incident ions are subject to additional inelastic energy losses dependent on the pathlength of the ion within the sample. Consequently, a thick CeO_2 film would result in a broad Ce-related peak in the MEIS spectrum, which would swamp the signal from copper nanoparticles dispersed on the ceria surface. PowerMEIS analysis requires the fitting of the peak shapes which is facilitated by a flat background. For this reason, thin ceria films were required grown on a substrate with a low atomic mass, such as Si used in this work.

<u>CeO_2 film on Si(111)</u>

A representative AFM image of an ultrathin CeO_2 film grown on Si(111) is shown in Figures 1a. Disc-shaped ceria particles are observed with an average diameter of ~23 nm (range 5-50 nm). Figure 1b shows the Ce 3d region of the XP spectrum of an analogous CeO_2 film on Si(111). The attenuation of the Si 2p signal as a result of ceria deposition allows an estimate of the CeO_2 film thickness. Assuming that the film is flat, the 58% attenuation of the Si 2p peak (see table 1) equates to a CeO_2 film thickness of approximately 1.8 nm. Assuming that the film adopts the fluorite structure of bulk CeO_2 (lattice parameter 0.541 nm) and that the surface terminates in {111} planes (interlayer spacing 0.313 nm), this corresponds to an average thickness of between 5 and 6 layers.

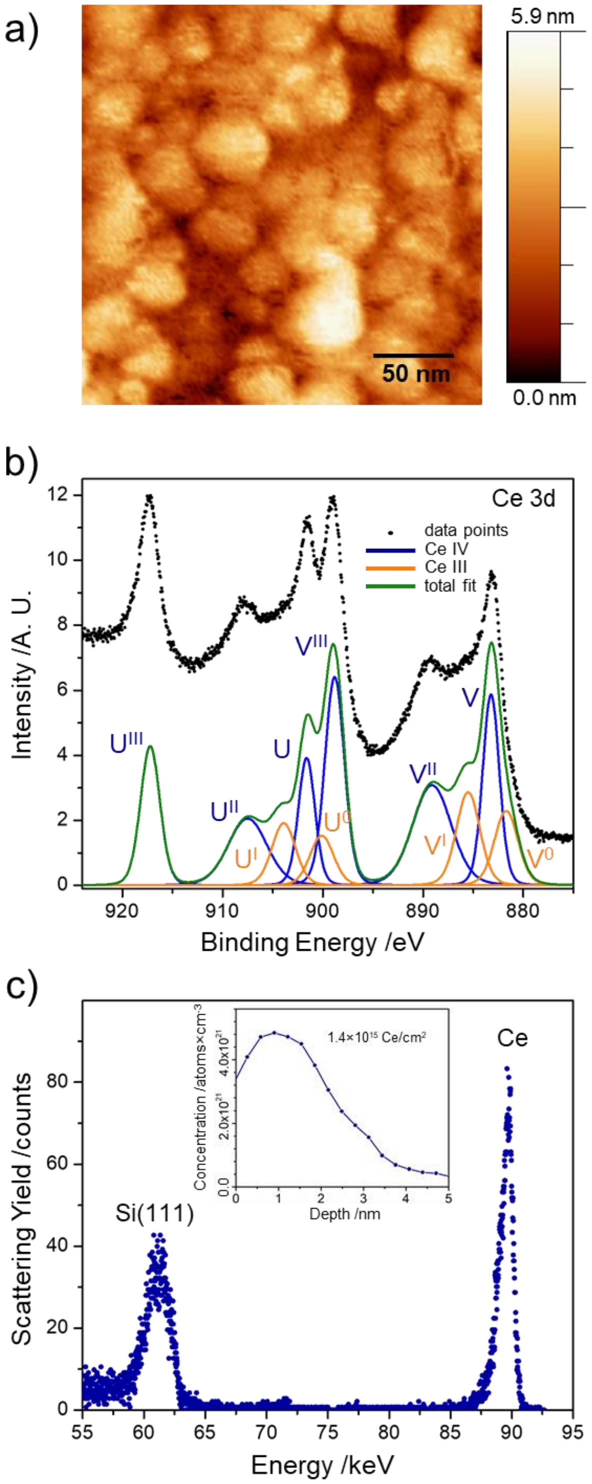

Figure 1. Characteristic AFM image of a) 255 nm × 255 nm of a CeO_2 film grown on Si(111);-b) XP spectrum of the Ce 3d region showing the fitting of the peaks to Ce(III) and Ce(IV) of a CeO_2 film grown on Si(111); Ce(IV) components are shown in blue, Ce(III) components are shown in orange; peaks are labelled according to the nomenclature introduced by Burroughs *et al*. [43]; c) MEIS spectrum showing the intensity of scattered ions as a function of ion energy at a scattering angle of 125.3° of a CeO_2 film grown on Si(111) and in the inset the MEIS derived Ce depth profile indicating an on average 2.5 nm Ce film thickness.

Table 1. Raw XPS areas (normalised counts and %Ce(IV)) from the preparation of a ~1.6 ML Cu on ~1.0 ML Au on a CeO_2/Si(111) sample.

system	Cu $2p_{3/2}$	Ce 3d	% Ce(IV)	Si 2p	Au 4f
Si(111)	-	-	-	13.6	-
CeO_2/Si(111)	-	101.1	91.2	5.7	-
Au/CeO_2/Si(111)	-	91.1	88.6	5.2	8.2
Cu/Au/CeO_2/Si(111)	13.3	83.6	83.2	4.6	8.0

The Ce 3d region was fitted to quantify the relative amounts of Ce(IV) and Ce(III) oxidation states in the thin film. The as-deposited film was found to be almost exclusively constituted of Ce(IV), consistent with the formation of near-stoichiometric CeO_2 films. More details of the fitting procedure used for the Ce 3d region can be found in the Supplementary Information (SI1).

Figure 1c shows the MEIS spectrum from a ceria film on Si(111) prepared under analogous conditions. The cerium peak at ~88 keV has a FWHM of ~1.3 keV and is well separated from the peak caused by gold nanoparticles (expected at ~91 keV). The Ce MEIS peak was converted directly into a depth profile based on well-known inelastic energy loss rates and the silicon random level reference. Shown in the inset in Fig. 1c), it indicates a mean depth of the ceria film of ca. 2.5 nm, and an average deposited cerium dose of 1.4×10^{15} atoms cm^{-2}.

Investigation of the effect of variable CeO_2 film thickness and morphology on MEIS spectra.

The distribution of CeO_2 grown on Si(111) was investigated by MEIS through the PM3 software. Figure 2a shows the MEIS spectrum after the deposition of 2.4 ML Cu followed by 0.54 ML Au onto a CeO_2 film on Si(111). This spectrum confirms that the cerium profile is sufficiently narrow that both copper and gold signals each appear against a flat background, which is important for the PM3 analysis of these signals presented later. Three models were used to represent the CeO_2 arrangement as can be seen in Figure 2b). According to the MEIS spectrum shown in Figure 2a, when the CeO_2 layer is simulated as a continuous thin film the experimental and simulated data show poor agreement at the cerium tail (arrow in figure 2a) and at the silicon edge (~61 keV). The cerium tail can be simulated better by adding a second layer of cerium diffusing into the silicon surface, but the silicon edge continues not to match. To improve further the agreement between experimental and simulated data, a ceria island model was used. In this case, eight steps were created with thickness for the ceria islands ranging from 0 to 3 nm. The fraction of each step of this model can be seen in Figure 2b). In each model the total atomic density (number of atoms per cm^2) was kept constant. This result is in agreement with the AFM images shown in Figure 1 (a-b). The copper and gold nanoparticles on the ceria film do not significantly affect the Ce-related signal since most of the ceria surface is not covered by them. A continuous thin film of metal would result in a shift of the cerium peak to lower energy, such a shift was not observed in the MEIS spectra.

Therefore, the fit to the cerium signal was refined prior to a detailed fitting of the copper and gold peaks. In addition, consistently the inclusion of copper and gold nanoparticles on the ceria films did not significantly change its initial profile.

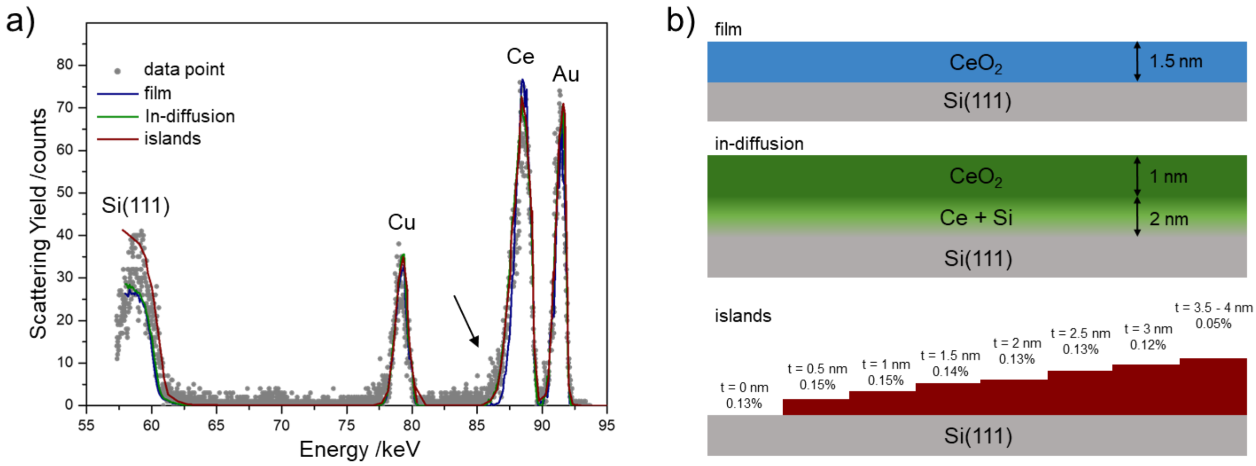

Figure 2. a) MEIS experimental data and simulations for a sample prepared by dosing copper (2.4 ML) followed by gold (0.54 ML) without thermal treatment for the three CeO_2 distribution models and for the backscattering angle of 131.3°. b) Schematic diagrams showing the three models employed for simulating the distributions of the CeO_2 layer morphology and thickness. In the first model a 1.5 nm thick CeO_2 film was used. In the second model a Ce in-diffusion layer was added. In the third model, the CeO_2 film thickness was allowed to vary between 0 and 3 nm, representing islands of CeO_2. Each model has the same number of atoms per cm^2.

The thermal behaviour of a typical CeO_2/Si(111) layer was investigated by XPS. From the analysis of the Ce 3d core level, the Ce(IV):Ce(III) was evaluated as ca. 90%:10% upon preparation. A change of the cerium oxidation state is seen with annealing, reaching a Ce(IV):Ce(III) of ca. 22%:78% after annealing to 500 K. The envelope of the O 1s peak, which contains also the signals of oxygen related to SiO_2 and the Ce-O-Si interfacial oxygen, varies accordingly. Ce 3d and O 1s core level spectra with annealing are reported in SI2.

Deposition of Au onto CeO_2/Si(111)

XPS

The metal vapour deposition of gold was carried out on a CeO_2/Si(111) sample at 300 K resulting in a gold coverage of ~1 ML. XP spectra of the Ce 3d and Au 4f regions are displayed in Figures 3a and 3b. For these XPS experiments, the non-monochromated Al *k*α source was used. The fitting of the Ce 3d region shown in figure 3a reveals that gold deposition results in a small decrease in Ce(IV):Ce(III) composition from ~91% Ce(IV) to ~89% (Table 1). This is consistent with a reduction of the ceria surface during the nucleation of gold particles. The reduction of CeO_2 by the deposition of metallic nanoparticle has been reported previously for a range of metals.[6, 44, 45] The Au $4f_{7/2}$

peak is recorded at 84.6 eV, as reported in figure 3b, a value slightly higher than that expected for metallic gold, 84.0 eV. [6, 46]

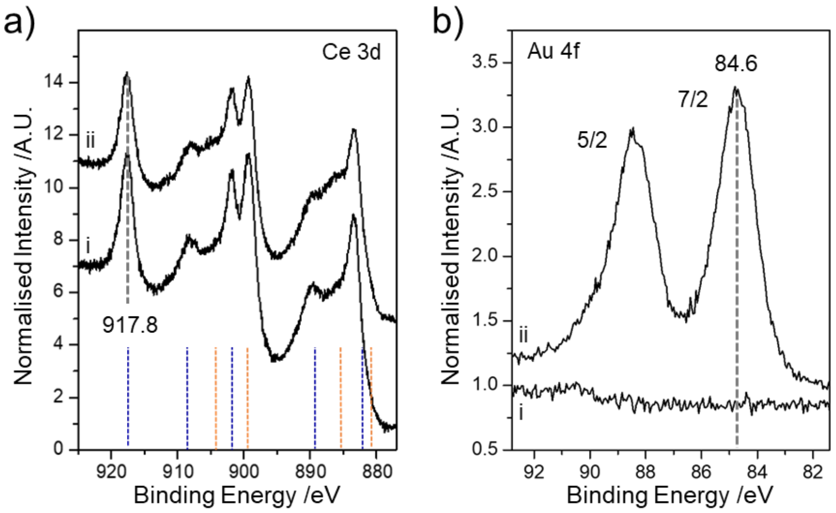

Figure 3. XP spectra displaying a) the Ce 3d region and b) the Au 4f region of the CeO_2/Si(111) surface, i) prior to and ii) after the deposition of ~1 ML Au, at a deposition temperature of 300 K; spectra are offset for clarity. In a) expected positions for Ce(IV)/Ce(III) components are indicated by blue/orange dashed lines.

Deposition of Cu onto Au/CeO_2/Si(111)

XPS:

The metal vapour deposition of copper was carried out on the Au/CeO_2/Si(111) sample at 300 K resulting in a copper coverage of ~1.6 ML. XP spectra of the Cu $2p_{3/2}$, Ce 3d and Au 4f regions before and after deposition of copper are displayed in Figures 4a-c. The Cu $2p_{3/2}$ is recorded at 933.5 eV, as shown in figure 4a; this value is in good agreement with those recorded for both metallic copper and Cu(I) [47]; moreover, no sign of asymmetries or satellite features that could suggest oxidation to Cu(II) can be seen. The Ce 3d region is reported in figure 4b. Table 1 reveals that the Ce 3d signal attenuates by ~9% after deposition of copper. In contrast, the Au 4f signal attenuates by ~2.5%. This is consistent with some copper being deposited onto gold particles, but the majority of the copper coalescing into pure nanoparticles on the ceria surface. The deposition of copper causes a further decrease in the percentage of Ce(IV) from ca. 88.6% to ca. 83.2%. This is consistent with the behaviour previously reported for the growth of copper on CeO_2 and supports the conclusion that copper particles are formed in direct contact with the ceria surface. [48] A small attenuation of the Au 4f peak indicates that some of the copper also condenses over the preformed Au nanoparticles.

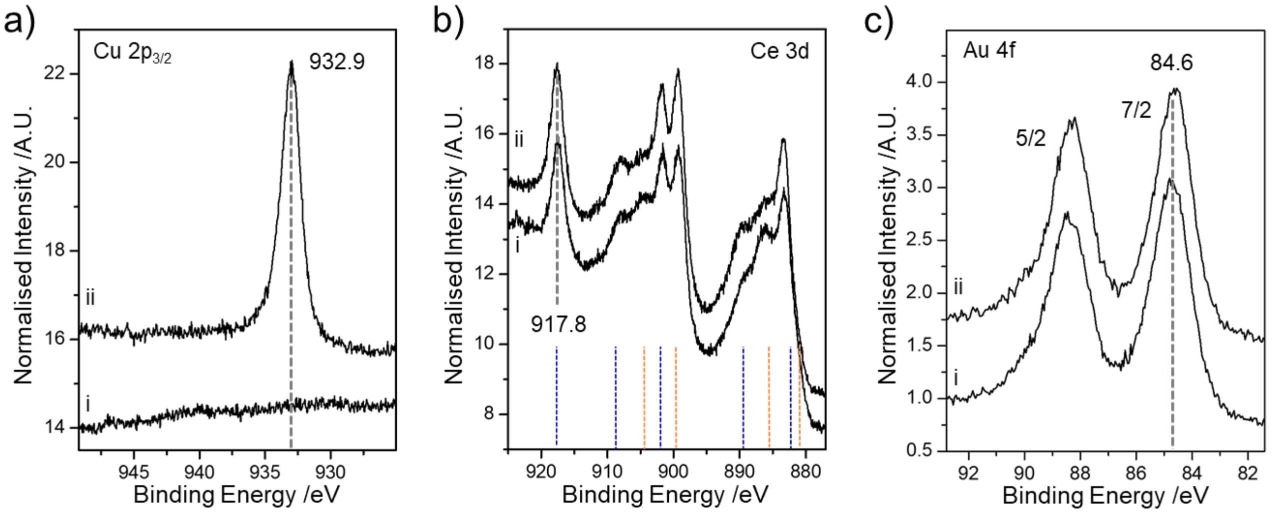

Figure 4. XP spectra of a) the Cu $2p_{3/2}$ region, b) the Ce 3d region and c) the Au 4f region, showing ~1 ML Au/CeO_2/Si(111) i) prior and ii) after deposition of ~1.6 ML Cu at 300 K. In b) expected positions for Ce(IV)/Ce(III) components are indicated by blue/orange dashed lines. Spectra are offset for clarity.

Annealing Cu/Au nanoparticle films on CeO_2/Si(111)

Figure 5 shows Cu $2p_{3/2}$, Ce 3d and Au 4f core levels XP spectra following the annealing of the layer described as above. Additional details, as well as O 1s, C 1s, Si 2p core level spectra, are reported in SI3.1.

The Cu $2p_{3/2}$ is recorded at 933.5 eV and remains essentially constant through the progressively higher annealing temperatures (Figure 5a). The fitting of the Ce 3d region in Figure 5b shows that the Ce(IV):Ce(III) ratio decreases with increasing annealing temperature. Following the highest thermal treatment, the Ce(IV):(III) ratio was found to be ~1:3. Similar behaviour is observed when annealing the CeO_2 thin film on Si(111) (See SI2). This is likely due to transfer of some oxygen from the ceria layer into the silicon substrate and/or desorption of oxygen. [49, 50] The overall intensity of the Ce 3d peaks increases with annealing temperature (Table 2 and Figure 5). Similar behaviour has been observed when annealing a ceria thin film, which was ascribed to a decrease in screening of subsurface cerium atoms when oxygen vacancies are created. [49] Contributions to the increase in the cerium signal could also derive from sintering of the metallic nanoparticles with increasing annealing temperature and from desorption of molecular adsorbates. The Au $4f_{7/2}$ peak, Figure 5c, is recorded at 84.6 eV and remains essentially constant through the annealing treatments. XPS (Table 2 and Figure 5) reveals that there is little change in the intensity of either the Cu $2p_{3/2}$ or Au 4f signals, which suggests that the particle size changes little with increasing annealing temperature.

Table 2. Raw XPS areas (normalised counts and %Ce(IV)) following the annealing of a ~1.6 ML Cu on ~1.0 ML Au on a CeO_2/Si(111) sample.

conditions	Cu $2p_{3/2}$	Ce 3d	% Ce(IV)	Si 2p	Au 4f
As prep, RT	13.3	83.6	83.2	4.6	8.0
Anneal 325 K	12.9	90.3	84.7	4.6	8.1
Anneal 375 K	12.6	88.5	78.9	4.7	7.8
Anneal 425 K	12.5	102.2	52.3	4.5	8.0
Anneal 475 K	12.6	108.5	44.1	4.2	7.2
Anneal 510 K	13.4	110.3	39.3	3.4	8.7
Anneal 540 K	12.2	122.2	23.5	4.2	7.2

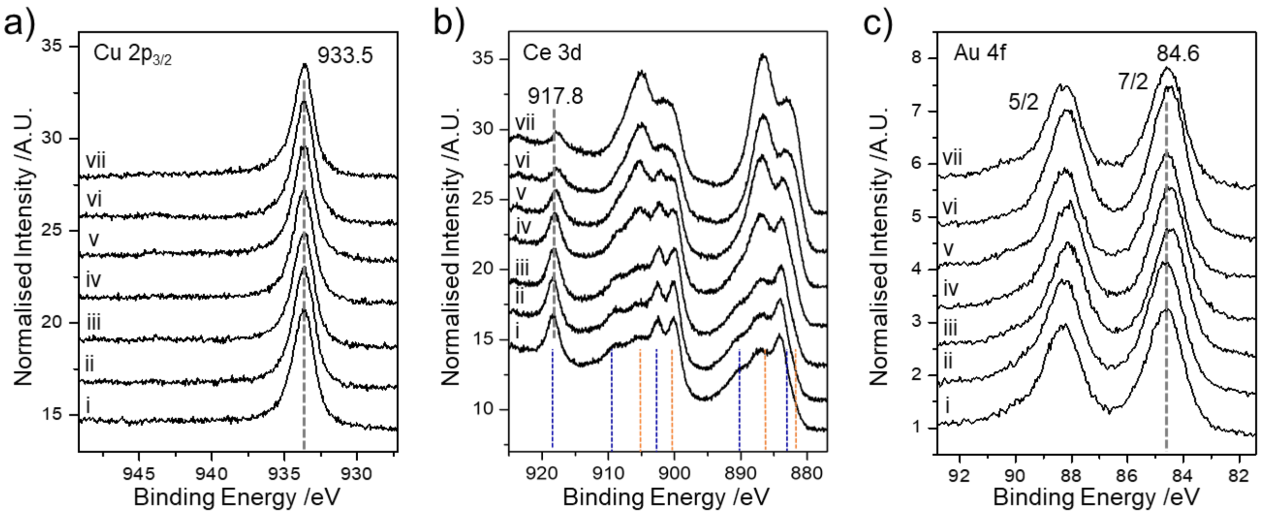

Figure 5. Annealing temperature dependence of XP spectra of the a) Cu $2p_{3/2}$, b) Ce 3d and c) Au 4f core levels for a sample prepared by the deposition of first ~1 ML Au followed by ~1.6 ML onto a ~2 nm CeO_2 film on Si(111) at 300 K; i) as prepared, ii) 325 K, iii) 375 K, iv) 425 K, v) 475 K, vi) 510 K and vii) 540 K. In b) expected positions for Ce(IV)/Ce(III) components are indicated by blue/orange dashed lines. Spectra are offset for clarity.

Cu/Au/CeO_2/Si(111)

MEIS

The PM3 software allowed us to explore several nanoparticle structures such as discrete nanoparticles (NPs), core@shell and alloy, with spherical and hemispherical geometries. In order to evaluate the goodness of the fit for the MEIS spectra the reduced Chi-square analysis was applied.[51] The Chi-square is used as a figure-of-merit for the evaluation of goodness of fit for MEIS spectra. In this work, we used the reduced Chi-square given by Equation 1:

$$\chi^2 = \frac{1}{N}\sum_{i=1}^{N}\left\{\frac{\left[I_{exp} - I_{sim} + min\left(I_{exp},1\right)\right]^2}{I_{exp}+1}\right\} \qquad \text{Eq. 1}$$

where *N* is the total number of data points, I_{exp} and I_{sim}represent the experimental and simulated spectra, respectively.[51] The min(I_{exp},1) factor is used to take into account cases of low counts. Equation 1 was applied to three ion backscattering angles (119.3°, 125.3° and 131.3°) with the same energy range for the analysis presented in this work and the mean Chi-square result was taken.

A sample was prepared by first depositing 0.14 ML Au followed by 0.6 ML Cu onto ~2 nm CeO_2/Si(111) at 300 K. MEIS data were acquired for the as-prepared sample and following annealing the same sample to 350, 425 and 525 K. The Chi-square analysis (inset in Figure 6) reveals that the best fit to the MEIS data (see S4.1) for the as-deposited sample was for discrete NPs of Cu (radius 1.5 nm) and Au (radius 2 nm) adopting a hemispherical shape. Cu nanoparticles were found to cover approximately 10% of the ceria surface, while Au particles covered approximately 2% of the surface. The fit for a core-shell morphology was only marginally less good. The possibility of a mixture of discrete particles and Au(core)@Cu(shell) particles is consistent with our XPS data following a similar sample preparation. On annealing, the particle morphology was found to be relatively stable up to ~425 K. After annealing to 525 K, the PowerMEIS Chi-square analysis now shows approximately similar values for discrete Cu and Au particles; particles with an alloy shell surrounding a Cu core and alloyed ($Au_{0.25}Cu_{0.75}$) particles. The MEIS data are consistent with a clear change occurring compared to the lower annealing temperatures and it is likely that a mixture of particle morphologies and compositions is present under these conditions caused by diffusion, agglomeration and intermixing processes at this elevated temperature. MEIS spectra and PowerMEIS fits are reported in SI4.1.

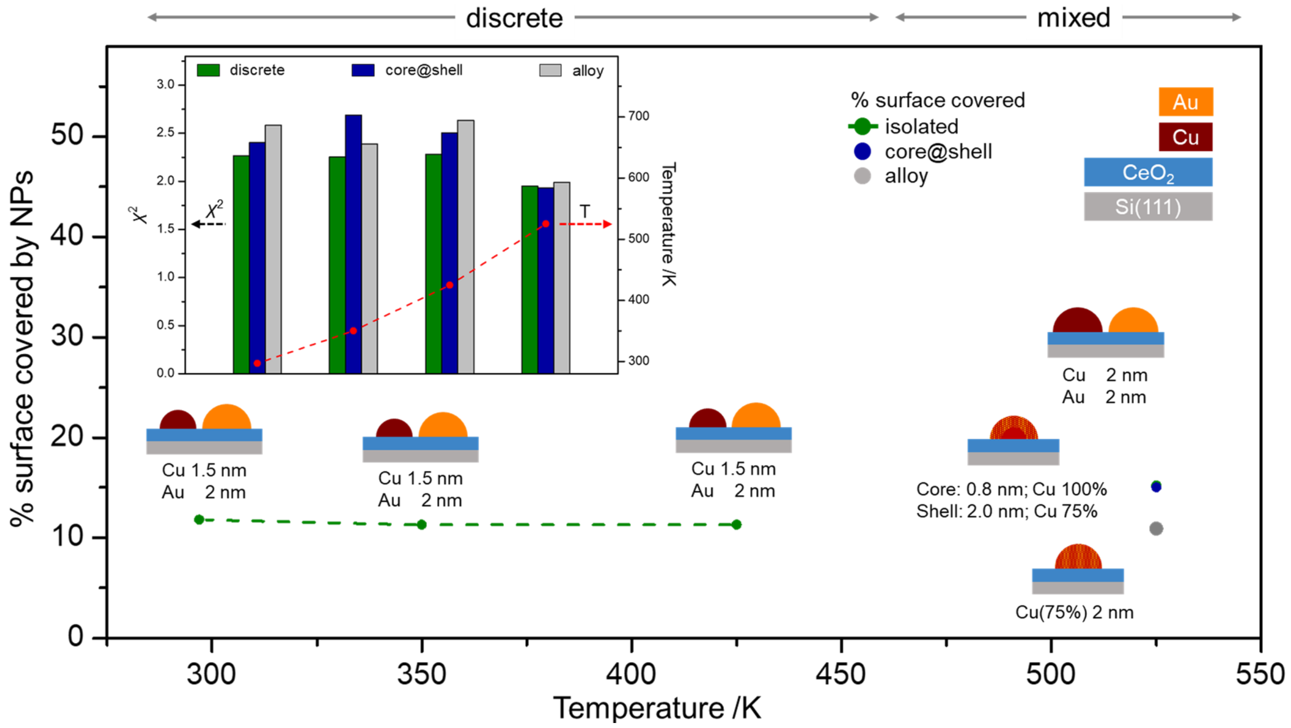

Figure 6. Nanoparticle radii, morphology and % of surface covered by nanoparticles as a function of annealing temperature for the samples prepared by the deposition of 0.14 ML Au followed by 0.6 ML Cu onto a ~2 nm CeO_2 film on Si(111) as deposited (~300 K) and annealed to 350, 425 and 525 K. In the inset, Chi-square analysis for the same samples obtained from the three ion backscattering angles (119.3°, 125.3° and 131.3°). Green, blue and grey bars indicate the use of a model with discrete NPs, core@shell and alloy, respectively.

To summarise the XPS and MEIS findings, XPS shows that when vapour depositing gold onto a CeO_2(111) film, a small charge transfer occurs on deposition, with cerium being slightly reduced and gold slightly oxidised. On addition of copper, metallic particles are nucleated, but a further reduction of ceria seems to occur. A slight decrease of the Au 4f intensity indicates that some preformed gold particles are coated by a copper layer. On annealing, the Cu $2p_{3/2}$ and Au 4f peaks stay approximately constant in both binding energy and intensity. Annealing causes an increase in the reduction of CeO_2, mimicking the behaviour observed upon annealing the CeO_2 films on Si(111). This could indicate that the metal NPs are thermally stable from the XPS point of view and there is minimal interaction with the substrate, with reduction of ceria being ascribed primarily to loss of oxygen. The MEIS analysis is consistent with the XPS results indicating isolated gold nanoparticles are formed on ceria, with subsequent growth of both isolated copper particles and copper particles on pre-formed gold particles upon deposition of copper onto Au/CeO_2/Si(111). This morphology remains stable on annealing to 425 K, though increases in particle size and alloy formation are observed following annealing to 525 K.

Influence of annealing on an air-exposed Au/Cu/CeO_2/Si(111) sample

XPS

A sample was prepared by the deposition of first ~1.5 ML copper followed by ~1.0 ML gold onto a ~1.5 nm CeO_2 film on Si(111). The sample was exposed to air before being introduced into the XPS chamber for analysis. For these XPS experiments, the monochromated Al k_α source was used. Deposition of copper on the relatively well-defined CeO_2(111) surface has been shown to be initiated at step edges.[52, 53] It has been reported that charge transfer from the oxide to copper species leads to the formation of Cu(I) [2, 45] which are thought to be located at the interface with ceria and covered by Cu(0) species.[54] Gold deposition onto Cu/CeO_2 can result in decoration of pre-existing copper particles or the formation of isolated gold particles or a combination of both effects.

Figure 7a-c show the Cu $2p_{3/2}$, Ce 3d and Au 4f regions as a function of annealing temperature. The annealing temperatures reported are, we believe, accurate to within about 25 K due to difficulties in measuring the sample temperature using this specific sample holder. After deposition of the metal nanoparticles, and subsequent exposure to air, the Cu $2p_{3/2}$ region shows a signal that can be fitted with two components (Figure 7a), one with maximum at a binding energy (BE) of 933.6 eV, attributed to copper in the I/0 oxidation state, and one at 935.5 eV, which is associated with Cu(II).[47, 55]

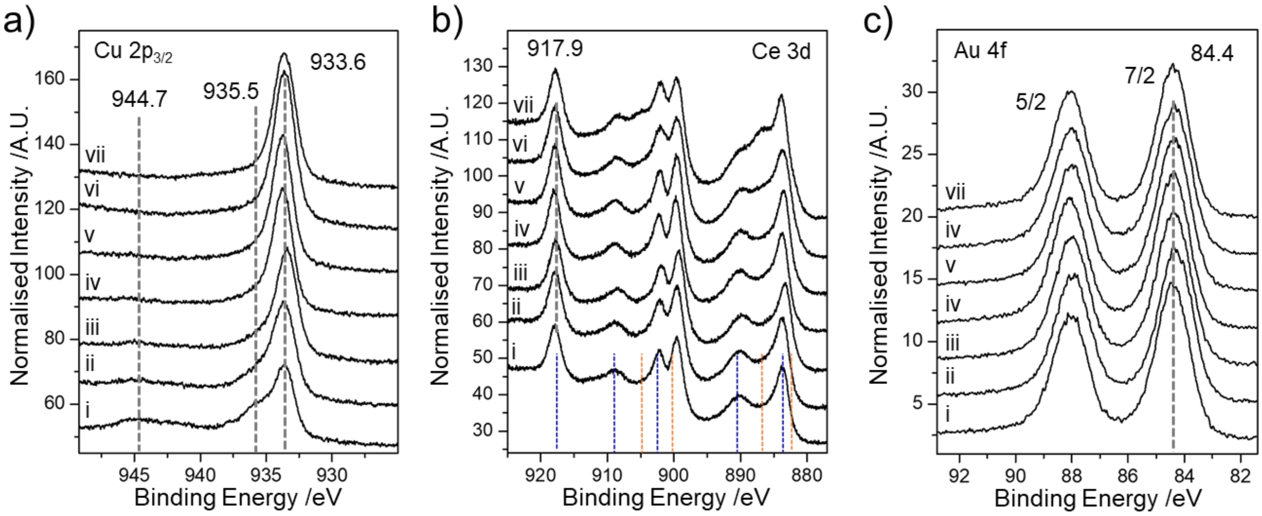

Figure 7. Annealing temperature dependence of XP spectra of the Cu $2p_{3/2}$, Ce 3d and Au 4f core levels for a sample prepared by the deposition of first ~1.5 ML Cu followed by ~1.0 ML Au onto a ~2 nm CeO_2 film on Si(111) at 300 K; i) as prepared, ii) 330 K, iii) 350 K, iv) 370 K, v) 385 K, vi) 400 K and vii) 425 K. In b) expected positions for Ce(IV)/Ce(III) components are indicated by blue/orange dashed lines. Spectra are offset for clarity.

Table 3. Raw XPS areas (normalised counts and %Ce(IV)) from a ~1.0 ML Au on ~1.5 ML Cu on CeO_2/Si(111) after exposure to air and as a function of annealing temperature

conditions	**Cu $2p_{3/2}$**	**Ce 3d**	**% Ce(IV)**	**Si 2p**	**Au 4f**
As prep, RT	60.30	191.61	89.9	19.73	37.02
Anneal 330 K	72.28	234.86	87.6	19.69	37.74
Anneal 350 K	76.47	217.84	91.0	19.27	37.59
Anneal 370 K	77.09	228.43	86.8	20.17	36.40
Anneal 385 K	84.69	269.18	84.6	19.21	36.88
Anneal 400 K	96.76	312.41	88.7	19.52	36.08
Anneal 425 K	60.30	302.89	74.8	19.73	37.02

The raised background at ca. 944 eV is attributed to the shake-up satellite features of Cu(II). A BE of 933.6 eV is approximately 1 eV higher than that typically observed for metallic copper particles.[56] Similar behaviour was reported in XP spectra of small copper particles deposited onto a single crystal ZnO surface where the authors concluded that small copper particles are partially oxidised due to the interaction with the ZnO surface.[57] With annealing to increasing temperature, the signals associated to Cu(II) decrease in intensity, the shake-up satellites attenuate and the lower BE component increases (Figure 7a). Each of these observations imply that the Cu(II) component reduces to Cu(I/0). A small shift of the lower BE peak is observed with increasing annealing temperature.

Figure 7b) shows that after preparation, the Ce 3d region shows the typical signature of cerium in the +IV oxidation state. With annealing, the decrease of the peaks related to Ce(IV) and the corresponding increase of the signals related to Ce(III) are recorded. The overall Ce(IV):Ce(III) composition % goes from ca. 90/10% after preparation to ca. 75/25% after annealing to 425 K. (see Table 3) The Au $4f_{7/2}$ is recorded at 84.4 eV, as shown in Figure 7c. The signal stays constant in position and shape throughout the annealing experiments. As observed for the main peak of copper, also the BE of Au 4f peaks are recorded at slightly higher BE than that expected for metallic gold.[6] Small gold particles have been reported to be partially oxidised on ceria surfaces, but a shift to higher binding energy has also been reported for Cu/Au alloys compared with pure gold.[58, 59]

Table 3 shows the variation of peak area for the Cu $2p_{3/2}$, Ce 3d, Si 2p, and Au 4f signals as a function of temperature obtained from the fitting procedure, and additional details are reported in SI3.2.

The Ce 3d and Cu $2p_{3/2}$ signals are seen to increase in intensity whereas that of Au 4f stays constant overall. On the basis of the XPS data, there are a number of possible interpretations of the variation in Ce 3d, Cu $2p_{3/2}$ and Au 4f intensities with increasing annealing temperature. The increase in the Ce 3d signal may indicate that the metal nanoparticles are sintering with increasing temperature, therefore exposing a larger area of bare ceria. However, one would expect a decrease in the overall intensity of the Cu $2p_{3/2}$ and Au 4f signals, which is not observed. The exposure of the sample to air causes the adsorption of carbon and oxygen containing species (e.g. OH^-, HCO_3^-, CO_3^{2-}). The thermally induced desorption of these species is likely to occur from copper and ceria sites rather than from less reactive gold sites. The deposition of copper onto ceria typically produces hemispherical copper particles.[53] As will be shown below, MEIS indicates that the copper particles have a radius of ~2.5 – 3.0 nm. Assuming a uniform array of particles on the CeO_2 surface, an array of copper particles can be envisaged whose centres are separated by between 10 and 14 nm. The subsequent deposition of gold is likely to result in gold nucleation on top of existing copper particles rather than the formation of isolated gold particles, given that Au-Cu bonds are thermodynamically more favourable than Au/ceria bonds especially when copper particles are already nucleated on the most favourable CeO_2 sites.[52, 53, 60] The relatively constant Au 4f signal as a function of increasing annealing temperature coupled with an increasing Cu $2p_{3/2}$ signal could be interpreted as being due to desorption of molecular species from bimetallic particles and intermixing of gold with copper.

MEIS: Au/Cu/CeO_2/Si(111)

Figure 8 summarizes our findings of the MEIS investigations of the samples when copper is first deposited followed by gold. MEIS spectra and PowerMEIS fits are reported in SI4.2. Figure 8 b) showing the NP's stoichiometry as a function of annealing temperature. After preparation in vacuum, PowerMEIS simulations of the data taken at 300 K indicate that the most likely nanoparticle structure corresponds to hemispherical particles of radius 2.5 nm with a Cu core of radius 1.3 nm and an alloy shell of composition 78% Cu giving an overall particle stoichiometry of ~80% Cu. After air exposure and annealing to 375 K, XPS reveals the presence of significant Cu(II) as well as C and O containing adsorbates. Under these conditions, analysis of the MEIS data reveals the formation of an exclusively Cu shell of thickness 0.6 nm surrounding a bimetallic core of radius 2.2 nm and with a Cu concentration of 45%. Segregation of Cu to the surface induced by exposure to atmospheric oxygen would be expected. PowerMEIS analysis of samples annealed to temperatures above 375 K is consistent with the formation of homogeneous alloy particles of a gradually increasing particle size an whose overall composition becomes slightly richer in gold.

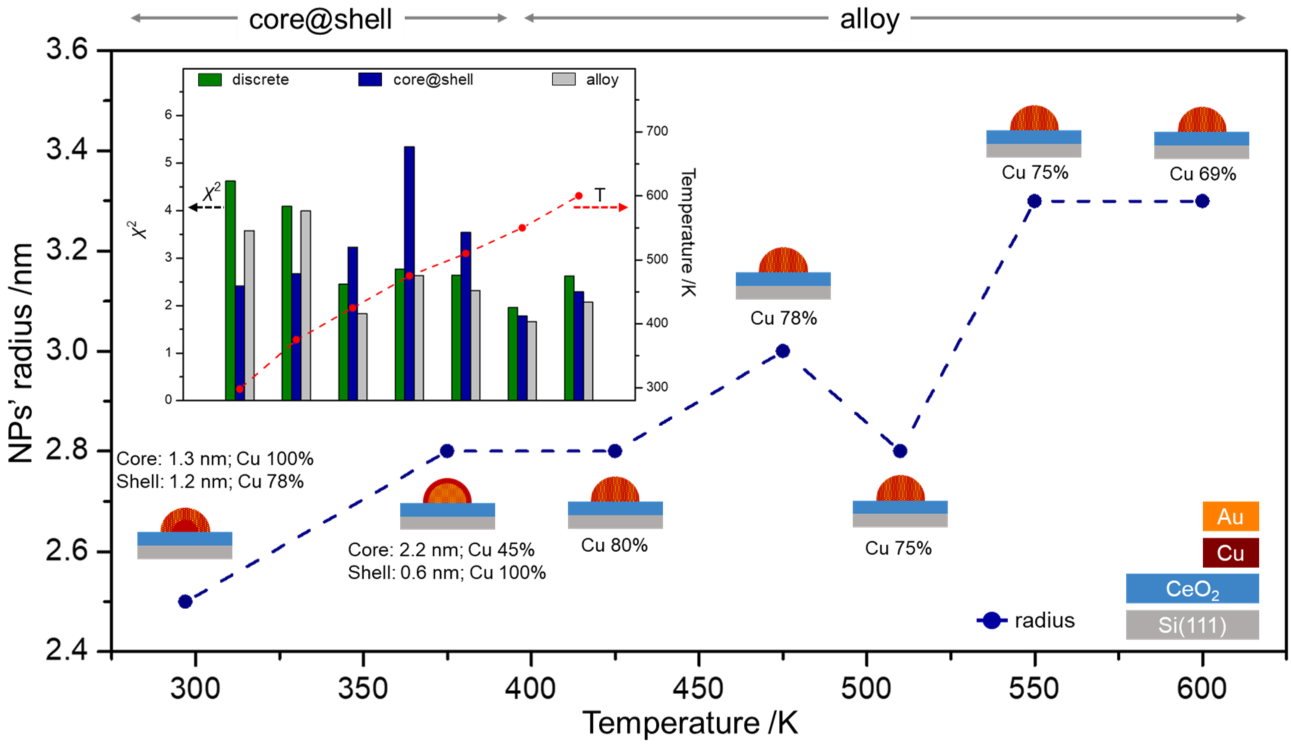

Figure 8. Nanoparticle radius, stoichiometry and morphology as a function of annealing temperature for the samples prepared by the deposition of ~1.5 ML Cu followed by ~1.0 ML Au onto a ~1.5 nm CeO$_2$ film on Si(111) as deposited and annealed to 375, 425, 475, 510, 550 and 600 K. Composition % is given with respect to Cu. In the inset, Chi-square analysis for the same samples obtained from the three ion backscattering angles (119.3°, 125.3° and 131.3°). Green, blue and grey bars indicate the use of a model with discrete NPs, core@shell and alloy, respectively.

Conclusions

A preparation method has been established for producing Au/Cu/CeO$_2$ model catalysts for analysis by MEIS consisting of a ~2 nm CeO$_2$ film deposited onto Si(111) followed by metal vapour deposition of elemental Cu and Au.

XPS reveals that the ceria film is initially almost pure CeO$_2$ in composition. On annealing a CeO$_2$/Si(111) sample, a gradual reduction is observed caused presumably by a combination of oxygen desorption and diffusion of oxygen into the Si substrate.

Deposition of Au onto the CeO$_2$/Si(111) surface at 300 K leads to a slightly lower Ce(IV):Ce(III) ratio. Deposition of Cu onto the precovered Au/CeO$_2$/Si(111) surface leads to further Ce(IV) reduction. In addition, a slight attenuation of the Au signal is observed. These observations are consistent with the formation of mainly pure Au and pure Cu particles with some Cu deposition onto Au particles. PowerMEIS analysis supports this conclusion, with the best fit to the MEIS data corresponding to discrete hemispherical Au (radius 2 nm) and Cu (radius 1.5 nm) particles. These particles are relatively thermally stable up to at least 450 K. The most physically realistic model for the sample after annealing to 525 K involves the formation of hemispherical alloyed CuAu particles (radius 2 nm).

A sample prepared by deposition of Cu followed by Au onto CeO_2/Si(111) was exposed to air. XPS revealed the presence of Cu(II) species following air exposure which are reduced to Cu/Cu(I) with increasing annealing temperature. Annealing to 375 K caused desorption of weakly bound adsorbates and MEIS revealed that under these conditions the sample consisted of nanoparticles with a Au rich core and a Cu rich shell. Annealing to higher temperatures resulted in the formation of alloyed particles. MEIS revealed that initially core-shell particles were produced after deposition of Cu followed by Au in vacuum. On exposure to air, Cu segregation to the surface was observed. Annealing to higher temperatures produced MEIS data that were consistent with the formation of homogeneously alloyed particles.

The powerful combination of XPS and MEIS allows significant insight into the thermal behaviour of Cu and Au particles on the ceria surface providing information on alloying behaviour, particle size and the electronic interaction with the CeO_2 support material. In fact, this work suggests that discrete Cu and Au particles are stable up to 450 K on the CeO_2 surface. When preparing Cu/Au/CeO_2 catalysts for selective hydrogenation of furfural, as discrete metal particles are desirable, the thermal treatment of the catalyst should be considered carefully in order to minimise alloy formation.

Acknowledgements

RM and FG acknowledge funding from EPSRC grants (RM: EP/506631/1; FG: EP/M029077/1). JAvdB and AR acknowledge the EPSRC funding for the use of the MEIS facility at the University of Huddersfield within grant EP/M029077/1. This study was financed in part by the Coordenação de Aperfeiçoamento de Pessoal de Nível Superior - Brasil (CAPES) - Finance Code 001, by Conselho Nacional de Desenvolvimento Científico e Tecnológico (CNPq), and PRONEX-FAPERGS 16/2551-0000479-0.

The research data supporting this publication can be accessed at http://dx.doi.org/10.17630/c6bcbb11-ffd3-497c-bd12-7e09bdcc31d9 to be activated upon acceptance.

Supporting material description: fitting of Ce 3d XPS region; XPS of CeO_2/Si(111) with annealing; XPS of (Cu+Au)/CeO_2/Si(111) with annealing; MEIS spectra and respective PowerMEIS fits of (Cu+Au)/CeO_2/Si(111) with annealing

References

[1] A. T. Bell, The impact of nanoscience on heterogeneous catalysis, Science, 299 (2003) 1688-1691.

[2] M. M. Branda, N. C. Hernandez, J. F. Sanz, F. Illas, Density Functional Theory Study of the Interaction of Cu, Ag, and Au Atoms with the Regular CeO_2 (111) Surface, Journal of Physical Chemistry C, 114 (2010) 1934-1941.

[3] A. Trovarelli, Catalytic properties of ceria and CeO_2-containing materials, Catal. Rev.-Sci. Eng., 38 (1996) 439-520.

[4] J. Kaspar, P. Fornasiero, M. Graziani, Use of CeO_2-based oxides in the three-way catalysis, Catalysis Today, 50 (1999) 285-298.

[5] L. J. Chen, Y. H. Tang, L. X. Cui, C. Y. Ouyang, S. Q. Shi, Charge transfer and formation of Ce^{3+} upon adsorption of metal atom M (M = Cu, Ag, Au) on CeO_2 (100) surface, Journal of Power Sources, 234 (2013) 69-81.

[6] M. Baron, O. Bondarchuk, D. Stacchiola, S. Shaikhutdinov, H. J. Freund, Interaction of Gold with Cerium Oxide Supports: CeO_2(111) Thin Films vs CeO_x Nanoparticles, Journal of Physical Chemistry C, 113 (2009) 6042-6049.

[7] F. Tao, S. R. Zhang, L. Nguyen, X. Q. Zhang, Action of bimetallic nanocatalysts under reaction conditions and during catalysis: evolution of chemistry from high vacuum conditions to reaction conditions, Chemical Society Reviews, 41 (2012) 7980-7993.

[8] E. Völker, F. J. Williams, E. J. Calvo, T. Jacob, D. J. Schiffrin, O2 induced Cu surface segregation in Au–Cu alloys studied by angle resolved XPS and DFT modelling, Physical Chemistry Chemical Physics, 14 (2012) 7448-7455.

[9] N. Artrith, A. M. Kolpak, Grand canonical molecular dynamics simulations of Cu-Au nanoalloys in thermal equilibrium using reactive ANN potentials, Computational Materials Science, 110 (2015) 20-28.

[10] N. Artrith, A. M. Kolpak, Understanding the Composition and Activity of Electrocatalytic Nanoalloys in Aqueous Solvents: A Combination of DFT and Accurate Neural Network Potentials, Nano Letters, 14 (2014) 2670-2676.

[11] X. M. Liao, V. Pitchon, P. H. Cuong, W. Chu, V. Caps, Hydrogenation of cinnamaldehyde over bimetallic Au-Cu/CeO_2 catalyst under a mild condition, Chinese Chemical Letters, 28 (2017) 293-296.

[12] X. M. Liao, W. Chu, X. Y. Dai, V. Pitchon, Bimetallic Au-Cu supported on ceria for PROX reaction: Effects of Cu/Au atomic ratios and thermal pretreatments, Applied Catalysis B-Environmental, 142 (2013) 25-37.

[13] R. Fiorenza, C. Crisafulli, G. G. Condorelli, F. Lupo, S. Scire, Au-Ag/CeO_2 and Au-Cu/CeO_2 Catalysts for Volatile Organic Compounds Oxidation and CO Preferential Oxidation, Catalysis Letters, 145 (2015) 1691-1702.

[14] L. Zhang, H. Y. Kim, G. Henkelman, CO Oxidation at the Au-Cu Interface of Bimetallic Nanoclusters Supported on CeO_2(111), Journal of Physical Chemistry Letters, 4 (2013) 2943-2947.

[15] N. K. Gamboa-Rosales, J. L. Ayastuy, M. P. Gonzalez-Marcos, M. A. Gutierrez-Ortiz, Oxygen-enhanced water gas shift over ceria-supported Au-Cu bimetallic catalysts prepared by wet impregnation and deposition-precipitation, International Journal of Hydrogen Energy, 37 (2012) 7005-7016.

[16] B. B. Chen, X. M. Li, R. J. Zheng, R. P. Chen, X. Sun, Bimetallic (Au-Cu core)@(ceria shell) nanotubes for photocatalytic oxidation of benzyl alcohol: improved reactivity by Cu, Journal of Materials Chemistry A, 5 (2017) 13382-13391.

[17] C. Pojanavaraphan, A. Luengnaruemitchai, E. Gulari, Catalytic activity of Au-Cu/CeO_2-ZrO_2 catalysts in steam reforming of methanol, Applied Catalysis a-General, 456 (2013) 135-143.

[18] C. Pischetola, L. Collado, M. A. Keane, F. Cardenas-Lizana, Gas Phase Hydrogenation of Furaldehydes via Coupling with Alcohol Dehydrogenation over Ceria Supported Au-Cu, Molecules, 23 (2018).

[19] R. F. Zhang, X. F. Kong, H. T. Wang, S. H. Zhang, D. Legut, S. H. Sheng, S. Srinivasan, K. Rajan, T. C. Germann, An informatics guided classification of miscible and immiscible binary alloy systems, Scientific Reports, 7 (2017) 9577.

[20] W. B. Pearson, Handbook of Lattice Spacings and Structures of Metals and Alloys (Pergamon, London, 1958).

[21] J. Hennig, D. Mari, R. Schaller, Order-disorder phase transition and stress-induced diffusion in Au-Cu, Physical Review B, 79 (2009) 144116.

[22] Y. Feutelais, B. Legendre, M. Guymont, New enthalpies determination and in situ X-ray diffraction observations of order/disorder transitions in $Au_{0.5}Cu_{0.5}$, Acta Materialia, 47 (1999) 2539-2551.

[23] X. Zhao, P. Liu, J. Hrbek, J.A. Rodriguez, M. Pérez, The chemisorption of SO_2 on the Cu/Au(111) surface: Interplay between ensemble and electronic effects, Surface Science, 592 (2005) 25-36.

[24] L. Wang, P. Li, H. Shi, Z. Li, K. Wu, X. Shao, Thickness-Dependent Adsorption of Melamine on Cu/Au(111) Films, The Journal of Physical Chemistry C, 121 (2017) 7977-7984.

[25] F. Grillo, R. Megginson, D. Batchelor, M. Muntwiler, C. J. Baddeley, Structural and electronic characterization of Cu/Au(111) near-surface alloys, Japanese Journal of Applied Physics, 58 (2019) 5.

[26] F. Grillo, R. Megginson, J. Christie, S. M. Francis, N. V. Richardson, C. J. Baddeley, Structure and Reactivity of Cu-doped Au(111) Surfaces, e-Journal of Surface Science and Nanotechnology, 16 (2018) 163-171.

[27] F. Grillo, H. Früchtl, S. M. Francis, N. V. Richardson, Site selectivity in the growth of copper islands on Au (111), New Journal of Physics, 13 (2011).

[28] Q. Liu, Y. Ning, W. Huang, Q. Fu, F. Yang, X. Bao, Origin of the Thickness-Dependent Oxidation of Ultrathin Cu Films on Au(111), The Journal of Physical Chemistry C, 122 (2018) 8364-8372.

[29] W. Wang, H. Shi, L. Wang, Z. Li, H. Shi, K. Wu, X. Shao, Comparison Study of Structural Properties and CO Adsorption on the Cu/Au(111) and Au/Cu(111) Thin Films, The Journal of Physical Chemistry C, 122 (2018) 19551-19559.

[30] S. Deckers, F. Habraken, W. F. Vanderweg, A. W. D. Vandergon, J. F. Vanderveen, J. W. Geus, Oxidation-induced segregation at the $Pt0_{.5}Ni_{0.5}$(111) surface studied by medium energy ion scattering, G, Applied Surface Science, 45 (1990) 121-129.

[31] C. J. Baddeley, L. H. Bloxham, S. C. Laroze, R. Raval, T. C. Q. Noakes, P. Bailey, Quantitative analysis of adsorbate induced segregation at bimetallic surfaces: Improving the accuracy of medium energy ion scattering results, Journal of Physical Chemistry B, 105 (2001) 2766-2772.

[32] V. Z. C. Paes, M. V. Castegnaro, D. L. Baptista, P. L. Grande, J. Morais, Unveiling the Inner Structure of PtPd Nanoparticles, Journal of Physical Chemistry C, 121 (2017) 19461-19466.

[33] D. F. Sanchez, R. Moiraghi, F. P. Cometto, M. A. Perez, P. F. P. Fichtner, P. L. Grande, Morphological and compositional characteristics of bimetallic core@shell nanoparticles revealed by MEIS, Applied Surface Science, 330 (2015) 164-171.

[34] M. A. Sortica, P. L. Grande, G. Machado, L. Miotti, Characterization of nanoparticles through medium-energy ion scattering, Journal of Applied Physics, 106 (2009).

[35] J. Gustafson, A. R. Haire, C. J. Baddeley, Depth-profiling the composition of bimetallic nanoparticles using medium energy ion scattering, Surface Science, 605 (2011) 220-224.

[36] G. G. Marmitt, PowerMEIS-3 simulation code, http://tars.if.ufrgs.br/.

[37] G. G. Marmitt, Metal oxides of resistive memories investigated by electron and ion backscattering, Ph.D. thesis, Universidade Federal do Rio Grande do Sul, Porto Alegre (2017), https://lume.ufrgs.br/handle/10183/170451.

[38] J. F. Ziegler, J. P. Biersack, U. Littmark, The Stopping and Range of Ions in Solids, vol. 1 of The Stopping and Ranges of Ions in Matter: Stopping tables SRIM 97 (Pergamon Press, New York, 1985).

[39] W. K. Chu, Calculation of energy straggling for protons and helium ions, Physical Review A, 13 (1976) 2057-2060.

[40] J. B. Marion, F. C. Young, Nuclear Reaction Analysis, Graphs and Tables (North Holland Publishing Company, Amsterdam, 1968).

[41] H. Trombini, G. G. Marmitt, I. Alencar, D. L. Baptista, S. Reboh, F. Mazen, R. B. Pinheiro, D. F. Sanchez, C. A. Senna, B. S. Archanjo, C. A. Achete, P. L. Grande, Unraveling structural and compositional information in 3D FinFET electronic devices, Scientific Reports, 9 (2019).

[42] X. C. Zheng, X. L. Zhang, Z. Y. Fang, X. Y. Wang, S. R. Wang, S. H. Wu, Characterization and catalysis studies of CuO/CeO_2 model catalysts, Catalysis Communications, 7 (2006) 701-704.

[43] P. Burroughs, A. Hamnett, A. F. Orchard, G. Thornton, Satellite structure in the X-ray photoelectron spectra of some binary and mixed oxides of lanthanum and cerium, Journal of the Chemical Society, Dalton Transactions, (1976) 1686-1698.

[44] J. L. Lu, H. J. Gao, S. Shaikhutdinov, H. J. Freund, Gold supported on well-ordered ceria films: nucleation, growth and morphology in CO oxidation reaction, Catalysis Letters, 114 (2007) 8-16.

[45] Y. H. Tang, H. Zhang, L. X. Cui, C. Y. Ouyang, S. Q. Shi, W .H. Tang, H. Li, L. Q. Chen, Electronic states of metal (Cu, Ag, Au) atom on CeO_2(111) surface: The role of local structural distortion, Journal of Power Sources, 197 (2012) 28-37.

[46] N. C. Hernández, R. Grau-Crespo, N. H. de Leeuw, J. F. Sanz, Electronic charge transfer between ceria surfaces and gold adatoms: a GGA+U investigation, Physical Chemistry Chemical Physics, 11 (2009) 5246-5252.

[47] M. C. Biesinger, Advanced analysis of copper X-ray photoelectron spectra, Surf. Interface Anal., 49 (2017) 1325-1334.

[48] G. H. Li, S. W. Hu, Q. Xu, J. F. Zhu, Interaction between Cu Nanoparticles and CeO_2(111) Film Surfaces, Journal of Physical Chemistry C, 123 (2019) 23563-23571.

[49] P. Sapkota, A. Aprahamian, K. Y. Chan, B. Frentz, K. T. Macon, S. Ptasinska, D. Robertson, K. Manukyan, Irradiation-induced reactions at the $CeO_2/SiO_2/Si$ interface, The Journal of Chemical Physics, 152 (2020) 104704.

[50] M. Vorokhta, I. Matolinova, M. Dubau, S. Haviar, I. Khalakhan, K. Sevcikova, T. Mori, H. Yoshikawa, V. Matolin, HAXPES study of CeOx thin film-silicon oxide interface, Applied Surface Science, 303 (2014) 46-53.

[51] K. J. Mighell, Parameter estimation in astronomy with Poisson-distributed data. I. The χ_γ^2 statistic, Astrophys. J., 518 (1999) 380-393.

[52] T. E. James, S. L. Hemmingson, C. T. Campbell, Energy of Supported Metal Catalysts: From Single Atoms to Large Metal Nanoparticles, ACS Catalysis, 5 (2015) 5673-5678.

[53] T. E. James, S. L. Hemmingson, T. Ito, C. T. Campbell, Energetics of Cu Adsorption and Adhesion onto Reduced CeO_2(111) Surfaces by Calorimetry, The Journal of Physical Chemistry C, 119 (2015) 17209-17217.

[54] L. Szabova, T. Skala, I. Matolinova, S. Fabris, M. F. Camellone, V. Matolin, Copper-ceria interaction: A combined photoemission and DFT study, Applied Surface Science, 267 (2013) 12-16.

[55] D. Tahir, S. Tougaard, Electronic and optical properties of Cu, CuO and Cu_2O studied by electron spectroscopy, Journal of Physics-Condensed Matter, 24 (2012).

[56] Y. T. Wu, E. Garfunkel, T. E. Madey, Initial stages of Cu growth on ordered Al_2O_3 ultrathin films, Journal of Vacuum Science & Technology a-Vacuum Surfaces and Films, 14 (1996) 1662-1667.

[57] M. C. Patterson, X. Nie, F. Wang, R. L. Kurtz, S. B. Sinnott, A. Asthagiri, P. T. Sprunger, Growth and Structure of Cu and Au on the Nonpolar ZnO$(10\bar{1}0)$ Surface: STM, XPS, and DFT Studies, The Journal of Physical Chemistry C, 117 (2013) 18386-18397.

[58] T .K. Sham, A. Hiraya, M. Watanabe, Electronic structure of Cu-Au alloys from the Cu perspective: A Cu $L_{3,2}$-edge study, Physical Review B, 55 (1997) 7585-7592.

[59] M. Kuhn, T. K. Sham, Charge redistribution and electronic behavior in a series of Au-Cu alloys, Physical Review B, 49 (1994) 1647-1661.

[60] S. L. Hemmingson, C. T. Campbell, Trends in Adhesion Energies of Metal Nanoparticles on Oxide Surfaces: Understanding Support Effects in Catalysis and Nanotechnology, ACS Nano, 11 (2017) 1196-1203.